Coherent Control of Atoms and Molecules

by

Randy Alan Bartels

A dissertation submitted in partial fulfillment
of the requirements for the degree of
Doctor of Philosophy
(Electrical Engineering)
in The University of Michigan
2002

Doctoral Committee:

Professor Henry C. Kapteyn, Co-Chair
Professor Margaret M. Murnane, Co-Chair
Professor Philip H. Bucksbaum
Professor Emmett Leith

For Malini

ACKNOWLEDGEMENTS

During my graduate career, many people have generously provided support and guidance from many people to whom I am exceedingly grateful. First and foremost, I would first like to thank my wife Malini for all of her kind support, encouragement, and unconditional love. She is my best friend and her love and support mean the world to me. My family and friends scattered around the globe have been a continual source of support and encouragement.

I can't imagine a graduate school experience that would be better for me than the one I experienced. For that, my advisors Margaret Murnane and Henry Kapteyn must take a large share of the credit. They have been friends and mentors to me, allowing me to explore just about anything that interested me. In fact, we even did a few of Henry's famous "one-day" experiments in more-or-less a day. At the same time gently nudging me in the direction they, in their wisdom, deemed best for my career. As a result, I have learned far more about a broad range of fields than I could have imagined would have happened during my Ph.D. work. I count Margaret and Henry among the most generous, genuine, and supportive people I know. On top of that, they are truly world-class scientists and it has been an honor and a privilege to work with them during the last 4 years.

Shortly after I began working for Margaret and Henry, they moved from the University of Michigan to the research laboratory JILA located on the campus of the University of Colorado in Boulder. This was a wonderful experience, allowing me to study at two excellent institutions. I was the first person in the group to make the trek out to Colorado, and I began building a laser system as the parts arrived in boxes. This gave me a wonderful opportunity to learn the laser system intimately and made running it on a daily basis much easier. JILA is a wonderful place to do experimental work because of the wide array of talented, knowledgeable, and helpful support staff.

I am grateful for the help of many other incredibly talented scientists, postdocs, and students during my graduate studies. Sterling Backus has been a tremendous resource. He quite possibly knows how to build and run ultrafast laser systems better than anyone else in the world. I have had the good fortune of using an updated version of the amplifier system that he designed in his Ph.D. work and has continually improved and advanced over the years. Sterling and I worked together on a majority of the experiments that make up this thesis work. Working with him has both been fun and fruitful. He was there with me many times working into the wee hours of the morning, sustained only by Cheetos and iced tea. I am also indebted to Erik Zeek who developed the deformable mirror pulse shape that I used

extensively in my work and for him letting me bug him repeatedly with questions about programming in Labview. Chip Durfee showed me how to make HHG radiation with a hollow core fiber, and taught me many things about doing good scientific experiments. Lino Misougti was a great resource in the lab and was always willing to drop what he was doing to help anyone with their experiments. Lino is also responsible for taking the bulky hollow-core fiber setup and transforming it into a stable, efficient setup. Ivan Christov worked with us to develop a very successful model of the HHG control experiment, and with his help, we were able to demonstrate that we were controlling the process with attosecond precision. Hersch Rabitz was very excited when he heard about our experimental results in the control of HHG. We spoke with him quite extensively and worked in collaboration on modifications to the learning control algorithms that allow the algorithm to learn about the system under control and find more robust solutions. Tom Weinacht and I developed a series of experiments to control molecular systems. Because we developed an approach that operated at room temperature, we were able to try many experiments very quickly, and had lots of fun. When we delved into the field of Chemical Physics, the immense technical knowledge in that field at JILA was extremely helpful. In particular, we have had many useful discussions with Steve Leone, David Nesbitt, and David Jonas. In the experiment where we compressed ultrafast optical pulses with spinning molecules, Mark Baertschy (a postdoc of Chris Green's, who is a fellow here at JILA) modeled the experiment, and helped us understand how we can optimize the compression experiment. Nick Wagner came to work in our lab the summer before he started graduate school and was involved in the demonstration of this new pulse compression technique. We are now working with Nick, Mark, Chris, and Marcos Dantus in an effort to optimize this pulse compression method. Dave Attwood at UC Berkeley and LBNL is an expert in the coherence of EUV and soft x-ray radiation. When we began our work on studying the coherence properties of hollow core phase-matched radiation, we worked closely with Dave and his student Yanwei Lui on the experiments. We have also worked with Chris Jacobsen from the Department of Physics & Astronomy, SUNY at Stony Brook and Brookhaven National Laboratory who has been a tremendous source of information on coherent x-ray imaging and has worked with us to do phase-retrieval imaging with our EUV source. All of the other students and postdocs in the laboratory (including Robbie, Tim, Dave, Scott, Rannan, Erez, Emily, Tennio, and any I may have omitted because of my limited memory) have made my experience very enjoyable. I wish them all luck and thank them for making my journey exciting, pleasant, and fun.

TABLE OF CONTENTS

LIST OF TABLES

Table

LIST OF FIGURES

Figure

LIST OF APPENDICES

Appendix

CHAPTER I

Introduction

From a practical point of view, atoms are the basic building blocks that we can use to manipulate our natural world. Molecules are collections of atoms with behavior drastically different from that of the atoms of which they are composed. The ability to control these atoms and molecules has driven the creation of materials that has revolutionized every aspect of technology that impacts our daily lives. Furthermore, the synthesis of chemicals (including life-saving drugs) also relies on our ability to control atoms and molecules. Current methods used to control the atoms and molecules that drive much of our technology are based on thermodynamics. An understanding of those laws allows us to exploit the predicted behavior of atoms and molecules for the synthesis of materials. Improvements in our ability to control atoms and molecules beyond what is allowed by thermodynamics will usher in a new era of technologies based on the control and not just the observation of nature.

At the turn of the previous century, it became apparent that a thermodynamic and deterministic mechanics description of matter, especially for the case of small objects like atoms and molecules, could not explain all of the observed behaviors.

This led to the development of quantum mechanics, which uses wave mechanics of matter to explain much of the observed behavior. Because the behavior of atoms and molecules can be describes as waves, they exhibit interference effects between these matter waves. However, in order to observe the wave interferences of an ensemble of quantum-mechanical objects, the waves must be stable with respect to one another, i.e., the ensemble must be coherent. The coherence of a system is not preserved in the presence of collisions or spontaneous radiation, and all quantum-mechanical systems are subject to these de-coherence mechanisms. The time-scales for de-coherence of atoms and molecules at room temperature are on the order of pico and femto-seconds.

Provided there is a coherence, the wave interferences of atomic and molecular quantum-mechanical wavefunctions can be manipulated by the application of an external electro-magnetic field. By manipulating this external control field, the wave interferences can be tailored to produce a desired final quantum-mechanical state that may result in the production of a specific chemical reaction product, or the shaping of the power spectrum of radiation produced by the atom or molecule. Efficient control requires that the control field interact with a coherent ensemble. In order to create and manipulate a quantum-mechanical population efficiently, the time-duration of the control field must be sorter than the de-coherence time. Furthermore, the natural time-scale of evolution of atoms and molecules is femto to picoseconds. As a result, in order to efficiently control the wave interferences of atoms and molecules, the use of coherent, ultrashort pulses of light is required. Atoms in molecules with negligible thermal population vibrate with characteristic periods of

$<$ 50 femtoseconds, while electronic wave functions in molecules in our experiments have sub-femtosecond lifetimes. In order to access these natural timescales, an optical source with a broad-bandwidth, corresponding to controlled sub-20 femtosecond pulse durations is required.

This thesis work sought to control the dynamics of quantum-mechanical systems using shapes light pulses [1, 2].

The new scientific advances discussed in this thesis are:

- The application of coherent control techniques to a highly nonlinear quantum system.
- Attosecond control of a process for the first time by controlling the phase of an electron wave packet with a shaped light pulse.
- Demonstration that a learning algorithm can be used as a powerful tool to discover new science.
- Discovery of a new phase matching mechanism in the high-field regime that occurs between a single atom and a light field.
- The first demonstration that a non transform-limited pulse can optimize a purely electronic nonlinear process.
- The generation of nearly transform-limited soft x-ray pulses.
- Demonstration of learning control of molecular vibrational coherences at room temperature and atmospheric pressure.

- Observation of molecular wave packet dynamics by analyzing the phase modulation imposed by a time-varying molecular polarizability.
- Self-seeding of impulsive stimulated Raman scattering.
- Use of modified cost functionals in a learning algorithm to learn about a system under study.
- Generation of a perfectly spatially coherent XUV beam for the first time.
- The first demonstration of the measurement of the spectrum of a light field by analyzing a double-pinhole interferogram.
- The demonstration of a new pulse compression scheme using phase modulation from controlled molecular rotations.

We achieve control of quantum systems by interacting a very broad bandwidth, shaped light pulse with atoms and molecules. To determine how to shape the optimal light field, I used an idea proposed by Herschel Rabitz in 1992 [3] that suggestes using a feed-back loop (or more appropriately, a learning loop) to allow the quantum system under investigation to determine which pulse shape best controls the system.

The idea of using learning control was a revolutionary advance for the field of "coherent control" because of the difficulty in determining optimally shaped fields to control complex, real-world, quantum systems; however, it is an approach that is borrowed from engineering. A number of scientists have implemented this idea in the laboratory, but the experiments focused on systems easily understood [4, 5, 6, 7, 8], where the optimal field was easily calculated, or extremely complex systems that

could not be understood theoretically [9, 10]. Furthermore, none of these prior experiments demonstrated that optical control of a quantum system could have practical applications outside of understanding and controlling quantum dynamics, leading critics of the field to complain that coherent control is an impractical way to control systems. Moreover, many thought that there is no hope of understanding the control mechanism for complex systems and that, once controlled, the systems were of no practical value to scientists in other fields. Herschel Rabitz's idea of learning control was also criticized as a naïve approach to science and that experiments are best performed under the direct control of the scientist.

In this thesis, I describe a set of experiments that address these major criticisms of coherent control, and shows that learning control algorithms can, in fact, act as powerful tools for discovering new, useful science. The work described in this thesis represents scientific advances physics, chemical physics, chemistry, and optical engineering. We have applied these learning, coherent control techniques to the control of electron wave packets in atoms, and to the control of rotational and vibrational wave functions in molecules.

The format of this thesis is as follows: the second chapter gives a brief description of learning control and evolutionary algorithms, the third chapter discusses control in atoms, the fourth chapter discusses the control of molecular systems, the fifth chapter discusses useful applications of controlled quantum systems, and the sixth chapter summarizes this work.

In the third chapter, I explain how to achieve the control of high harmonic genera-

tion (HHG) [11, 12, 13] using broad-bandwidth, shaped light pulses. HHG normally produces a frequency comb of harmonic lines that are an odd integer multiple of the driving laser frequency. I demonstrate that a learning algorithm can be used to find an optimal HHG spectrum to produce a single harmonic, resulting in a quasi-monochromatic x-ray spectrum that is concentrated in a femtosecond duration pulse. In this experiment, the learning algorithm found a new solution that was previously unknown, and would have likely gone undiscovered. This spectrum has applications to a wide variety of time-resolved x-ray experiments because it generates a very short duration x-ray pulse without the need for spectral filtering that might broaden the pulse. Not only does the optimal pulse shape modify the HHG spectrum, it also increases the conversion efficiency of energy from the fundamental driving laser pulse to the x-ray pulse, compared to the conversion efficiency of a transform-limited pulse into HHG light. This result was very surprising, and is the first demonstration of the optimization of a nonlinear process by a non transform-limited laser pulse. Finally, since HHG is the most "extreme" nonlinear process that has ever been observed. This thesis describes the coherent control of a quantum system with the highest nonlinearity to date.

Chapter 3 also discusses models of HHG generation [14, 15, 16, 17, 18] that can describe most of the experimentally observed features. A theoretical model was used in conjunction with a learning algorithm, and the result was that the model exhibits excellent agreement between theory and experiment. Through our understanding of the control of HHG [13], we discovered a new phase-matching mechanism that occurs

between the interaction of a single atom and a pulse of light. This phase matching mechanism is the result of the control of the phase of an electron wave packet with 25 attosecond precision. Thus, this work is the first experimental demonstration of the control of any process with attosecond precision. These results directly refute assertions that the control mechanism of a complex quantum mechanical system can not be determined from a learning control experiment. In fact, in our experiment, the learning algorithm discovered new science.

In the fourth chapter, I apply the learning control "machine," developed originally for the HHG experiments, to the problem of controlling molecular systems. The ultimate goal of such control is to manipulate chemical reactions [19], resulting in the synthesis of products that would be otherwise difficult, or impossible, to synthesize by other methods. The essential idea is to use an optimal control pulse to distort molecules in such a way that a barrier to a reaction pathway is reduced or eliminated, allowing a reaction to proceed. A surface catalyst acts in much the same way in that the surface itself distorts the reactants in order to initiate a chemical reaction. Thus, the shaped laser pulse in this scheme acts as a laser catalyst.

Using the learning machine, we performed experiments that manipulated vibrational and rotational degrees of freedom in molecular gasses and vapors [20, 21]. Due to the short duration of our laser pulses, we are able to induce coherent motion in molecules that exhibit substantial "random" motion, i.e., in gasses at room temperatures, and where the gas is held at atmospheric pressure. This approach holds the promise of coherently "driving" chemical reactions in "real-world" condi-

tions, resulting in macroscopic quantities of products. Furthermore, our approach is non-resonant and can be applied to any molecular system.

In these experiments, we demonstrated selective control (or heating) of specific vibrational modes in multimode molecules. We have also developed a new form of molecular spectroscopy that monitors molecular wave packet motion by analyzing the modified power spectrum of a probe pulse. The probe spectrum experiences changes when phase modulated by the time-dependent molecular polarizability generated by the pump pulse. This approach allows us to monitor the evolution of ro-vibrational wave packets and observe and control overtone and combination band vibrational excitation. The observation of overtone excitation using this technique [21] is an important development towards mode-selective chemistry. Finally, we observe indications of control of the reaction rate of a bimolecular chemical reaction with shaped laser pulses.

Learning control has been shown to be a powerful tool for the control of complex quantum systems. This approach allows one to control the system, even if the details of the system are unknown. During the course of an optimization, many "experiments" are performed, each with a different pulse shape. These distinct pulse shapes each probe the quantum system in a different way. By collecting and analyzing these experimental results, it may be possible to uncover information about the system under control.

We have taken a first step towards using the learning algorithm itself to determine information about the system under control. The learning algorithm was modified

so that the pulse shaper was "penalized" (i.e., reducing the fitness value) for pulse shapes that deviated from a target shape. The effect is that control knobs that do not result in an improvement of the system control are not used. The result is that the optimal pulse shapes are simplified, and only the essential control features are preserved. These experiments are the first demonstration of the use of modified cost functionals to learn about the system under control. The simplified optimal pulse shapes clearly demonstrate the control mechanism and illustrate the promise of using the algorithms to learn about the systems under investigation.

In the first section of chapter 5, I discuss the generation of controlled molecular rotational wave packets, and demonstrate a new technique for compressing ultrafast optical pulses [22]. This technique is applicable at any wavelength from the deep ultraviolet (deep-UV) to the infra-red (IR) regions of the spectrum. In our scheme, one light pulse was used to create a set of "designer" spinning CO_2 molecules inside a hollow glass fiber. The "designer" nature of the spinning CO_2 molecules is that they align and realign periodically, having been set spinning (or "kicked") at the same time by the light pulse. This light pulse is 20 femtoseconds in duration at a wavelength of 800nm, in the near-IR (where it is easy to generate such fast pulses of light). A second, longer duration light pulse with a different wavelength (color) is then sent into the same fiber, at precisely the right time where it encounters the spinning molecules. The aligning molecules act like microscopic molecular modulators - tiny versions of the modulators used to encode optical pulses for transmitting voice and data information across optical networks. This coherently-evolving molec-

ular system exhibits faster modulation times (ps) than is possible using electro-optic modulators, corresponding to the time of less than one picosecond during which the molecules come into and then go out of alignment. This system thus has an enormous bandwidth exceeding 40 THz. Such ultrafast modulation causes dramatic spectral modulation of the second pulse, increasing its bandwidth by over an order of magnitude. This increased spectrum means that the time duration of the second pulse can also be compressed by an order of magnitude, provided that all the new colors in the light pulse can be made to arrive at the same time. One very attractive feature of this scheme is that this second pulse can be compressed by simply sending it through a piece of glass. This is much simpler to implement than traditional approaches to compressing light pulses that require sending the spectrally-broadened pulse through a prism or grating pair. It is also far less lossy (particularly in the UV), and far more compact. Thus far we have demonstrated that this scheme can easily generate 30 femtosecond duration light pulses. The next step will be to generate < 5 femtosecond light pulses in the deep-UV and vacuum-ultraviolet, where materials and many small molecules can be probed.

In the second section of chapter 5, we show that, by using a phase-matched hollow-fiber geometry, the EUV light generated exhibits the highest inherent spatial coherence of any source in this region of the spectrum [23]. Since this source exhibits full spatial coherence at very short wavelength, this light source represents the smallest inherent effective source-size of any light source yet created. While studying the spatial coherence of HHG, I realized that by measuring the spatial coherence, the

power spectrum of the incident field could be determined [24]. We demonstrate this by comparing the deconvolved spectrum with that obtained by a traditional grating spectrometer. HHG generated in a hollow-fiber geometry is constructed on a fraction of an optical table. Finally, in the third section of Chapter 5, I show the application of this versatile source to coherent x-ray imaging that may be useful for plasma and biological imaging.

CHAPTER II

Coherent control of quantum systems with learning algorithms

2.1 Introduction

Since the advent of the laser in the early 60's, researchers have sought to use laser light to solve problems in virtually every scientific discipline. Chemists, in particular, looked upon this intense single-frequency light source as a way to manipulate chemical reactions. The initial idea was simple: simply tune a laser source to the characteristic frequency of a bond you wish to break and turn up the intensity of the laser. The molecule should snap apart and you could use those products to drive and control chemical reactions. However, in the laboratory this idea was a complete failure. Energy that was dumped into specific bonds redistributed itself throughout the molecule on femtosecond to picosecond timescales [25]. Increasing the energy only broke the weakest bond in the molecule and no control seemed possible.

Thus, the dream of manipulating matter with light pulses soured and research interest dwindled. This early work ignored a significant aspect of the molecules they sought to control. Molecules are quantum mechanical systems and their normal

modes are described by waves that can interfere [1, 2]. Shaped light fields can control this interference and thereby control the final state of the system (as illustrated in Figure 2.1); this approach has been dubbed "coherent control". Coherent Control techniques have evolved from focusing solely on chemical systems to a wide range of quantum mechanical systems, and have been applied to semiconductor systems [26, 27, 28, 29, 30, 31], terahertz radiation sources [32, 33, 34] , shaping of Rydberg wave functions [6], and single atoms [11].

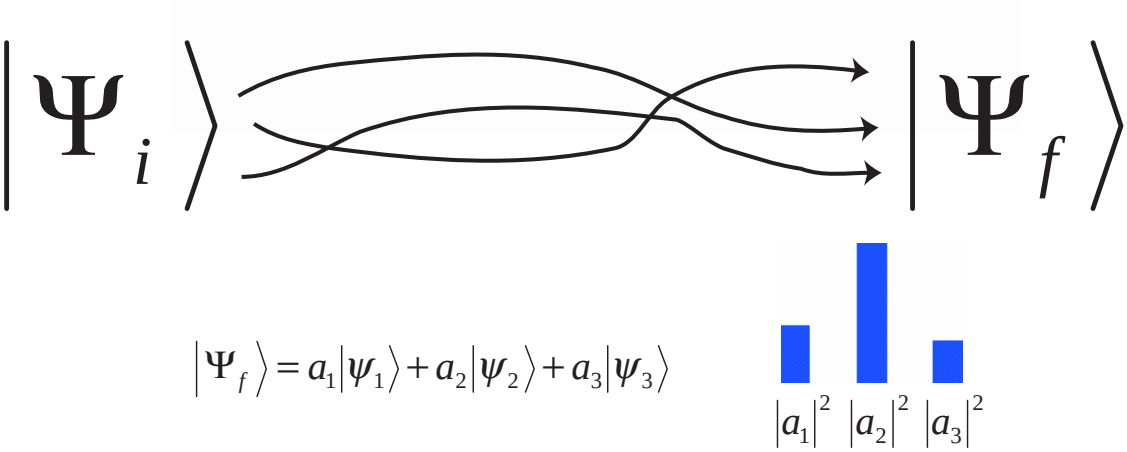

Figure 2.1: Coherent control is accomplished by manipulating inferring pathways in a quantum mechanical system.

2.1.1 A brief history of coherent control

Two major approaches to the control of quantum mechanical systems have been proposed and developed. Both of these ideas exploit wave interferences in quantum mechanical systems and highlight different aspects of this mechanism. The first proposal by Brumer and Shapiro [35] excites two pathways that interfere constructively or destructively depending on the relative phase of two CW lasers. The probability of forming a given product or exciting a particular state depends on the coherent

sum of the two states since they are indistinguishable.

This technique has been utilized by Elliot to control transitions in mercury [36] and thoroughly studied in Robert Gordon's group to control the ionization of HCl, CO, and H_2S [37], photoexciation of HI [38], and controlling product ratios of the photodissociation of H_2S [39] and CH_3I [40]. Shnitma et al. demonstrated the control of branching ratios in the photodissociation of Na_2 [41], while Dupont et al. demonstrated the control of photoexcited electrons in semiconductors for applications in fast switching [27].

Although this approach has been quite successful, its efficiency is limited because quasi-CW lasers act on only a fraction of the thermal distribution of atoms or molecules in which control is sought. For example, at 1 K, the thermal energy kT is ~ 20 GHz, which is larger than a ns pulse bandwidth. Energy redistribution relys on relatively slow processes such as collisions to restore depleted populations. Furthermore, the decay of coherences limits the amount of energy that can be effectively used for control because these coherences are required for stable wave interference.

An alternative approach proposed by Tannor and Rice suggested using pairs of short pulses to manipulate quantum mechanical wave packets [42, 43]. More generally, this can be viewed as optimal control in which some optimally shaped electromagnetic field is used to sculpt a desired final quantum mechanical state [44]. This concept is illustrated in Figure 2.2. The pulses used in this approach are shorter than the energy redistribution and coherence decay times in molecules, making it highly efficient. A short pulses excites vibrational wave packets that evolve in a

field-free manner, and that achieve a desired target goal at some specified time.

There are generally three types of control that are grouped in this control scheme. The first utilizes pulse pairs that excite two time-delayed quantum mechanical wave packets that interfere to excite specific states in the system. The second, called pump-dump, excites a wave packet on an excited state surface, then a second pulse "dumps" that population to a ground-state level, or some dissociative product channel. The final, more general, approach is to determine a single, shaped optical field that creates an optimal quantum mechanical state.

Figure 2.2: Optimal control is a variation of coherent control that uses a shaped optical field that drives a quantum system form some initial state into a desired final state.

Coherent control with pairs of unshaped phase-locked pulse pairs has been demonstrated in a host of molecular [45, 46, 47, 48, 49, 50, 51, 52, 53] and semiconductor [28, 29, 30, 34, 31] systems. Optimally shaped laser fields offer the most versatile and general approach to the control of quantum mechanical systems. The optimal field guides the system from some initial state to the desired final state by working in conjunction with the system evolution. The capabilities of this approach can be extended in the high-field regime as the optimal field itself begins to substantially modify the potential of the system under control and allows for more complex control [10].

The calculation and shaping of optimal fields for control has been demonstrated for selective control of optical phonons in cryogenic solids [4], the control of excited state vibrational wave packets [54, 55], controlling the yield of a chemical reaction [56], the control of 2-photon absorption [5, 57, 58], and for the control of molecular vibrations with overtone excitation [21].

Determining the optimal driving field for controlling quantum systems requires detailed knowledge of the Hamiltonian of the system to be manipulated, ample computer time to calculate the field (where all experimental conditions must be known exactly). The primary difficulty here is that the Hamiltonian for most systems is unknown, particularly for complex chemical systems. Furthermore, it might be difficult and time-consuming to calculate the optimal field given the Hamiltonian. Once found, there is no guarantee that the optimal field will be robust and the control may be very poor on average as the experimental conditions fluctuate. Finally, even if we have the exact optimal field, it can be difficult to reliably deliver the optimal field to the quantum system to be controlled.

2.2 Learning algorithms for coherent control of quantum systems

The difficulty of calculating the optimal field for controlling a quantum system gets progressively more difficult as the system gets more complex. However, a clever approach proposed by Rabitz et al. [3, 59, 2], demonstrated through computational simulations that trial-and-error learning algorithms can in principle be applied to optimally control quantum systems. This approach essentially uses the quantum

system under control as an analog computer, testing each trial solution, and guiding the laser system to discover the optimal field. This approach solves the basic problems of optimal control discussed above. The quantum system knows its own Hamiltonian, and no computation time is required because the system solves for the solution essentially instantly. The solution found is guaranteed to be robust because the control is achieved in a noisy laboratory environment where the experimental parameters may be fluctuating. Finally, since the control filed is found *in-situ*, the correct optimal filed is automatically delivered to the quantum system under control.

Figure 2.3 illustrates the basic concept of a learning loop. The learning algorithm tests large groups of trial pulse shapes on the quantum system and evaluates how well the pulse shape allows the system to evolve to the desired outcome. The learning algorithm then uses the results of the experiments to determine new pulse shapes to try, and repeats the loop until the system is in the target quantum state. As the learning algorithm iterates through each loop, it learns to control the quantum system better until eventually the algorithm "teaches" the laser how to control the quantum system.

2.3 An overview of learning algorithms

The type of learning algorithm employed to control quantum systems is typically an evolutionary algorithm. These algorithms are so named because the inspiration for their design is based loosely on the principles of biological evolution. The basic steps of reproduction, natural selection, and diversity by variation are all used in a typical evolutionary algorithm. The reproduction stage mixes genetic information

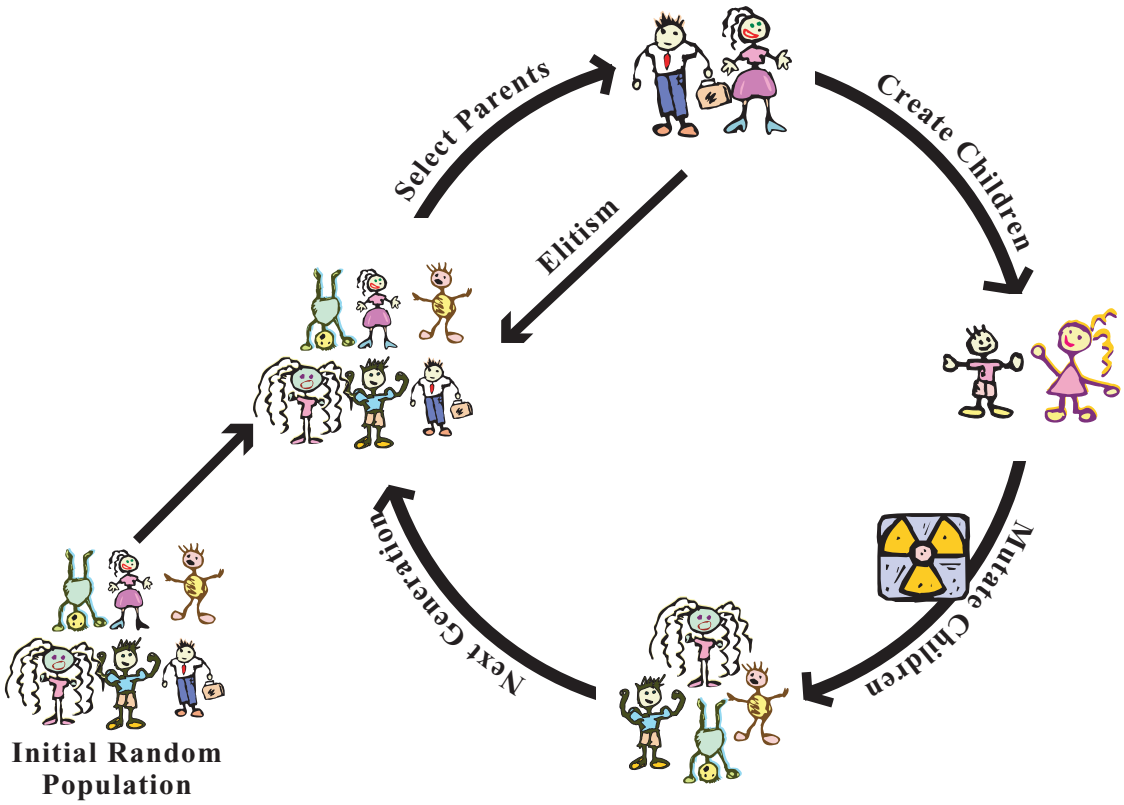

Figure 2.3: An evolutionary algorithm can be used to teach a laser system to control a quantum system. The algorithm begins with a random population. Each member of the population is a trial pulse shape; for our system, a trial pulse shape is represented by the set of voltage levels applied that distort a deformable mirror. Each trial pulse shape is tested in the system under control, and then a fitness value is calculated that quantifies the quality of the control. A fraction of the fittest members of the population are duplicated, forming the set of children. Those children are mutated so that the solutions are perturbed. The parents and mutated children are combined and the process repeats. After a number of iterations, the algorithm converges to an optimal control field (the best trial pulse shape).

from two members of a population to produce a "child" (new trial solution) with a combination of traits from the two parents. Natural selection is the process that chooses individuals that propagate to the population that forms the next generation. In nature, this is a combination of the fitness (or degree to which an individual has successfully adapted to his environment) and chance that determines what genetic information is passed to the next generation. Finally, there is diversity in genetic information due to the variation in members of a population. Mutation of genetic information is the primary way that new genetic information is introduced into a population.

2.3.1 Terminology of Evolutionary Algorithms

Before delving into a discussion of evolutionary algorithms (EA), it is important to define the components of the algorithms. The DNA gives the genetic information of a member of the population, which can carry either phenotypic (characteristics of the individual) or genetic (a coded form of the phenotype) information. The type of information contained in the DNA varies according to the type of EA used. A population is a set of members, which are described by their DNA. The fitness of an individual is a measure of how well the individual has adapted to the environment. For the purposes of controlling a quantum system, the fitness is determined by evaluation some observable of the quantum system. This fitness function can be viewed as a mountainous landscape (i.e., fitness landscape) and a "good" solution corresponds to a tall mountain peak. There is may be a global optimum, which is simply the tallest peak in the landscape. The process of selection determines which

members of the population are carried over to the next generation. It follows that selection also determines what information from the pervious experiments is retained by future generations. Recombination and mutation operations serve to perturb the DNA content of members of the population in order to explore the parameter space of the fitness landscape and avoid a local minima.

2.3.2 An overview of evolutionary computation

The foundation for current evolutionary algorithms come from work done just as computers began to emerge as a tool in large research facilities. However, the low computational speed and memory of these machines hampered this early work. The idea of automatic programming was first presented in the work of Friedberg [60] at IBM. The idea was to use a limited set of instructions from which a computer algorithm could select to construct a program that would convert an input to a desired output. This approach used no selection mechanism and turned out to do worse than a pure random search. The next attempt was by Bremermann [61] to perform evolutionary optimization. He sought to optimize functions by recombination and mutation. However, his algorithm did not converge well and was largely ignored. Both automatic programming and evolutionary optimization, although flawed, provided the basis for future developments in evolutionary algorithms.

Using the lessons of Friedberg and Bremarmann, Fogel tried another approach he called "evolutionary programming" (EP) [62]. This new approach used selective pressure to push a population towards a solution. The original implementation compared a parent and a child (a mutated version of the parent) and kept the better

one for the next generation. He later expanded the number of members to form real populations and introduced recombination operators. An EP represents the DNA (or set of information that describes the trial solution as implemented in a learning system) as simply the control knobs (i.e., parameters of the system that we control) that manipulate the device that produces the trial solution we wish to analyze in our apparatus. The DNA elements are mutated with a normally distributed random variable weighted by a scaled fitness value. Recombination is not used in EP because it is seen as secondary to mutation [62]. The members of the population that form the next generation are taken from the union of the set of parents and children from a tournament (tournament selection operator). This work was ignored until the early 70's when genetic algorithms and evolutionary strategies were developed independently in the US and Germany.

Evolutionary Strategies (ES) were developed by Bienert, Rechenberg, and Schwefel at the Technical University of Berlin for the optimization of fluid dynamics problems (e.g., optimization of nozzle shapes) [63]. The initial implementation compared a parent (μ) and a child (λ) in a manner similar to EP. Later versions made use of large populations including both parents and children ($\mu + \lambda$), referred to as *elitism*, or only the children made by the parents (μ, λ). Schwefel also introduced the self-adaptation of algorithm operators so that the operators can be optimally adjusted throughout the optimization [64].

The DNA (or set of variables that produces a trial solution) in an ES simply uses the control knobs directly just as in the EP. The mutation operator adds a

normally distributed random variable, with some variance, to each component of the DNA. The variance is also modified on each iteration so that the mutation rate self-adapts. A recombination operator then splits the DNA into pieces and exchanges information. This recombination operator has been viewed by some as a macro-mutation operator. The members of the population of the next generation are then simply the set of children, or the combined set of children and parents in the case where elitism is included. The optimal convergence rate has been found to correspond to a ratio of children to parents equal to seven ($\frac{\mu}{\lambda} = 7$) [63]. There is no theoretical optimum for the number of parents; however, setting μ too small results in a path oriented search, whereas a larger μ takes advantage of a population, but consumes more computation and experimental time.

John Holland, working independently at the University of Michigan, developed the genetic algorithm (GA) in parallel with the ES development in Germany [63]. The DNA in a GA is not simply the control knobs, but a transformed version of the control knobs (or variables we apply to our "solution generator apparatus"). Instead, each variable in the DNA is transformed into a new representation. The most commonly used representation for DNA in a GA is to convert the control knobs to their binary numeric representation. For example, if the "control knobs" that would be used in an evolutionary program or an evolutionary strategy were the set $\{2, 4, 9, 3, 4\}$, then in a 4-bit binary encoding, the DNA would be $\{00100100100100110100\}$. Due to the binary nature of the representation, a Gaussian mutation operator is no longer appropriate, and as a result, the mutation operator used in a GA is random bit flips.

The mutation operator is seen by Holland as secondary, so the mutation probability is set to be small in a typical GA implementation.

Recombination on the other hand, is quite evolved in a GA. The initial operator was simply a one-point crossover, similar to ES, where the genetic information is exchanged between two parents at a single point. The obvious extension of this is to exchange several blocks of DNA (multipoint crossover) by splicing the DNA at several locations. More advanced versions of these recombination operators have been made to self-adapt. The simplest, segmented crossover, is multipoint crossover with an adaptable number of crossover points [65]; they also used shuffle crossover which mixes up the ordering of the DNA blocks. The most advanced recombination operator, punctuated crossover, dynamically varies the number and locations of crossover points [66]. Instead of choosing the member for the next generation to be only the top performers, the members are selected by a roulette wheel selection. The idea is that each member of a population (trial solution) is assigned a probability that is proportional to its fitness value. A fraction of the current population is chosen to proceed to the next generation by a random number generator that favors more "fit" solutions that have larger fitness values.

2.4 Experimental demonstrations of Learning Control

A number of experiments have recently demonstrated the use of shaped pulses for control of quantum systems with a learning algorithm. Bardeen et al. [67] demonstrated that a learning algorithm can determine that a pulse with positive chirp is optimally effective in avoiding saturation of a molecular transition and the control

in I_2 in both the gas and solid phases. Gerber et al. [9] demonstrated that molecular dissociation could be controlled through the use of pulses with a complex shape determined through a learning algorithm. Bucksbaum et al. [6] demonstrated the use of iterative algorithms to "sculpt" Rydberg atom wavefunctions into the desired configuration, and also to control Stokes scattering in molecular systems. Weinacht et al. demonstrated the control of Raman scattering in liquids [68]. Leone et al. [8] demonstrated the time-shifting of rotational wave packet dynamics in Li_2. These experiments represent systems at the two extremes of complexity. In the case of one-and two-photon absorption or molecular excitation, the physical reasons behind the optimum solutions are straightforward to understand. In the case of vibrational excitation or dissociation of polyatomic molecules, the pulse shapes obtained through optimization are complex and extremely difficult to interpret.

In contrast, as will be discussed in Chapter 3, the case of high-harmonic generation represents a quantum process that is highly nonlinear, but that nevertheless has proven to be both accessible to experiment and theoretically tractable. The optimal laser pulse for coherent x-ray generation can be explained as a new type of "intra-atomic" phase matching [13], that enhances the constructive interference of the x-ray emission from different electron trajectories driven by adjacent optical cycles for a particular wavelength (i.e. harmonic order). This intra-atomic phase matching allows us to selectively increase the brightness of a single harmonic order by over an order of magnitude, essentially channeling the nonlinear response of the atom to a particular order of nonlinearity. Furthermore, the arbitrary control over

the shape of the driving pulse allows us to spectrally narrow a given harmonic order very effectively, resulting in a bandwidth of the harmonic peak that is likely to be at or near the time-bandwidth limit for such a short x-ray pulse. Finally, optimization of a single harmonic without suppressing adjacent harmonics can increase the brightness of some harmonic orders by factors of ≈30.

Furthermore, it was thought that the learning algorithm was not sufficiently robust to operate on high-order or highly complex quantum systems. Our work demonstrating control of high harmonic generation showed that a high order quantum system could be controlled, and that control could also be well understood.

2.5 Experimental Apparatus

For our work, we used a broad-bandwidth, short-pulse-optimized Ti:sapphire amplifier system into which a closed-loop pulse shaping apparatus was incorporated [69]. By careful design of these amplifier systems, pulses as short as 15 fs (approximately 6 optical cycles) FWHM can be generated at high repetition-rates and high pulse energies (up to 7 kHz with pulse energies > 1 mJ). In such laser systems, low energy pulses of duration ~ 10 fs are generated by a broad-bandwidth Ti:sapphire oscillator [70], stretched in time to lower their peak intensity, and then amplified in two amplifier crystals prior to re-compression. This type of laser system is ideal for inclusion of a simple, phase-only, pulse shaper into the beam before amplification, since phase modulations introduced by the shaper will propagate without distortion in the high-energy, amplified, laser pulse.

We used a new type of phase-only pulse shaper for this work, incorporating a

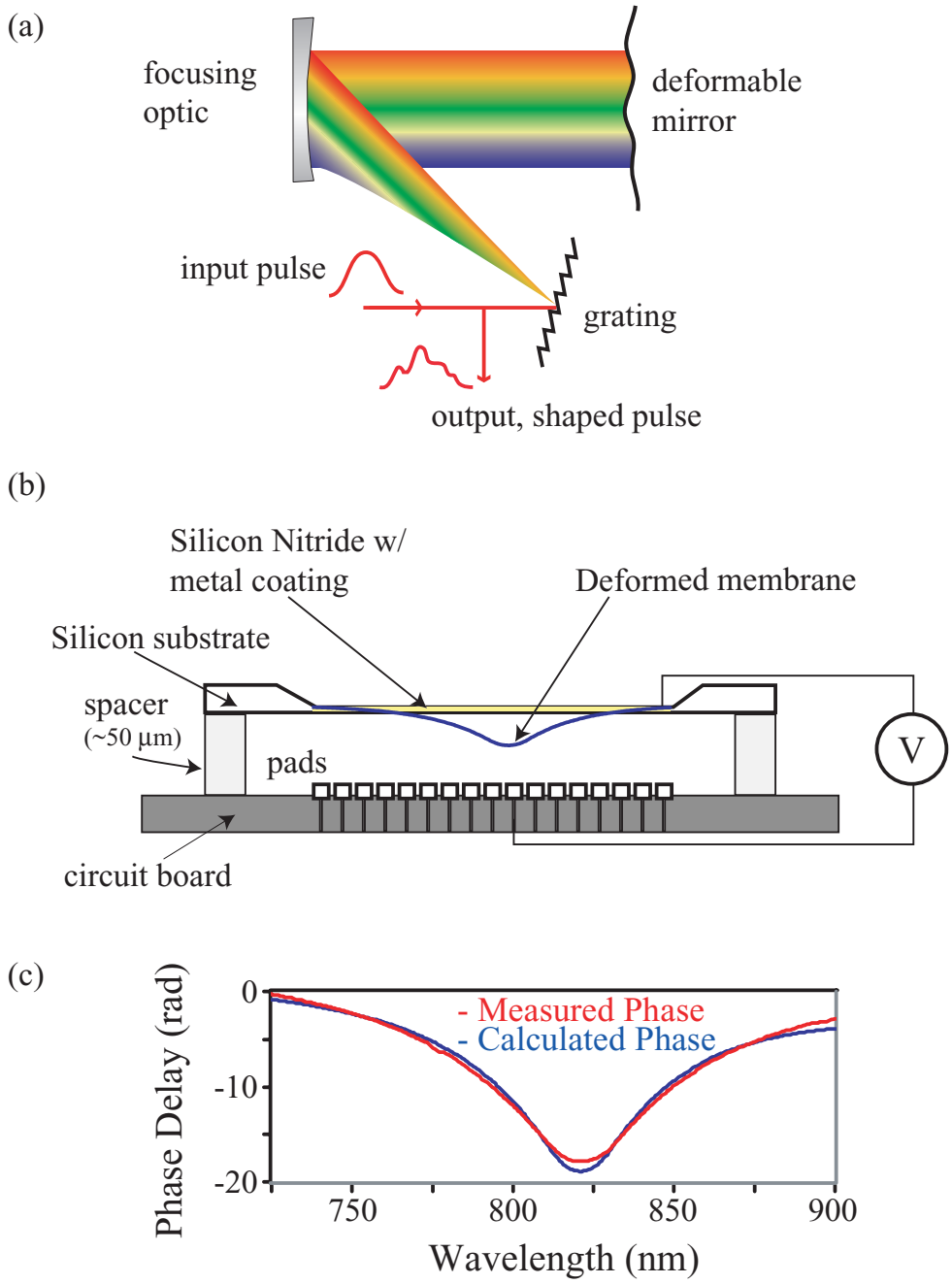

Figure 2.4: A deformable mirror that folds a zero-dispersion stretcher (a) can be used to adjust the relative delay of colors (and thereby spectral phase) of an optical pulse. The mirror (b) is constructed by growing a layer of Si_3Ni_4 (600 nm) on a Si substrate and back-etching a window which is over-coated with a metal. This mirror is suspended over an array of pads patterned on a PC board. When a voltage is applied to one of the pads, the mirror deforms due to electrostatic attraction, changing the spectral phase (c) [71].

micro-machined deformable mirror [69, 71]. This simple shaper (illustrated in Figure 2.4) works by separating the color components of the ultrashort light pulse (which span $\sim 80\,\mathrm{nm}$ bandwidth centered at $800\,\mathrm{nm}$) using a grating, then reflecting them from the deformable mirror. Subsequently, the color components are reassembled to form a collimated, temporally shaped, beam. Altering the exact shape of the mirror can then control the relative arrival time of each color component in the pulse. Thus, the pulse shaper manipulates the phase of the pulse in the spectral domain, reshaping the pulse shape and phase in the time domain, while conserving the pulse energy. The mirror itself is a smooth silicon-nitride surface incorporating 19 actuators that deform the mirror — thus it is possible to precisely control the pulse shape, without introducing artifacts due to discrete pixellation. Furthermore, by not altering the spectrum of the pulse, we avoid possible pulse distortions due to nonlinear self-phase modulation in the amplifier. The deformable mirror used in this work was capable of deflecting up to 4 μm (or 20π at 800 nm), which compensates for the dispersion accumulated by propagation through 1 cm of fused silica [71]. The exact shape of the pulse, including the amplitude and phase of the electromagnetic field, can be measured using the second-harmonic generation frequency resolved optical gating (SHG FROG) technique [72].

The laser system was adjusted to produce a transform-limited laser pulse that demonstrates the utility of our evolutionary algorithm, and provides a benchmark pulse shape for comparison with our coherent control experiments descried in chapters 3 and 4. We used an evolutionary algorithm that starts with a population of

$\sim$100 members, each of which corresponds to a particular set of voltages applied to the 19 mirror actuators (the DNA). The fitness of the corresponding pulse shape is then measured experimentally. The fitness is simply a quantitative measure of the desirability of a population member, and for pulse compression, we use the intensity of the frequency doubled laser pulse. The best solutions (largest fitness values) are selected as parents, which determine future populations (generation) of the algorithm. Several copies of each parent form the set of children. The children are mutated with a Gaussian noise function to perturb the solutions. The parents and mutated children are combined to form the population of the next generation. The process is then repeated until the fitness changes by an insignificant amount between generations; at this point, the process is said to have converged. This typically occurs in 50 to 100 iterations, with about 100 population members tested for each iteration. Details of this algorithm can be found in Appendix A, and settings of the algorithm used to control HHG are given in Chapter 3, while those used to control molecules are given in Chapter 4.

2.6 Summary

In this thesis, I describe the construction and application of a learning machine capable of controlling complex, nonlinear quantum mechanical systems in realistic (i.e., noisy) laboratory environments. This approach is extremely powerful in that the algorithm determines how to best control the system. Although this approach has been criticized in the past, Chapters 3 & 4 show that it is very robust and useful. By allowing the learning machine to search the parameter space for an optimal solution,

we remove experimenter bias and we show that the learning algorithm discovers new, unknown, and unexpected solutions. In other words, the learning algorithm truly can learn.

CHAPTER III

Coherent Control of Atoms: Manipulating the Process of High Harmonic Generation

3.1 Introduction

In this chapter, I discuss the application of coherent control concepts to the process of high harmonic generation (HHG). HHG is a very high-order nonlinear process, and thus is an excellent candidate system for controlling with complex, temporally shaped pulses. Unleashing a learning algorithm that controls a deformable mirror pulse shaper on HHG has proven to be successful, and has demonstrated the control of electron wavefunctions using light. This control process can be thought of as a new phase matching mechanism, and this mechanism was discovered by the learning algorithm itself. This chapter will begin with a brief description of the physics of HHG. I will then describe the control experiment, and finally the modelling results of the process.

The development of high-power femtosecond lasers [73, 69] with pulse durations of a few optical cycles has led to the emergence of a new area of research in "extreme" nonlinear optics (XNLO) [74, 75, 76, 77, 78]. High harmonic generation (HHG) is a

beautiful example of such a process. HHG can be understood from both a quantum and semi-classical point of view [79, 80, 14]. In HHG, an intense femtosecond laser is focused into a gas. The interaction of the intense laser light with the atoms in the gas is so highly nonlinear that high harmonics of the laser frequency are radiated in the forward direction. These harmonics extend from the ultraviolet (UV) to the soft x-ray (XUV) region of the spectrum, up to orders greater than 300. Because all of the atoms in the laser interaction region experience a similar, coherent light field, the x-ray emissions from individual atoms are mutually coherent.

High harmonic generation is a very interesting candidate for coherent or feedback control experiments for a number of reasons. First, the HHG x-ray emission has a well-defined phase relationship to the oscillations of the laser field [15, 81, 82], as explained below. Second, HHG is one of the highest-order coherent nonlinear-optical interactions yet observed. Third, there exist both quantum [16, 17, 13] and semi-classical [80, 14] models of HHG that, although not complete as yet, can be used to carefully compare theory and experiment. Finally, HHG is a unique type of ultrafast, coherent, short-wavelength, compact light source. This source can be used as a powerful tool for time resolved studies of dynamics at surfaces [83] or in chemical reactions, for x-ray imaging, and for generating attosecond-duration light pulses [16, 84, 77, 78]. By improving the characteristics of HHG using coherent control techniques, many potential applications are enabled and made more straightforward.

3.2 Semiclassical model of HHG

The simple semi-classical theory of HHG [79, 80, 14] considers an atom immersed in an intense, ultrashort laser pulse, where the laser pulse can be treated as a time-varying, classical electric field. At laser intensities of approximately $10^{14} Wcm^{-2}$, the optical field is so strong that the Coulomb barrier binding the outermost electron of the atom becomes depressed. Electrons can then tunnel through the barrier, leading to field-ionization of the atom. This process occurs twice per optical cycle, during that portion of the pulse for which the laser field is sufficiently strong. Once ionized, the electrons are rapidly accelerated away from the atom by the oscillating laser field, and their trajectory is reversed when the laser field reverses (see Figure 3.1). Depending on when during the optical cycle the initial tunnelling event occurs, some fraction of the ionized electrons can recollide with the parent ion and recombine with it. In this recombination process, the electron kinetic energy, as well as the ionization potential energy, is released as a high-energy photon. The x-ray emission bursts occur every half cycle ($\sim$ 1.2 fs) of the laser field for which the laser intensity is sufficient to ionize the atom. However, a particular harmonic (i.e., photon energy) may be emitted only during a limited number of half-cycles depending on the kinetic energy required to drive a particular harmonic. In the frequency domain, this periodic emission results in a comb of discrete harmonics of the fundamental laser, separated by twice the laser frequency. The exact nature of the emitted x-rays depends in detail on the exact waveform of the driving laser field, because this determines the phase accumulated by the electron as it oscillates in the laser field [81]. In

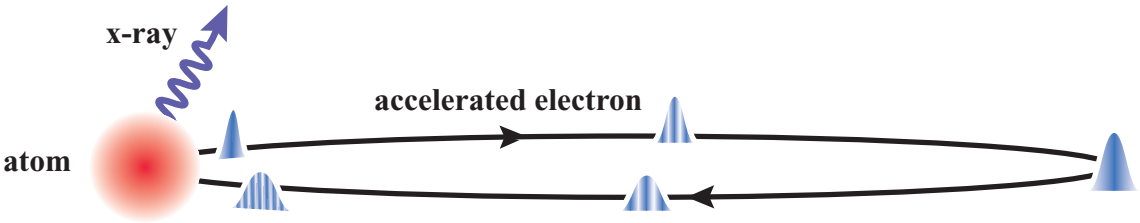

Figure 3.1: In the semiclassical picture, the electron wave packet starts from rest after tunneling out of the atom and appearing in the free-electron "continuum". The electron is accelerated in the laser field and on the subsequent half cycle, the electron is decelerated and turns around to be accelerated towards the parent ion. During this trajectory, the electron wave packet accumulates a quantum mechanical phase that is determined by the laser field. This phase can be roughly described classically as the deBroglie wavelength integrated along the electron trajectory.

this chapter, I discuss coherent control techniques where, by precisely adjusting the exact shape (waveform) of an intense ultrashort laser pulse on a *sub-cycle* basis, we can manipulate the spectral properties of the high-harmonic emission to selectively enhance particular harmonic orders, and to generate near-transform-limited x-ray pulses for the first time [11].

3.3 Quantum mechanical description of HHG

Although the simple semi-classical picture of high-harmonic generation described above is well-established and yields very useful predictions of the general characteristics of high-harmonic radiation, a more complete description requires the use of a quantum, or at minimum, a more rigorous semiclassical model of the evolution of the electron wave function [18]. In a quantum picture, the wave function of the atom in the intense laser field evolves in such a way that as the laser field becomes sufficiently strong, small parts of the bound-state electron wave function escape the vicinity of

the nucleus and are spread over many Bohr radii (≈ 100). This "free" portion of the electron wave function can recollide with the atomic core, and reflections from the core then lead to very rapid modulations of the electronic wave function, both in space and in time. The x-ray emission results from the resulting rapid fluctuations in the overall dipole moment of the atom: in the quasi-classical approximation, the phase of the induced dipole is determined by the value of the action at its saddle points. This corresponds to the contribution of the electron trajectories relevant to this particular emission. In the case of a linearly-polarized strong field, we use the following approximate expression for the dipole moment

$$d(\tau) = i \int_0^{\tau} \mathrm{d}\tau_b \left[\frac{\pi}{\varepsilon + i(\tau - \tau_b)}\right]^{\frac{3}{2}} E(\tau_b) \exp\left[-iS(p_s, \tau, \tau_b) - \gamma(\tau_b)\right], \tag{3.1}$$

where ε is a positive regularization constant, and we neglect the bare atomic dipole moments (atomic units are used here). In Eq. 3.1, we assume that the electron is ionized at a time τ_b by the electric field $E(t)$, and that it returns to the parent ion at a time τ after "free" motion in response to the laser field. Also, in Eq. 3.1, $\gamma(\tau_b) = \int_0^{\tau_b} w(t)\mathrm{d}t$, where $w(t)$ is the Ammosov-Delone-Krainov [85] tunneling ionization rate, and

$$p_s(\tau, \tau_b) = -\frac{1}{\tau - \tau_b} \int_{\tau_b}^{\tau} A(t')\,\mathrm{d}t'$$

is the stationary momentum, for which the quasiclassical action

$$S(p_s, \tau, \tau_b) = \int_0^{\tau} \left\{\frac{1}{2}\left[p_s + A(t)\right]^2 + I_p\right\} \mathrm{d}t \tag{3.2}$$

has saddle points that correspond to the most relevant electron trajectories. Here $A(t)$ is the vector potential, I_p is the ionization potential.

3.4 Classical trajectory analysis

In the quantum picture, it is clear that the phase of the dipole moment of the atom, and therefore the phase of the electric field of the emitted x-rays, depends on the accumulated phase of the electronic wave function that travels away from the core and then returns. In a simple semi-classical picture, the phase advance of the electron during the half-cycle trajectory can be estimated from the deBroglie wavelength $\lambda_{deBroglie} = \frac{h}{mv}$ to correspond to several "cycles" of the electron wave function (e.g., for the 27^{th} harmonic in Argon, the kinetic energy upon recollision is 26 eV, corresponding to a velocity of 3 nm/fs, and a deBroglie wavelength of 2.4 Angstrom, and accumulates about 5 waves of phase). With this in mind, the potential for using precisely-shaped driving laser pulses for "coherent control" of this system becomes more clear. Modest changes in the exact position of the crests of the driving pulse as a function of time — that occur on a sub-optical-cycle or attosecond time-scale — can result in a substantial shift in phase of the x-ray burst that results from a single half-cycle of the laser field.

We can solve the equations of motion for an electron driven by a sinusoidal electric field to obtain a picture of the electron trajectories in the classical picture [79]. Figure 3.2 shows a simple example of electron motion in a fixed-intensity field of $2\text{x}10^{14} W/cm^2$. HHG radiation is emitted when the electron returns to its initial location, and the electron velocity (i.e., kinetic energy) determines the generated harmonic wavelength. The distribution of harmonic order emitted as a function of ionization time in the driving field is shown in Figure 3.2(b). This ionization

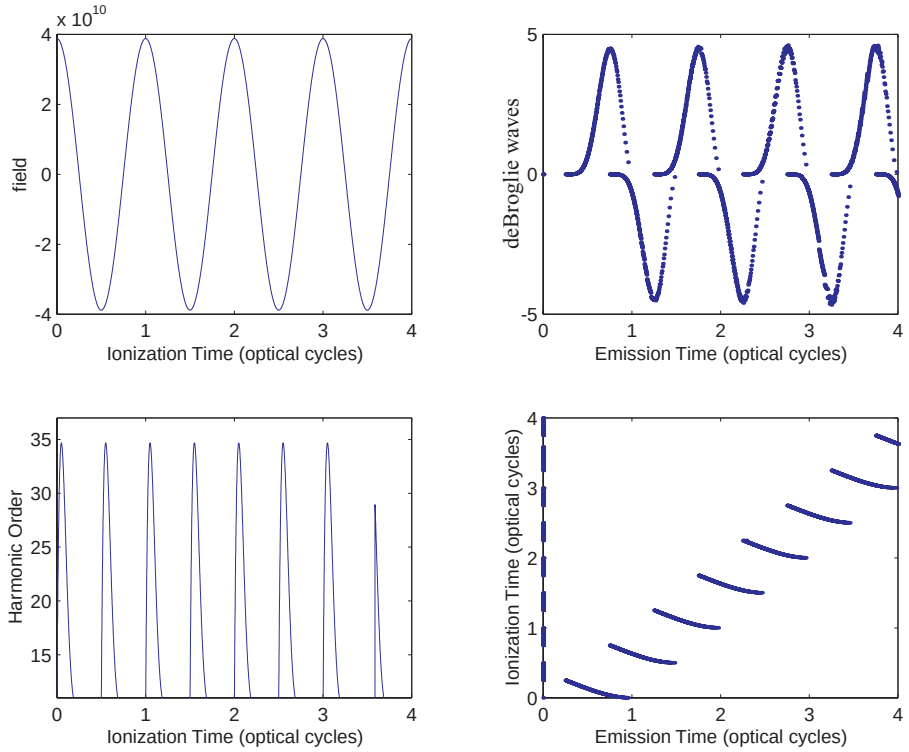

Figure 3.2: Classical behavior of electron trajectories driven by a sinusoidal electric field (a). The return energy determines the harmonic order of the released photon energy (b) at its corresponding emission time. The self-action phase is calculated by integrating the deBroglie wavelength along the trajectory of the electron and is plotted in terms of the number of deBroglie waves (c), and the relationship between the ionization and emission times (d) shows that the electrons spend a fraction of an optical cycle in the laser field.

time determines the return kinetic energy, and therefore, the harmonic order of the emitted photon.

The recollision time is also a function of ionization time (and harmonic order) and this relationship between the ionization time and the recollision time is plotted in Figure 3.2(d). We can see that there is a variation in the emission time with respect to the ionization time, which means there is a relationship between the harmonic order and the length of time the "free" electron spends in the laser field.

The duration of the "free" trajectory of the electron in the light field is called the excursion time, and is found by taking the difference between the emission and ionization time. The excursion time for this simple driving field is illustrated in Figure 3.3. Notice that at the cutoff (i.e., the maximum harmonic energy), there is only one excursion time, and therefore, one trajectory. However, every harmonic other than the cutoff has contributions from both a "long" and a "short" electron trajectory.

The phase accumulated by the electron wavfunction is calculated by integrating the deBroglie wavelength along the electron trajectory ($\phi_{deBroglie} = \int k_{deBroglie}(x)dx$ where $k_{deBroglie}(x) = \dfrac{2\pi}{\lambda_{deBroglie}(x)}$ where x is the path variable of the electron trajectory) is shown from each emission time in Figure 3.2(c), and as a function of harmonic order in Figure 3.4. We see that the phase accumulated by the electron is maximum for the cutoff harmonic, since these electrons have the shortest deBroglie wavelength, and, therefore, most rapidly accumulates phase, as well as have the longest excursion time of any harmonic.

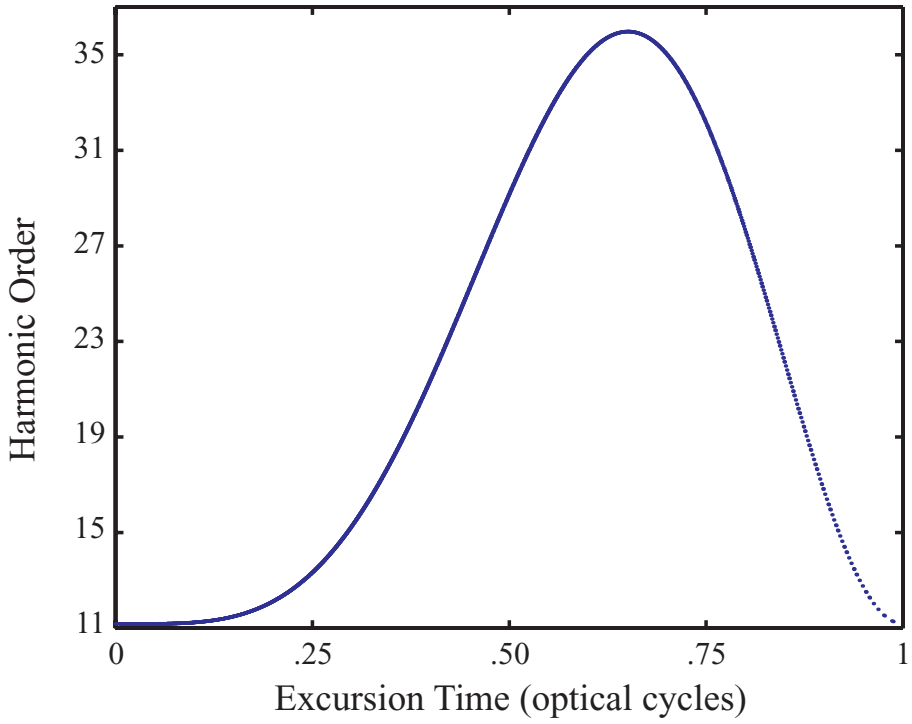

Figure 3.3: Excursion time duration of the electron trajectory calculated by taking the difference between the emission and ionization times.

We can view the time each harmonic spends in the laser field (or "flight time") by plotting both this ionization and emission times as illustrated in Figure 3.5. The short trajectories illustrated in Figure 3.5(a) are shown to increase their excursion time with harmonic order, while the long trajectories experience a decrease in excursion time with increasing harmonic order.

The flight times for the short trajectories that recollide and emit photons with the energy for the 25^{th}, 27^{th}, and 29^{th} harmonic orders are shown in Figure 3.6. There is nearly complete overlap of the time spent in the laser field between these harmonic orders, yet we show in later sections of this chapter that we selectively increase the brightness of the 27^{th} harmonic by nearly an order of magnitude. In light of this picture, it seems surprising. The important parameter for control will be shown to

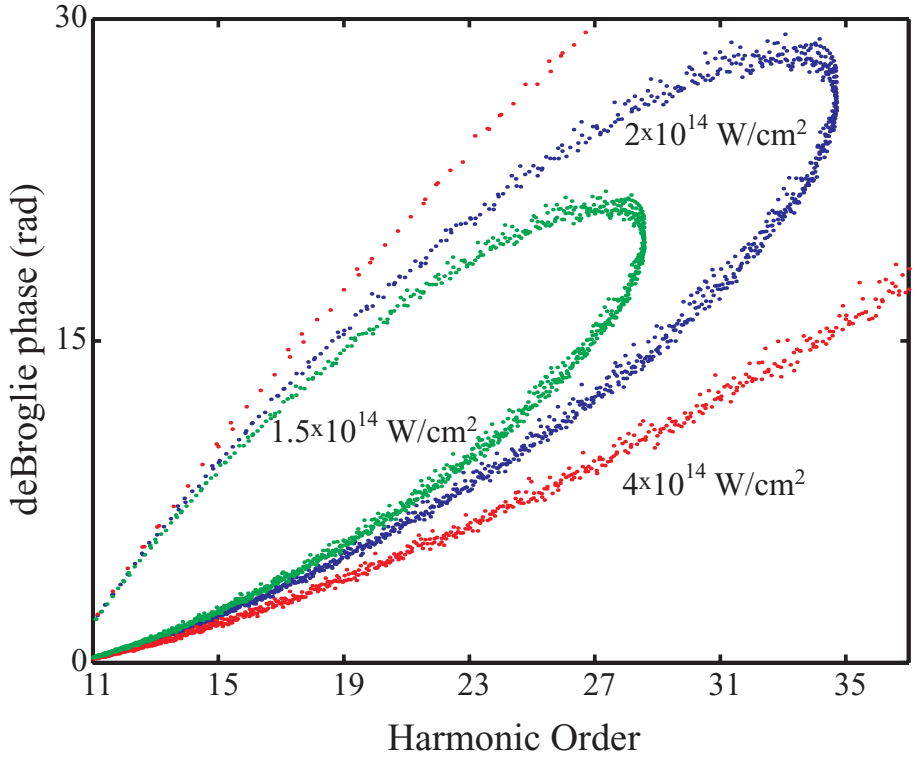

Figure 3.4: The "deBroglie phase" of the electron accumulated during the electron trajectory. This is the classical interpretation of the electron wave packet phase accumulated by the electon during its "free" trajectory. In the classical interpretation, this phase is computed by integrating the k-vector of the deBroglie wavelength along the path of the electron. The deBroglie wavelength is "chirped" in that the wavelength is not constant along its "free" trajectory path. For example, at the turning points, where the direction is reversed, the wavelength is infinite. The total number of deBroglie waves can, however, be computed by dividing the phase accumulation by 2π. The "short" trajectory spends less time in the laser field, and accumulated a smaller deBroglie phase than the "long" trajectory. Thus, the bottom portion of the phase distribution corresponds to the "short" trajectory, and the top to the "long" trajectory. Notice that the phase depends on the peak intensity of the half-cycle, and, therefore, is not the same on each half-cycle of the driving laser pulse.

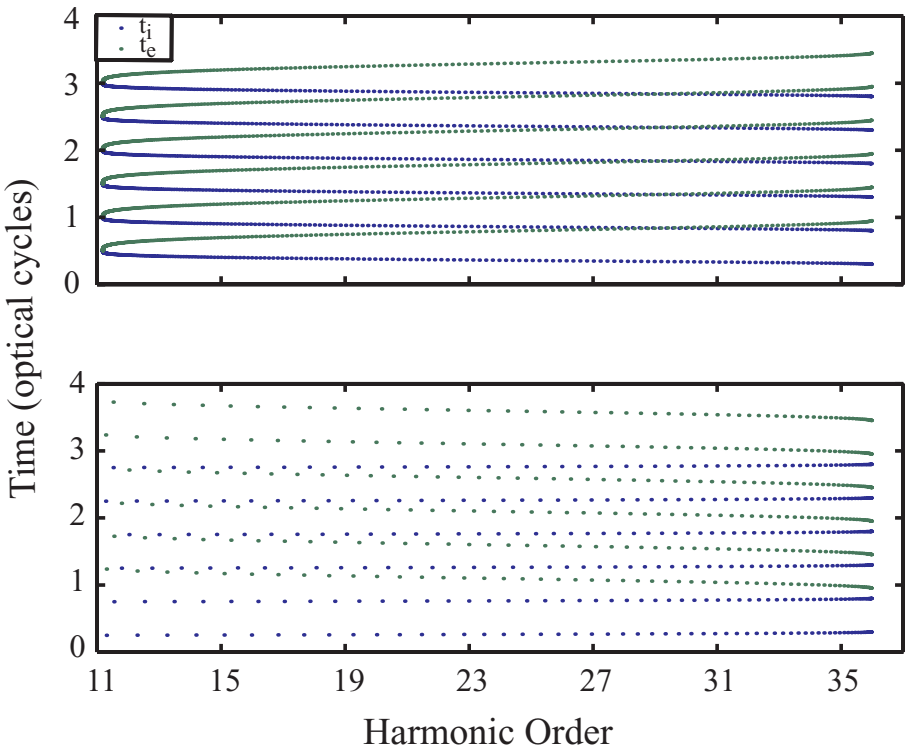

Figure 3.5: The ionization (blue) and emission (red) times for the short (a) and long (b) trajectories contributing to HHG generation.

be the free electron wave packet phase. Note that the rate of phase accumulation varies during the electron trajectory. For example, near the turning points (i.e., the stationary points), where the electron slows down and reverses direction, the rate of phase accumulation is nearly zero. As a result, although most of the time that each neighboring electron trajectory spends in the laser field is coincident, the range of time over which the electron wave packet is effectively controlled is not the same for each harmonic, making selective control possible. We do expect there to be some coupled behavior between harmonic orders as the pulse shape is changed. This coupling is observed in correlations between neighboring harmonics with nearly optimal pulse shapes in a later section of this chapter.

This classical trajectory analysis gives us an intuitive classical representation for the important control parameters for the manipulation of the HHG process. To calculate reliable, quantitative information, a more sophisticated formalism is used in a later section; however, this analysis shows that, we expect some selective control among harmonic orders to be possible.

3.5 Finite time response

The preceding sections outline the features of HHG that allow us to manipulate the properties of emitted HHG radiation from a single atom. This raises a fundamental question as to why it is possible to tailor the nonlinear polarization that leads to HHG. In low-order electronic nonlinear optics, the response time of the nonlinearity is essentially instantaneous. As a result, the polarization depends only on the instantaneous driving fields, and not on a history of the field. The phase of the

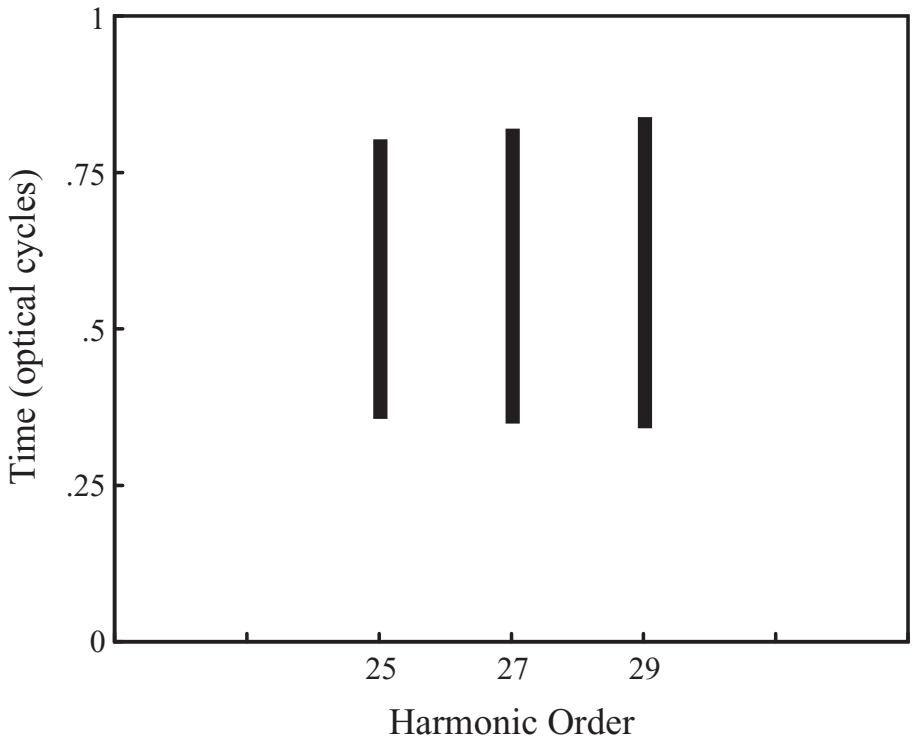

Figure 3.6: Flight time of the 25^{th}, 27^{th}, and 29^{th} for the short trajectories.

nonlinear polarization is transferred to the radiated light at the harmonic frequency. To maximize conversion to the new color, all of the radiation emitted during the driving pulse must be in phase and add together constructively. The simplest way to meet this condition is to use a transform-limited pulse, because the phase across the pulse is "flat."

A notable exception to the instantaneous response of perturbative nonlinear optics was observed by Yaron Silberberg's group [58]. In a two photon absorption (TPA) experiment with an intermediate resonance, Silberberg's group showed that a non-transform-limited laser pulse can increase the TPA absorption by a factor of 7 with a shaped laser pulse, even when the peak intensity of that laser pulse was reduced. To excite TPA, pairs of photons within the laser pulse bandwidth must

sum together to equal the electronic transition frequency. When the TPA system lacks a resonance, the photon pairs must arrive simultaneously, and this condition is guaranteed for a transform-limited laser pulse. However, when an intermediate resonance is present, population can be transferred to the intermediate electronic state and is stored here for a finite time, creating a "memory" effect. Photons absorbed by the intermediate resonance experience a storage time inversely proportional to the detuning from the resonance frequency. Because of this "memory," photon pairs that sum to the TPA frequency no longer need to arrive at the same time in the pulse. They can now be separated by a time equal to or shorter than the "storage time" of a given photon frequency. As a result, a non-transform-limited laser pulse produced more TPA absorption than does a transform-limited laser pulse.

Equations (3.1) & (3.2) show that the nonlinear polarization for HHG is not instantaneous, and depends on the cumulative effect of the driving field over the *sub-cycle ($< fs$)* time of its excursion. The result is that the phase of the HHG radiation during the pulse is not a direct reflection of the driving pulse phase, but depends on the time-history of the driving pulse phase and intensity during its excursion. As a result, a transform-limited pulse is not optimal, because it will imprint an irregular phase on the HHG radiation. Thus, the selectivity of a particular order is "engineered" in the system through pulse shaping. The effect of the phase change on each half-cycle could be eliminated using a "flat-top" pulse, but this would not be selective among harmonic orders. A time-varying intensity, combined with a time-varying pulse phase can give counter-balancing factors that can be manipulated for

selectivity. Although the attosecond time scale of this response might be thought to make it difficult or impossible to coherently control the process, in fact, the very high order-nature (i.e., extreme phase sensitivity) of this process gives us a "lever" with which we can control the phase evolution of the process with very subtle changes in the driving pulse shape.

3.6 Early attempts of HHG control

In the simple case where high-harmonic generation is driven by an unchirped, transform-limited, laser pulse, the HHG light generated on the leading edge of the pulse, where the driving pulse intensity is rising rapidly, will be emitted with an intrinsic negative chirp. This is because the electrons released on each subsequent half-cycle traverse an increasingly longer path away from the atom, resulting in a larger phase-shift of the electron wave function at the time of recollision, and travel faster, resulting in a more energetic recollison and thus a shorter x-ray wavelength. This results in a spectral broadening of the peaks in the HHG emission spectrum [15, 81]. Imposing a positive chirp on the driving laser pulse can counteract this intrinsic negative phase, restoring a series of well-defined harmonic emission peaks in the spectrum, as illustrated in Figure 3.7. In this past work, where a simple linear chirp is applied to the excitation pulse, all harmonic orders were observed to behave similarly in terms of spectral widths, and the overall x-ray flux does not increase. Attempting to control HHG with a linearly chirped laser pulse did not result in a substantial increase in HHG intensity or flux, nor did it exhibit selectivity among harmonic orders.

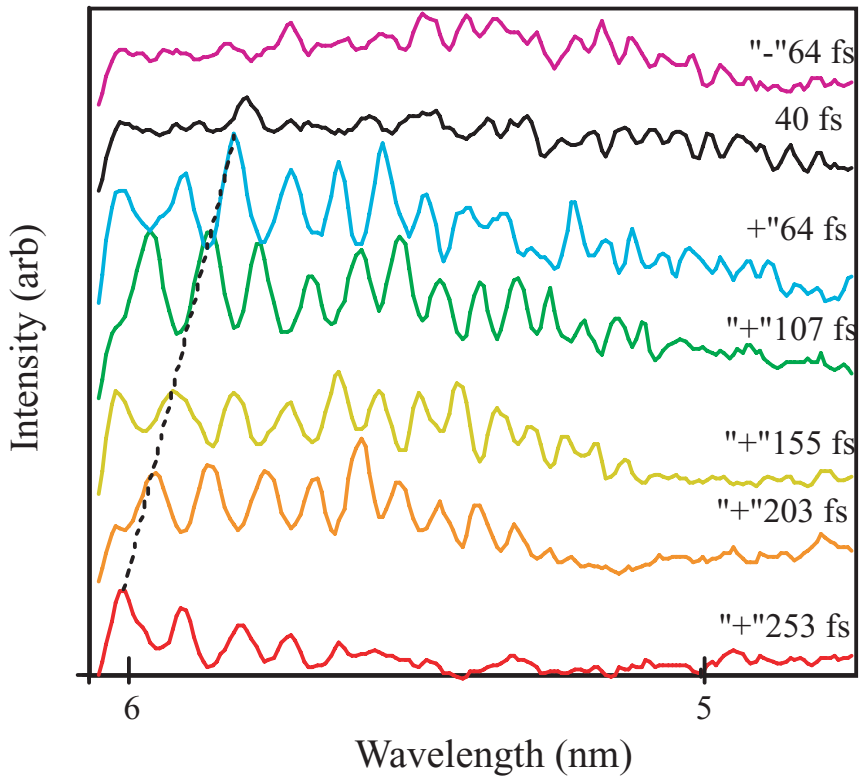

Figure 3.7: HHG spectrum in Helium as a function of driving laser pulse duration [81]. The pulse duration is controlled by adjusting the linear chirp of the pulse. We see that for a positive chirp, the harmonic structure becomes well-resolved, while the structure is degraded for a negatively chirped driving laser pulse.

Although past work that studied HHG excited by simple linearly chirped pulses has proven very useful in understanding the fundamental processes involved, theoretical models of HHG predict that the intrinsic chirp resulting from the electron trajectory is not in-fact linear. By altering the shape of the driving laser pulse in a more sophisticated manner using a pulse shaper [69, 86, 71], one can expect to be able to manipulate the spectral characteristics of the XUV emission more precisely. In this work, however, we demonstrate that coherent control can manipulate the process in ways that are much more powerful than was originally thought. By adaptive feedback control of the pulse shape using an evolutionary algorithm [69, 3, 59, 2], we demonstrate experimentally that we can not only control the spectral characteristics of high-order harmonic generation (HHG), but also can very-substantially enhance the overall brightness of the HHG emission *in a selective fashion.*

3.7 HHG Control Experiment

The process of high-harmonic generation is best implemented using very short-duration ($\ll$ 100 fs) light pulses, since these pulses allow a relatively high intensity to be incident on a neutral atom prior to ionization, resulting in more-efficient generation of higher-energy harmonic photons [87, 88, 89]. Furthermore, to make coherent control practical, the number of trajectories should be limited to a small number (10). In this work, the driving pulse shape is manipulated using the deformable mirror described previously. Although this type of pulse shaper is limited in that it is a "phase-only" shaper and cannot alter the spectrum of the driving pulse, this has not been proven to be a significant limitation in controlling a highly-nonlinear

process such as high-harmonic generation. Color-components that are not wanted can always be moved to early or late times within the pulse where no HHG is taking place.

The difficulty of calibrating the pulse shaper to generate a predetermined pulse shape, as well as the uncertain accuracy of theoretical models that might predict an optimum pulse shape, make a "one-step" optimization of the HHG process (i.e., predict an optimum pulse shape and program it into the pulse shaper) both impractical and undesirable. Instead, we implemented a learning algorithm to train the laser system to optimize the high-harmonic emission.

This scheme requires a large number of repeated trials, which is possible in a reasonable time because of the high photon flux generated through phase-matched high-harmonic generation [90, 91]. In phase-matched frequency conversion, an environment is created where both the fundamental and the harmonic radiation travel through an extended medium at the same phase velocity. This allows the nonlinear signal of all atoms within this region to add coherently and constructively, enhancing the output signal. *Phase matching is characterized by a reduction of destructive interference in order to increase total harmonic signal levels.* In conventional nonlinear optics at visible wavelengths, phase-matching is typically accomplished using a birefringent crystal oriented such that the pump beam (in one polarization) and the signal (in another) travel at the same speed. In the case of high-harmonic generation, the XUV light propagates in a low-pressure, isotropic gas, precluding the use of birefringence effects. Instead, we propagate the light in a waveguide structure (simply a

hollow capillary tube), and use the frequency-dependent phase velocity of the waveguide, in combination with the gas dispersion, to achieve phase matching. In the case of phase-matched high-harmonic generation, the total conversion efficiency is still limited by effects such as the strong absorption of the HHG radiation in the gas, and the effects of ionized electrons on phase-matching. Nevertheless this technique allows us to achieve conversion efficiencies of $\sim 10^{-5}$ to photons energies of $\sim$50 eV, while also using a kilohertz repetition-rate, millijoule pulse-energy laser system. The resulting flux is sufficient to obtain a high signal-to-noise high-harmonic spectrum in a single shot using a flat-field x-ray spectrometer. In practice, our apparatus can try $\sim$100 different pulse shapes per second. Equally important, since the output signal we observe results from an in-phase coherent addition of individual atomic responses, many effects and distortions of the pulse spectrum that might result as a result of propagation are minimized. Essentially, phase-matching allows us to approach the "single atom" response to the driving laser.

To demonstrate that the evolutionary algorithm selects a pulse shape unique to optimizing the high-harmonic generation, we preceded each HHG optimization run with a pulse-duration optimization. This allows us to start with a time-bandwidth-limited pulse, and see how the HHG optimized pulse differs from it. The time-bandwidth limited pulse is obtained by using the evolutionary algorithm with a feedback signal derived from second-harmonic generation of the pulse [69, 71, 92, 93, 7]. A fraction of the laser output is sent into a second-harmonic crystal. The conversion efficiency of the SHG increases with the peak intensity of the fundamental

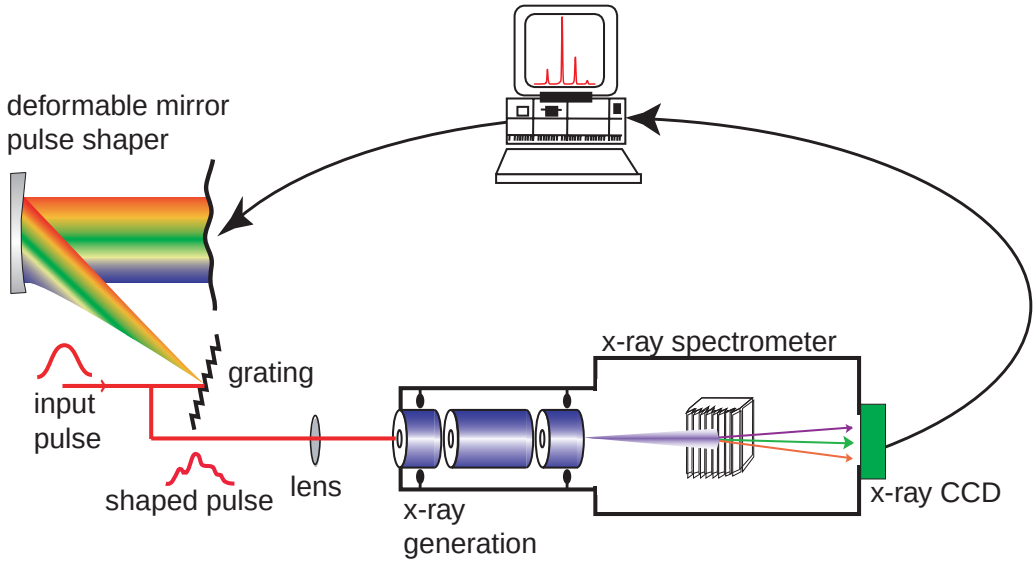

Figure 3.8: Experimental set-up for optimization of high-harmonic generation.

pulse; thus the most intense pulse, which occurs when all component frequencies of the pulse have the same relative arrival time, produces the largest fitness value and corresponds to the Fourier transform-limited pulse. This computer optimization converges after about 100 generations of about 100 trials each (10,000 total "experiments"). This optimization takes ∼10 minutes of real time, and converges very well to a transform-limited pulse, as was verified by making FROG measurements on the pulse.

Subsequent to this optimization, the HHG optimization is performed. The set-up is shown in Figure 3.8. The x-ray output from a hollow core fiber is passed through a 100 nm aluminum filter to eliminate the fundamental IR beam, while passing photon energies up to 72 eV. An imaging x-ray spectrometer (Hettrick SXR-1.75) was used to image the spectrum onto an x-ray CCD camera. (Andor Technologies) A computer reads-in the HHG spectrum and evaluates the fitness criterion. The fitness functions used to evaluate the harmonic spectrum will differ depending on the goals

of the optimization process. A particular harmonic is designated as the spectral flux (s_j) integrated over a 0.5 eV bandwidth about that harmonic (corresponding to the resolution limit of our spectrometer/CCD system). Table 3.1 lists a number of fitness functions we used for various optimization goals. The simplest fitness criterion to use is simply to observe the peak intensity of a single harmonic order (Table 3.1(a)). Alternatively, it is possible to select for enhancement primarily of only one harmonic order (Table 3.1(c)). Figure 3.9 shows the result of such an optimization at 30 torr of Argon gas pressure in a 175 μm diameter fused silica capillary 29 mm long [11]. This pressure is optimum for phase matching in this geometry. We see that the intensity of the 27^{th} harmonic can be increased by a factor of eight over that obtained using a transform-limited pulse. Furthermore, the brightness of other harmonic orders does not increase as much, and the spectral bandwidth of the harmonic order decreases. This is very desirable for application experiments such as time-resolved photoelectron spectroscopy that require monochromatic emission.

Various fitness functions used by the learning algorithm			
	Goal	Form	Notation
(a)	Increase brightness	$f := (s_{j,k} : s_{j,k} \geq s_{j,i} Vi)$	M_j
(b)	Increase energy	$f := \sum_i s_{j,i}$	E_j
(c)	Select a single harmonic	$f := E_j - \frac{1}{2}(E_{j-2} + E_{j+2})$	
(d)	Select a single harmonic	$f := M_j - \frac{1}{2}(M_{j-2} + M_{j+2})$	

Table 3.1: Various fitness functions used by the learning algorithm; s_j refers to the j^{th} harmonic spectrum. (a) finds the maximum value of a given harmonic order, (b) finds the energy of a given harmonic order with summation over i, (c) selects a single harmonic order with an energy criterion, and (d) selects a single harmonic order with a brightness criterion.

The result discussed above is remarkable in that we have shown that although second-harmonic emission is optimized using the highest peak-power, transform-

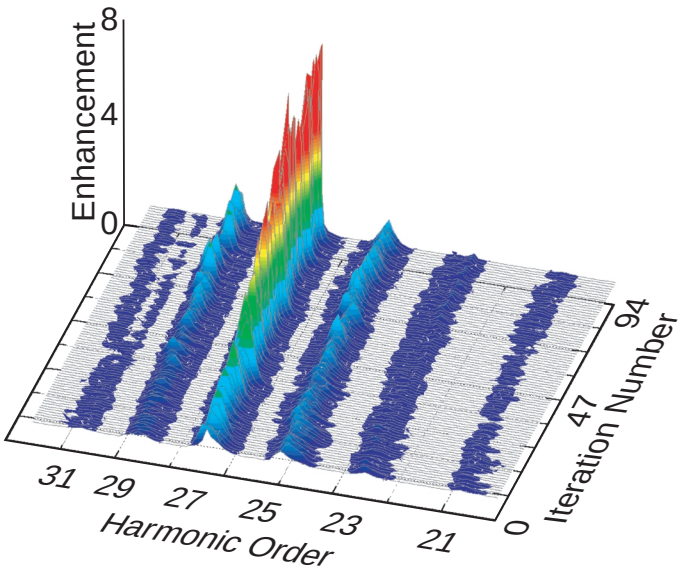

Figure 3.9: Optimization of a single (27^{th}) harmonic in argon while suppressing adjacent harmonics.

limited pulse, high-harmonic emission is optimized with a non-transform limited pulse. This is a manifestation of the fact that HHG is fundamentally a non-perturbative process — slight changes in pulse shape can "channel" excitation from one harmonic order to another.

The optimized pulse shape is actually only slightly different from the transform-limit—21 fs as opposed to the 18 fs transform limit. Figure 3.10 shows the laser pulse shapes corresponding to the transform-limited and final (iteration number 94) HHG spectra shown in Figure 3.9 measured with SHG FROG. The intensity profile of the optimized and unoptimized pulses is nearly the same (Figure 3.10). However, a slight pre-pulse appears on the leading edge of the optimized laser pulse. The intensity of this pre-pulse is too weak to lead to ionization or HHG, and is an artifact

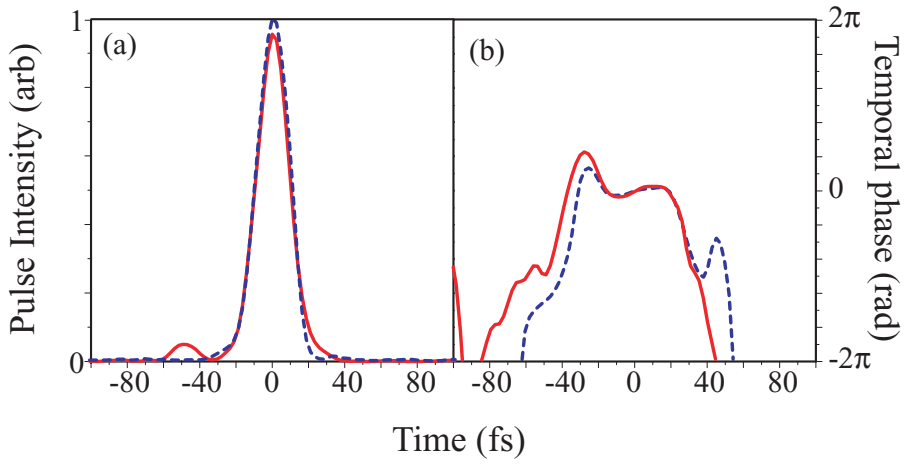

Figure 3.10: Amplitude and phase of the optimal laser pulses corresponding to Figure 3.9: (a) initial transform-limited pulse (dashed) and optimized pulse shape (solid); (b) initial (dashed) and optimized temporal phase (solid).

of our pulse shaper. The intensity profile does not produce significant changes in the HHG spectrum, but there is a change in the temporal phase on the optimal pulse that results in the observed spectral changes. In the region of time where there is significant pulse energy, the transform-limited pulse has a flat phase, while the optimal pulse has a small, but highly nonlinear temporal phase across the pulse. As explained below, it is this very slight change in the pulse used to drive the HHG process can result in a substantial and beneficial change in the output energy, brightness, and spectrum of the HHG radiation.

Other fitness criteria select different optimal outcomes. Figure 3.11 shows the results of an optimization run in which the brightness of the 27^{th} harmonic is used as the fitness criterion. In this solution, the brightness of the harmonic is increased by more than an order of magnitude. The spectral resolution of the measured spectral width shown in Figure 3.11 is instrument limited at 0.24 eV FWHM. A spectral comb produces a pulse train in time, where the time-duration of each spike in the

pulse train is determined by the number and spacing of frequency comb lines. The number of pulses in the pulse train is determined by the width of each line in the frequency comb. The spectrum in Figure 3.11 has an overall bandwidth of ∼6 eV and a comb line width of ∼0.24 eV, which corresponds to a Fourier transform-limited pulse train with a time-envelope of ∼5 fs with 200 as structure. Before optimization the bandwidth of this harmonic peak was $>$ 1 eV, with roughly the same overall bandwidth, but corresponds to a transform-limited pulse train envelop of $\sim$ 1.2 fs. Simulations predict that a 5 fs pulse train will be produced by a 20 fs driving pulse. By applying a nonlinear chirp on the optimum pulse shape, the spectrum was reshaped in a way that made the Fourier transform of the measured spectrum consistent with the time-domain structure expected from our simulations. Thus, the optimization process can likely generate near-transform-limited x-ray pulses for certain fitness criteria.

Figure 3.12 shows the highest enhancements we have observed to date. Here, the 21^{st} harmonic is observed to increase by a factor of 33 when excited by an optimized pulse compared with a transform-limited excitation pulse [12]. This large enhancement is possible because no selectivity requirement has been imposed. As a result, the algorithm finds a pulse shape that optimizes each harmonic order. In later sections, we show that the selective optimization is a result of the flattening of the relative phase of x-ray radiation from each half-cycle for the target harmonic. Because we can achieve higher optimization enhancements for a non-selective criterion, it seems that flattening many of the plateau harmonic phases is easier than to do it in

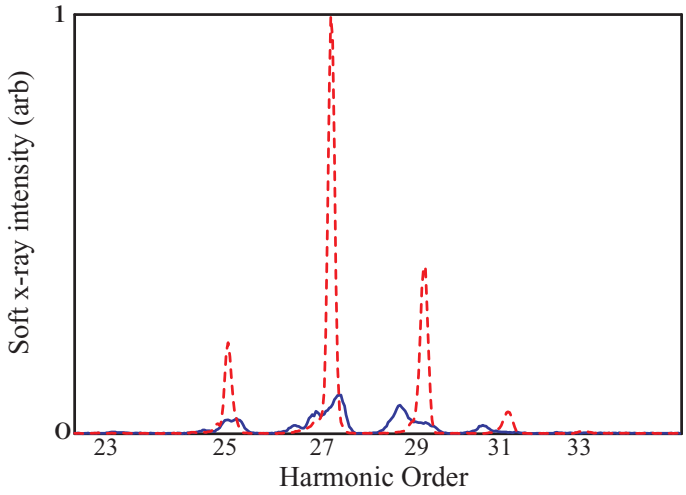

Figure 3.11: A spectrum consistent with nearly transform-limited x-ray generation obtained by optimization of a harmonic order in argon with a spectral window at longer wavelengths than in Figure 3.9 and without suppressing adjacent harmonics. The harmonic peak is enhanced by over an order of magnitude. Harmonics before and after optimization are shown solid and dashed respectively.

a selective manner.

Although the data of Figures 3.11 and 3.12 show the highest enhancement observed in our experiments to date, all harmonics optimized in any noble gas we observe some enhancement of the x-ray signal after optimization. As an example, Figure 3.13 shows the results of a series of experiments in which successive individual harmonic orders (17-23) were optimized in Krypton at a pressure of 4 torr. The fitness function used for these harmonics is that of Table 3.1(d). Each harmonic order optimization was successful to varying degrees with brightness increases from 1.7 to 6 and increases of the energy in the optimized harmonic order from 5 % to 220 % [12]. To distinguish between the optimized pulses corresponding to the series of harmonics shown in Figure 3.13, a Wigner distribution (a type of time-frequency representation of the pulse) can be used. We observe that the optimal pulse shape

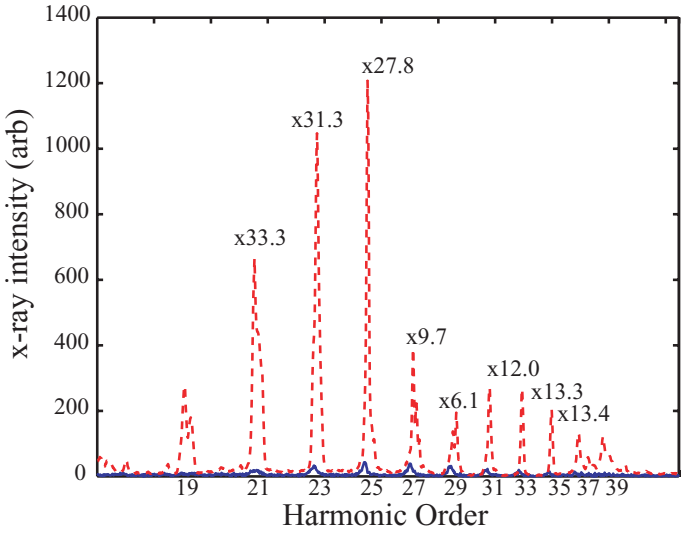

Figure 3.12: Highest enhancements observed to date. The 21^{st} harmonic is observed to increase by a factor of 33 when excited by an optimized pulse compared with a transform-limited excitation pulse. Harmonics before and after optimization are shown solid and dashed respectively.

results from spectral phase changes in different spectral regions of the pulse for each optimization of Figure 3.13.

As the energy of the driving laser pulse increases, the x-ray emission becomes stronger and then eventually saturates, as shown in Figure 3.14(a). This saturation is accompanied by a reduction in the rms fluctuations of the x-ray output, as shown in Figure 3.14(b). Also plotted on this figure is the peak enhancement factor of a single harmonic order as a function of driving pulse energy. At low pulse energy, the enhancement factor is very weak. However as the pulse energy increases, the enhancement factor also increases. Once the HHG process saturates, the driving laser pulse can be stretched to a longer duration while still having sufficient intensity to create the necessary harmonic orders, providing freedom to change the pulse shape or waveform in order to optimize the harmonics. By contrast, prior to saturation,

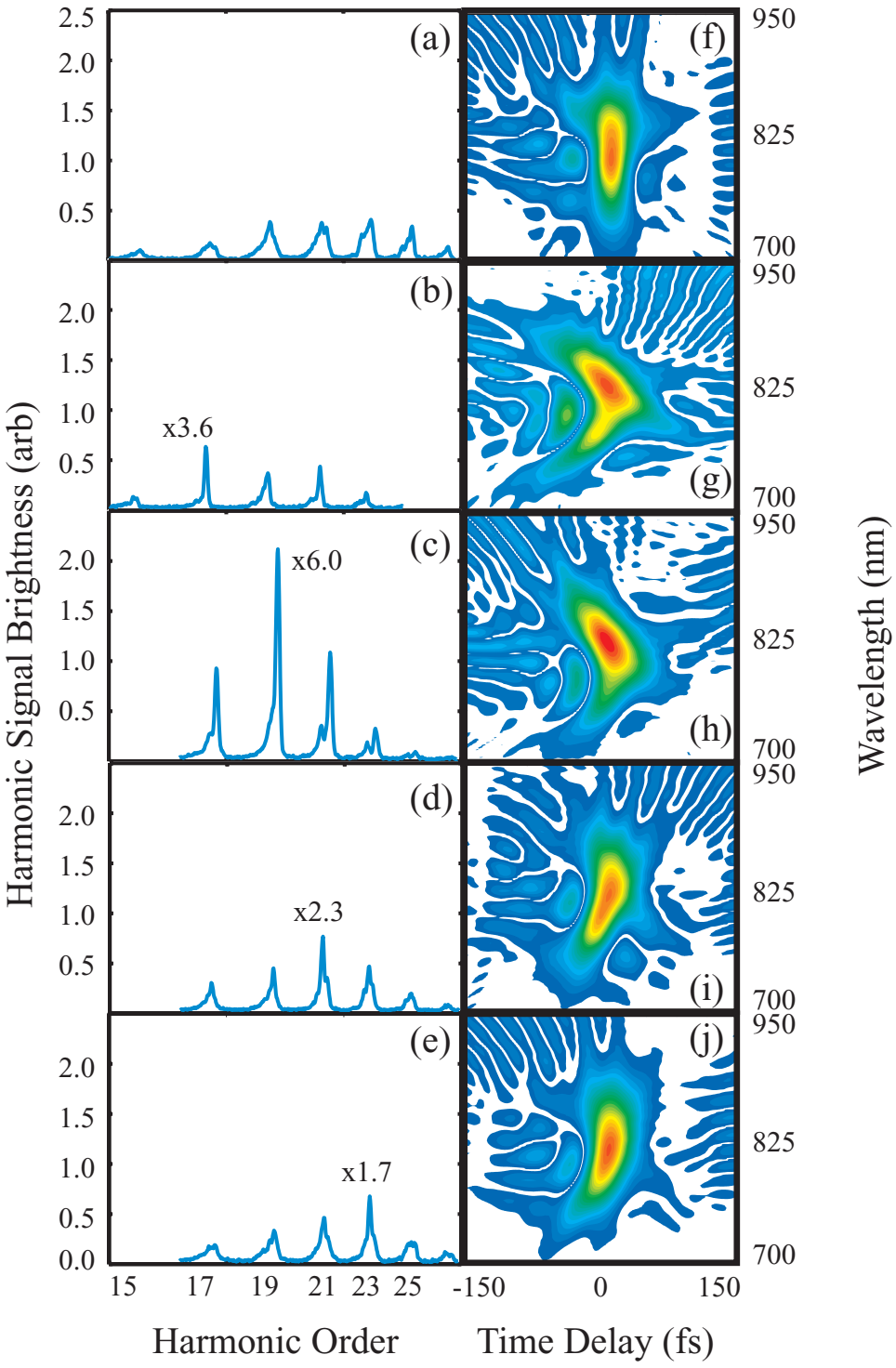

Figure 3.13: Sequence of optimizations performed in Kr for adjacent harmonics (17-23). Measured harmonic spectra for the transform limit (a) and after optimization with the fitness criterion in Table 3.1(d) for the 17^{th} (b), 19^{th} (c), 21^{st} (d), and 23^{rd} (e) order harmonics. The Wigner distributions for the measured transform limited and optimal pulse shapes are shown in panels (f)- (j) next to their corresponding spectra.

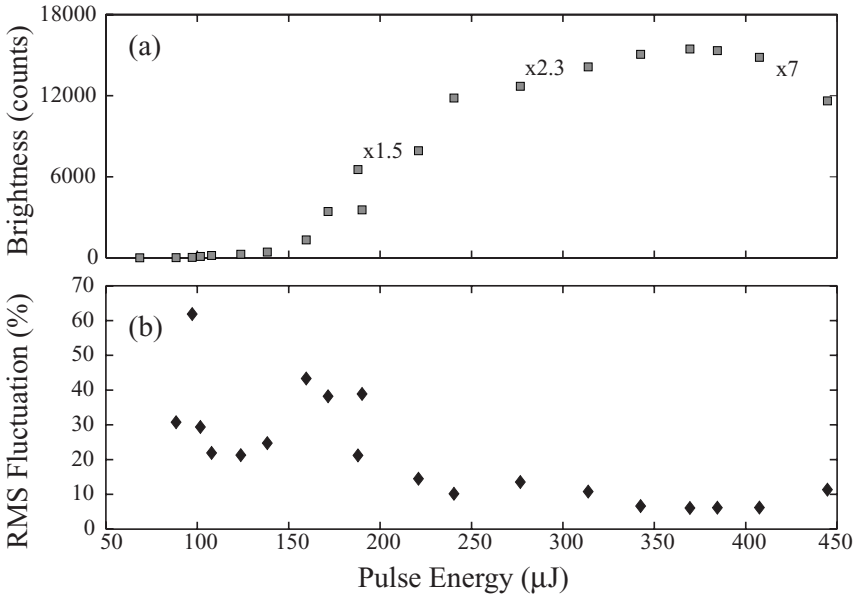

Figure 3.14: Dependence of optimization of laboratory noise. X-ray emission as a function of driving laser energy for an optimal laser pulse shape along with brightness enhancement factors of the 29^{th} harmonic in argon as a function of driving pulse energy (a), and corresponding RMS fluctuations of the x-ray output, as a function of driving laser intensity (b).

the necessary pulse shape changes to the driving laser pulse often reduce the peak intensity of the pulse sufficiently such that the particular harmonic order can no longer be generated.

3.8 Theory of HHG Optimization

In collaboration with Ivan Christov, we have developed a successful theoretical model of this HHG optimization process that explains the physical basis of the optimization [13]. Using this model, we show that a new type of "intra-atom" phase matching is possible as a result, where an atom is driven by an optimal optical waveform. For an optimized laser pulse shape, the x-ray emissions from adjacent half-cycles of the laser pulse can add in phase. This leads to strong constructive

interference in the frequency domain between emissions from electron trajectories from different half-cycles, thereby selectively enhancing a particular harmonic order. This mechanism is based on the interaction of a short pulse with a single atom—in contrast to traditional phase matching techniques that depend on propagation effects.

This model is a highly optimized version of the Lewenstein model [18] that calculates HHG spectra in a semiclassical approximation. We apply a learning algorithm to the model, which runs at speeds comparable to the experiment, and which applies the same fitness functions to the HHG emissions as in the experimental optimization. The model predicts an optimized pulse shape and emission spectrum that is very close to the experimental results — in the case of selective optimization of a single peak, for example, an enhancement of ∼8x is predicted (Figure 3.15), using an optimized laser pulse shape slightly longer than the transform limit. Figure 3.16 shows the experimental and calculated optimized laser pulse shapes, together with the corresponding phase. There is excellent agreement, with both pulses exhibiting a nonlinear "chirp" on the leading edge. Harmonic radiation is generated throughout the duration of the driving laser pulse during the time when the intensity is sufficient to ionize and accelerate the electrons to high velocity. However, during the course of the laser pulse, the ionization steadily rises. The increased level of ionization on the trailing edge of the driving laser pulse destroys the phase-matching conditions. The loss of phase-matching means that only the HHG radiation generated on the leading edge contributes strongly to the overall signal level. As a result of the weak

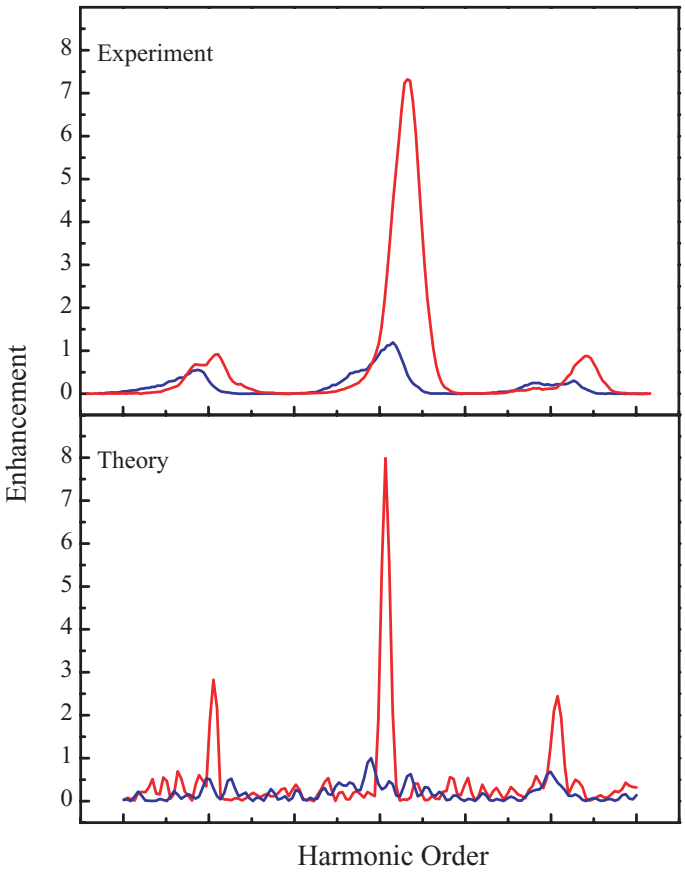

Figure 3.15: The measured HHG spectra for the transform-limit (blue) and optimized pulse (red) (a) is well reproduced by the HHG spectra calculated by our theoretical model the for the transform-limit (blue) and optimized pulse (red) (b).

contribution to the HHG signal from the trailing edge of the pulse, the temporal phase of the optimal pulse the trailing in either the experimental or theoretical case is random, and the fitness functions do not select any particular shape for the trailing edge of the pulse.

This model is a novel theoretical approach to high-harmonic generation that couples a fully quantum model of the electron response with a semiclassical electron trajectory picture. In the quasiclassical model, the x-ray emission results from rescattering of an electron, ionized in a strong laser field, with its parent ion. In

our approach, each harmonic order appears as a result of a constructive or destructive interference of the contributions of a number of rescattered electron trajectories. Since the amplitude and the phase of the contribution of a given electron trajectory to the dipole moment is directly related to the amplitude and the phase of the laser field at the time of ionization, it is intuitively clear that by shaping the waveform of the laser pulse, one may control the interference effects in the x-ray emission that comes from these different electron trajectories. In this way, a significant redirection of energy between the different harmonics within the harmonic comb is possible. Such improvements are not possible by simply changing the linear chirp of the driving laser pulse, as has been demonstrated previously [81]. We note that the results presented here do not take into account propagation effects. This is a reasonable assumption since we use a phase-matched geometry [90, 91]. When the HHG process is phase matched, the fundamental light is made to propagate at the same velocity as the HHG light, and prevents a relative phase-slip between HHG radiation generated from different atoms at different locations in the fiber. Thus, the phase-matching geometry effectively minimizes the effect of an extended source region on the HHG signal (with the exception of absorption of the HHG radiation) where propagation effects are smaller than the single-atom effects considered here.

We use Equations (3.1) & (3.2) to calculate the dipole phase and intensity in time, then the dipole acceleration is Fourier transformed to obtain the HHG spectrum. We assume that the degree of ionization is low, in agreement with the experiment [11]. The integral in Eq. (3.1) can be converted to a sum by calculating the saddle points of

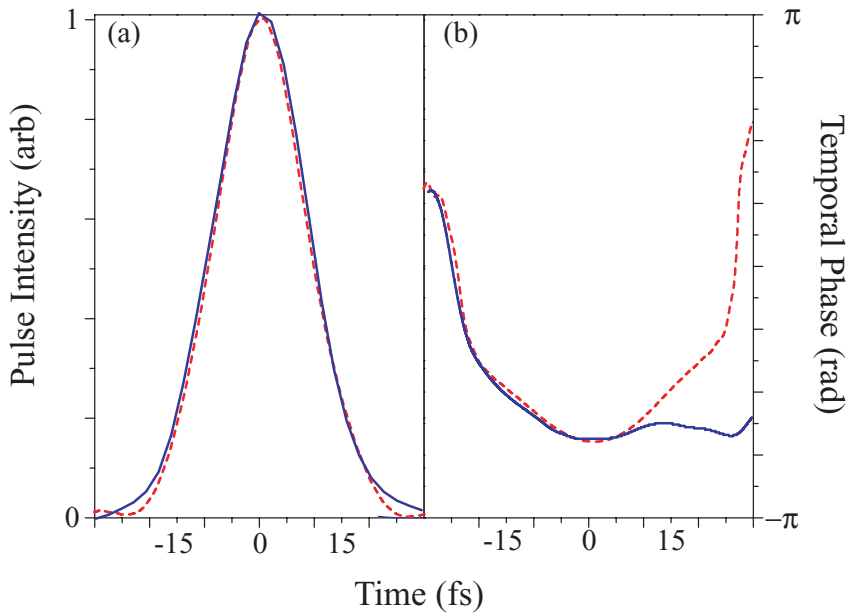

Figure 3.16: Experimental and calculated optimized laser pulse shapes, together with the corresponding temporal phase. The experimental phase trace is the difference between the measured optimized and initial temporal phase in Figure 3.10 scaled by a factor of four in amplitude.

the action with respect to the ionization time τ_b [94, 95]. For the quasi-free electron, the saddle-point condition reduces to an implicit connection between the saddle-point time $\tau_{b,s}$, and the return time τ. In fact, the calculation of the time-dependent dipole moment in Eq. (3.1) can be simplified further by assuming that for each time τ the major contribution corresponds to only those electrons which have been ionized in the interval $(\tau - T, \tau)$, where T is the period of the laser light. By comparing the harmonic spectrum calculated by Eq. (3.1) with a full numerical solution of the Schrodinger equations, we verified that there is good agreement between the semiclassical theory and the fully quantum theory, for laser pulses longer that 10 fs (centered at 800 nm) where nonadiabatic effects can be neglected [16, 96].

In the case of a free electron, simple integration reveals that the action, and hence,

the dipole phase, is proportional to the laser intensity. Near cutoff, harmonics are generated by only a few electron trajectories corresponding to electrons ionized near the peak of the pulse, and therefore the phase of the harmonics is close to quadratic. Past work has demonstrated that this intrinsic phase can be compensated for by a linearly chirped laser pulse, but without any enhancement or selectivity of the harmonics [81, 96, 15]. In contrast, in the mid-plateau region of the harmonic spectrum, more electron trajectories contribute to the emission. Some of these trajectories correspond to ionization times further from the peak of the laser pulse, and therefore a more complex (nonlinear) phase modulation of the harmonic orders appears. Using a laser pulse with an appropriate nonlinear amplitude and phase modulation of the atomic dipole can result in the generation of more temporally coherent x-ray emission.

3.9 Intra-atomic phase matching

To obtain an intuitively clear picture of the optimization process, we calculate the contributions of the individual electron trajectories to a particular harmonic. We Fourier-transform the time-dependent dipole moment given by Eq. (3.1), and then calculate the Fourier integral by using the saddle point technique with respect to the return time τ [97]. The resulting expression for the amplitude of the mth harmonic is the sum of the complex contribution from each trajectory (s) that contributed to the mth harmonic order; omitting some slowly varying terms, we obtain

$$d(\tau) \propto \sum_s \left[\frac{\pi}{\varepsilon + i(\tau_s - \tau_{b,s})}\right]^{\frac{3}{2}} E(\tau_{b,s}) \exp\{[-iS(p_s, \tau_s, \tau_{b,s}) - \omega_m \tau_s - \gamma(\tau_b)]\}, \tag{3.3}$$

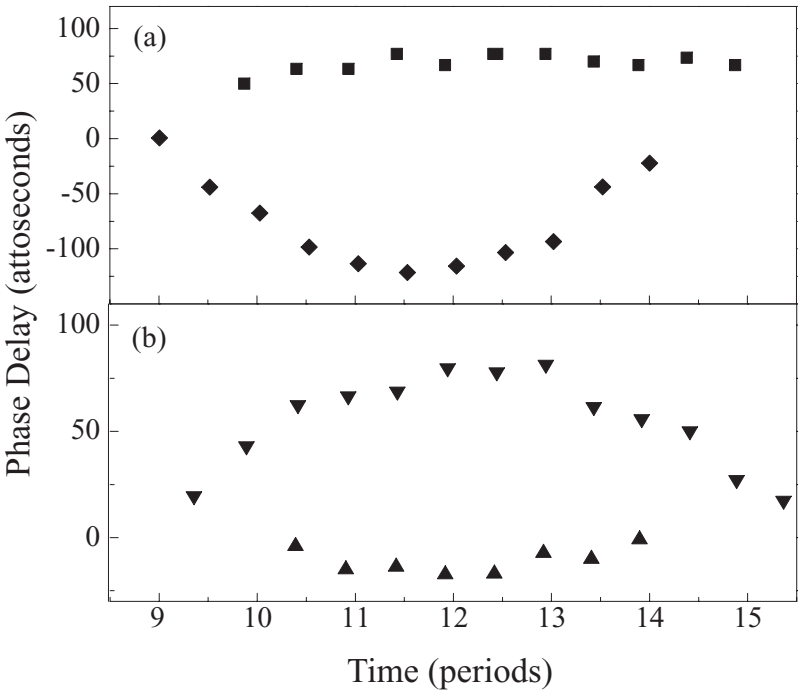

Figure 3.17: (a) Phase distribution of the most relevant trajectories before (diamonds) and after (squares) optimization. (b) Phase distribution of neighboring harmonic orders after optimization.

where τ_s is the saddle-point value of τ, which is determined by the relation

$$\frac{1}{2}[p_s(\tau_s, \tau_{b,s}) + A(\tau_s)]^2 + I_p = \hbar\omega_m.$$

This relation poses an additional restriction on the number of relevant trajectories, by limiting them to only those that contribute to the harmonic of interest. Equation (3.3) is a special representation of the dipole moment, allowing one to calculate directly the amplitude and phase of the contributions of the individual trajectories from each half-cycle. In our simulations, we observe the same degree of enhancement for a given harmonic for a variety of pulse shapes, provided they have the same nonlinear chirp (within ≈ 5 %).

Figure 3.17 illustrates the essence of the optimization process. In Figure 3.17(a), the diamonds show the time dependence of the phase of the 25^{th} harmonic when

generated by a transform limited pulse. This dependence is close to parabolic, which reflects the effect of the laser-induced intrinsic phase of the atomic dipole. In contrast, the phase dependence for the optimized laser pulse (squares) is almost flat, with a phase error corresponding to a time delay of less than 25 attoseconds — which is considerably smaller than the period of the 25^{th} harmonic (106 attoseconds). This effect can be interpreted as a phase matching that takes place between the atom and the laser pulse, ensuring that the phases of the contributions from different electron trajectories are locked within a narrow time interval. This leads to a strong positive interference effect in the frequency domain, optimizing the temporal coherence of the harmonic field. Figure 3.17(b) shows the temporal phase of the trajectories that contribute to the 23^{d} and 27^{th} harmonic orders for the identical laser pulse shape which optimizes the 25^{th} harmonic (Figure 3.16). It can be seen that the optimal pulse shape for the 25^{th} harmonic "over-compensates" the phase for lower-order harmonics and "under-compensates" the phase for higher order harmonics.

The degree of selectivity possible in controlling the relative intensity of harmonics of the HHG spectrum is determined by the degree to which the electron trajectories that generate each harmonic order are independent. More precisely, it depends on how independent the regions over which the electron wave packet phase is accumulated for a trajectory that contributes to one harmonic order vs. another. We see from section 3.4 that there is significant overlap between the trajectory times of neighboring harmonic orders. It is clear that some independence exists, allowing for energy to be channeled among harmonic orders and leading to selective control of the

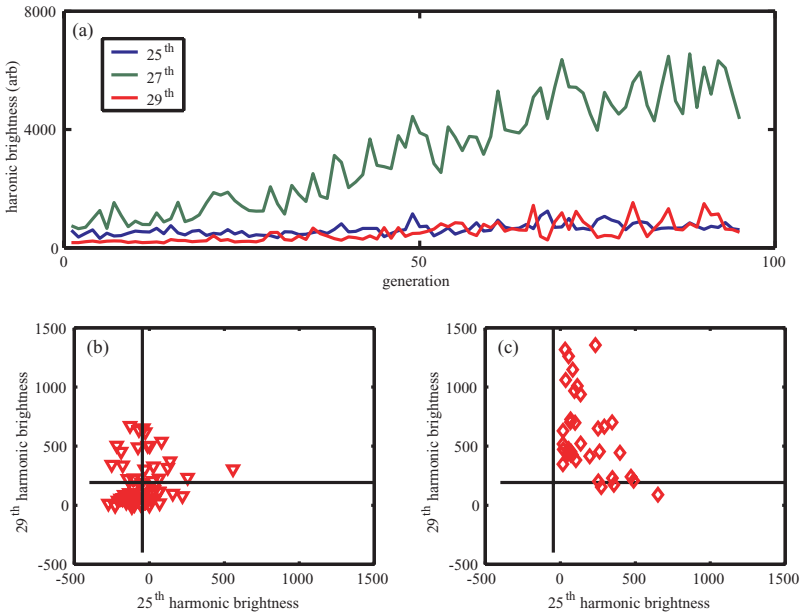

Figure 3.18: The anti-correlation of the intensity of neighboring harmonic orders of nearly optimal driving pulses illustrates the degree to which selective control is possible in HHG. The harmonic peak intensities from Figure 3.9 are plotted for the 25^{th}, 27^{th}, and 29^{th} harmonic orders (a). The correlation between those intensities is shown for early (b) and later (c) generations.

HHG spectrum. However, because most of the trajectories experience an overlap, we also expect correlated behavior between harmonic orders for pulse shapes that are very near optimal. As the algorithm tries different pulse shapes to learn to best control the system, many nearly optimal pulse shapes are tried. A pulse shape that provides a flat phase for the trajectories for the target harmonic will introduce some curvature into the neighboring harmonic orders. We see from Figure 3.17(b) that the phase distribution of the neighboring harmonic orders has opposite curvature. Thus if a nearly optimal pulse shape "flattens" the phase distribution for one harmonic order, then the other neighbor will have a more-curved trajectory phase distribution. This should be reflected in an anti-correlation of the intensity of the neighboring harmonic orders during the optimization. Figure 3.18(a) shows the intensity of the 25^{th}, 27^{th}, and 29^{th} harmonic orders for the best result for each generation from the data in Figure 3.9. Pulse shapes at the beginning of the optimization run show no specific correlation pattern as illustrated in Figure 3.18(b), however, near convergence of the algorithm, a distinct anticorrelation appears in the data as depicted in Figure 3.18(c).

The results obtained from the rigorous semi-classical approach described above have been independently verified by Chu [98] using a full three-dimensional quantum mechanical treatment using a learning algorithm. Their results find very similar solutions to those found in our experimental and theoretical work. However, the success of the semiclassical approach demonstrates that the approximations implicit in the semiclassical model are both necessary and sufficient for the description of the

intra-atomic phase-matching process.

There are two scenarios that could lead to enhancement in the x-ray emission from the HHG process. The first is the intra-atomic phase matching idea discussed above. Another possible approach is to enhance the dipole at the optimized harmonic frequency at some time in the pulse. One mechanism for enhancement of the dipole response is through the creation of a wavefunction that optimizes the recollision cross section for electron wave packets with a desired kinetic energy. This is a more standard picture of coherent control in which an overall atomic wavefunction is sculpted by electron wave packet interferences to produce an optimal result. This optimization mechanism will result in an increase in the dipole strength for the target harmonic after a few half-cycles of the laser pulse. Thus, the intra-atomic phase matching mechanism is easily distinguished from the dipole-enhancement by looking at the dipole strength of the harmonic on each half-cycle of the laser pulse.

Figure 3.19, shows the strength of the dipole emission at the optimal harmonic from different half-cycles of the laser pulse. This figure clearly shows that the dipole emission strength follows the field and is not increased at later times for the optimal field, as would be expected if the dipole emission were strengthened due to constructive interference of the overall wavefunction of the atom. In the calculation, the x-ray wavelets from each half-cycle are made to interfere implicitly when the dipole acceleration is Fourier transformed to obtain the HHG power spectrum. There is no interaction of the x-ray radiation with the driving laser field or the atom emitting the x-ray radiation. The results clearly demonstrate that both the selectivity and

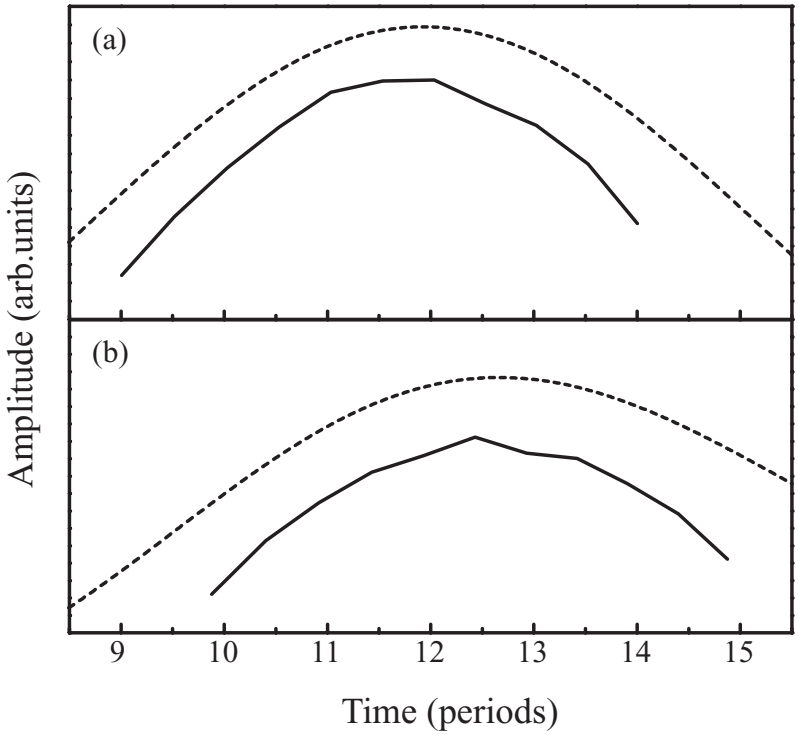

Figure 3.19: Time dependence amplitude of dipole strength of the most relevant trajectories that contribute to the target harmonic (solid line) and the envelopes of the corresponding laser pulse (dashed line) before optimization (a), and after optimization (b).

the increased conversion efficiency are solely due to the interaction of the driving laser field and a single atom due to intra-atomic phase matching.

This model clearly illustrates the physics behind the shaped-pulse optimization and demonstrates that the optimization results from a single-atom effect. It confirms that the total x-ray signal is the result of coherent interference of the emissions resulting from a number of electron trajectories that emit the correct photon energy on recollision, as illustrated schematically in Figure 3.20. In the medium, the laser pulse propagate through each essentially stationary atom. Alternatively, in the reference frame of the pulse, we can view this as atoms traveling through stationary laser pulses. In this picture, each time the atom passes through a half-cycle of the

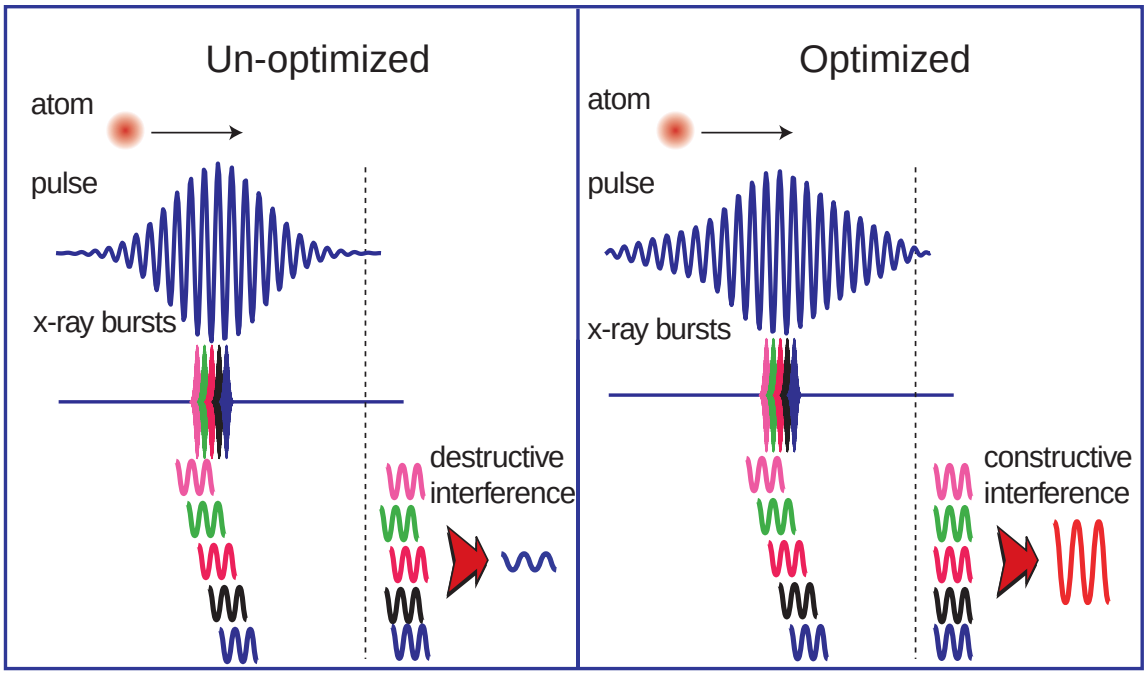

Figure 3.20: Schematic representation of intra-atomic phase matching.

laser pulse, an x-ray burst is generated. If we filter out the target harmonic, we can view this as a series of short, narrow-bandwidth x-ray bursts (or wavelets). For a transform limited pulse the phases of these wavelets are misaligned, and the resulting destructive interference results in a weak harmonic signal. The optimization process shifts the phases of the x-ray wavelets so that they are aligned, resulting in an increase in the brightness of the harmonic. The changes to the driving laser pulse aligns the x-ray wavelets with a 25 attosecond precision.

Manipulating the phase of the x-ray bursts such that they add together constructively generates a larger x-ray flux due to *a reduction of destructive interference pathways*. This is exactly analogous to traditional phase matching. The observed increase in total x-ray flux as a result of re-phasing of harmonic emission therefore represents a new type of intra-atomic phase matching during the laser-atom interaction,

and that manipulates the time-evolution of quantum system on a sub-optical-cycle or attosecond timescale.

3.10 Attosecond science

The demonstration of the control of a process on an attosecond timescale represents the emergence of a new paradigm in the manipulation of matter. In this work, we have demonstrated that it is possible to control a process with attosecond precision using a properly tailored laser pulse whose duration is substantially longer than a femtosecond. In fact, an optical cycle of the central wavelength ($\sim$2.4 fs) is two orders of magnitude longer than the timescale of the control demonstrated here ($\sim$25 as). The reason that control of the electronic wave packet is possible is that it responds to the field, and its trajectory is determined by the integral of the driving field during its excursion in the free-electron continuum. As illustrated in Figure 3.3, the electron trajectories last a fraction of an optical cycle. The control of the electron wave packet required for intra-atomic phase matching is achieved by adjusting the local trajectory, which modifies the electron wave packet phase. The relative change between electron wave packets from different half-cycles aligns the phases using slight adjustments in the amplitude and phase of the driving laser pulse. Furthermore, the carrier-phase offset need not be stabilized because the control occurs during the interaction of a single laser pulse and atom. In our experiment, we are making use of the difference in the evolution of the systems from one half-cycle to another. In essence, we take a "snapshot" of the system (on each half-cycle) and superimpose the "photos." Because the picture changes on each half-cycle, we

are sensitive to dynamic changes. However, because we are superimposing a small number of pictures (~ 10), we can still observe the dynamics. This experiment goes a step further than simply observing the sub-cycle by sub-cycle dynamics; here we control the "pictures" on each half-cycle to make the each picture one each half-cycle the same.

Any process that responds to a fraction of a cycle of the field of an optical pulse can be manipulated on a sub-cycle, and therefore, attosecond (at 800 nm) timescale. A recent experiment at the NRC in Ottawa has demonstrated that excited-state wave packets in H_2 can be manipulated in a similar manner shown in our work [99].

3.11 Summary

In summary, this chapter demonstrates adaptive or "learning" control of a very high order nonlinear process in the strong-field regime for the first time. We demonstrate significantly increased enhancement and selectivity of individual harmonic orders, as well as the generation of near-transform-limited x-ray pulses. Both theory and experiment confirm that we achieve optimization and control of the HHG process by adjusting the relative timing of the crests of the optical wave on a sub-cycle or attosecond timescale. This adjustment changes the recollision-time of an electron with an ion with a precision of ≈ 25 attoseconds. Furthermore, we have shown that this optimization process has uncovered a new type of intra-atomic phase matching. For an optimized laser pulse shape, strong constructive interference can be obtained in the frequency domain between different electron trajectories generated from different half-cycles of a laser pulse, thereby optimizing a particular high-harmonic order.

Microscopically, the optimized laser pulse shaped is mapped onto oscillations in the wave function of the ionizing electron, thus generating an optimized atomic dipole moment for x-ray generation.

This novel type of phase matching occurs within a single atom, and is very distinct from conventional phase matching. In conventional phase matching, the velocities of the fundamental and harmonic waves are "matched" throughout an extended interaction medium, thereby increasing the harmonic output [90]. In contrast, here a single-atom interacts with an optimized optical waveform. This process also has an analog in mode locked lasers, except that in this case the constructive interferences occur in time instead of in frequency. We note that the total integrated x-ray flux, both experimentally and theoretically, increases as a result of optimization. Therefore, more laser energy is converted into forward-directed x-rays as a result of the intra-atom phase matching process. Finally, this selective optimization could not be achieved using a flattop, fast rise time, pulse. Even if such a pulse could be generated experimentally (which is not possible at present because significantly more bandwidth would be needed), it would likely enhance all harmonics, without any selectivity. Using optimally shaped pulses, we achieve a higher degree of control by combining the non-linear chirp of a laser pulse with the nonlinear phase of the HHG. The physical reason for our ability to control HHG is that the harmonic emission is due to a high-order electronic nonlinearity with a finite response time. This work is the first to take advantage of this non-instantaneous response to enhance a nonlinearity.

Our results have immediate utility for the probing of dynamics of chemical and material systems, because it provides a way to select a harmonic without temporally broadening it. The result is a bright, quasi-monochromatic, transform-limited, and highly spatially-coherent soft x-ray light source for use in techniques such as photoelectron spectroscopy and spectromicroscopy, time-resolved x-ray studies of material and chemical systems, and time-resolved holographic imaging. Finally, HHG has proven to be a fruitful test-bed for further work in quantum control concepts, because theoretical models are available to aid in understanding the outcome of optimization. For example, the speed and robustness of different algorithms can be evaluated, to learn more about multi-parameter optimization. Finally, we note that the application of an evolutionary learning algorithm resulted in our obtaining a deeper understanding of the dynamics of this quantum system; i.e. *"learning" algorithms really do result in learning.*

CHAPTER IV

Coherent Control of Molecules: Manipulating Molecular Degrees of Freedom

4.1 Introduction

Controlling atoms and molecules with coherent optical fields has been a long-standing goal in chemical physics [1, 2]. With the advent of ultrafast lasers capable of generating pulses that are short in comparison to molecular timescales, there has been considerable interest in creating, controlling, and measuring vibrational wave packets. There has been increasing interest in not only achieving control in quantum systems, but also in understanding the control mechanism, which has proven to be a challenging task.

Early experiments generated wave packets in excited electronic states and demonstrated control over the position of these wave packets as function of time [54]. Recent experiments [100] have included nuclear motion in the ground electronic state, which is directly relevant to controlling and monitoring many chemical reactions. These experiments focused on controlling motion in a single normal mode of the system. Extending control and measurement of vibrational motion to several modes, including

overtones, is an exciting prospect for several types of studies, including mode coupling and bond selective chemistry [101, 19]. Furthermore, most past work on ground state vibrations relied on transferring population through an excited electronic state (resonant Raman). These resonant Raman techniques are disadvantageous in that they require lasers to be tuned to an excited electronic state, and that limits the number of systems that may be studied. Moreover, most past work has been done at low pressures with atomic and molecular beams that are not conducive to generating a high yield in a bimolecular chemical reaction.

In this Chapter, I demonstrate a number of experimental advances in coherent control of molecular systems. First, we demonstrate *selective* control over molecular motion in gases *at STP* using very short, shaped, excitation pulses. Coherent vibrational excitation of a *single* bond corresponding to thermal temperatures over 2000 K was shown to be possible. This is an important milestone towards the goal of laser selective chemistry [19] on a macroscopic scale, because it extends cryogenic and molecular beam experiments to high temperatures and densities. Secondly, I demonstrate the creation and measurement of shaped multimode vibrational wave packets in CCl_4 with strong overtone excitation, implying significant vibrational amplitude. We also control which modes and which mode combinations are excited. This implies that we are exciting vibrational coherences, where the displacement of the atoms from their equilibrium position is substantially larger than in previous work [4]. A learning algorithm was used to automate the control process. Using a special cost function [102] incorporated into an evolutionary learning algorithm [103], we obtain a

clear interpretation of the control mechanism, which is based on impulsive stimulated Raman scattering [104, 4]. This serves as a demonstration of a general technique for systematically gaining insight from solutions found by learning algorithms. Fourth, I demonstrate the use of chirped Raman excitation where the delay between two chirped pulses can be used to control the excitation of a single, specific vibrational mode. Fifth, by analyzing the spectroscopic data obtained from this technique, a wealth of information about anharmonicities and ro-vibrational coupling is obtained. Sixth, I observe and control reaction rates of uni and bi-molecular reactions. Finally, the reshaping of pump pulses in the Raman active medium is shown to seed the excitation of very short vibrational motion, when used in cooperation with spectral broadening induced by self phase modulation.

It is important to note that the vibrational wave packets in this work are excited with a single pulse far detuned from electronic resonances, achieving non-resonant control of the amplitude of modes in the wave packet. This was shown in earlier solid state impulsive stimulated Raman scattering (ISRS) experiments [105, 4, 105]; however, in this new work, the samples were used at much easier to obtain conditions (i.e., temperatures and pressures), and since the leaning algorithm "found" optimal pulse shapes consistent with ISRS, the interpretation is more convincing. Furthermore, no molecular resonance is exploited in this excitation scheme, and the molecules are not specially prepared, the approach is general and can be applied to a large class of molecules. Because it is non-resonant, it can be generalized to any molecular gas or liquid with Raman-active modes that can be excited impulsively,

and it is not limited by the need to access resonances in the VUV. This approach works at high pressures and temperatures, and thus may facilitate laser control of chemical reactions with macroscopic product yields. In particular, since changes in chemical bonding will involve a superposition of several modes, control of multimode wave packets may lead to selective control over reactions.

4.2 Impulsive Stimulated Raman Scattering

The two most important timescales for controlling molecular motion are the vibrational period (τ_ν), and the coherence time (τ_c). If one is able to generate intense, shaped laser pulses whose duration is shorter than τ_ν, then it is possible to manipulate the motion of the molecule on its own natural timescale. This regime is known as impulsive Raman scattering. Control of molecular motion in the impulsive regime with shaped laser pulses offers many important advantages over steady state or transient scattering, where the laser pulse is longer than τ_c and τ_ν respectively. First, one can create and measure vibrational wave packets sensitive to the motion of individual bonds, rather than just populations of eigenstates. Secondly, since the laser pulse is shorter than τ_c, all of the laser energy deposited into the molecules is done so coherently, allowing for efficient molecular excitation. (e.g., driving of overtones). Finally, one can programmably alter the phase of a single driving pulse, simultaneously controlling the excitation of several vibrational modes in a given molecule. Attempts to control a comparable number of modes in a molecule with transient or steady state Raman scattering would require several tunable, picosecond, phaselocked lasers.

Excitation of Raman-active modes involves two photons with a frequency differ-

ence equal to the vibrational energy. Since the molecule has a significant amount of inertia, it cannot respond instantaneously to the details of the rapidly varying electric field, and the dynamics are insensitive to the absolute temporal phase. What is most relevant for Raman type processes is the phase of frequency differences separated by the Raman frequency in the light field. For a vibrational mode with a frequency of Ω_ν, what matters is the relative phase of frequency pairs whose difference is equal to Ω_ν. In a short pulse with a continuous spectrum, one has to integrate over all frequency pairs separated by Ω_ν. If the duration of a driving laser pulse τ_p is shorter than the vibrational period $\tau_\nu = \dfrac{2\pi}{\Omega_\nu}$, the bandwidth of the laser pulse $\Delta\omega_L$ exceeds the vibrational frequency, and the excitation can be considered impulsive. During impulsive stimulated Raman scattering (ISRS), frequency pairs with a difference of Ω_ν within the bandwidth of a single laser pulse act as pump and Stokes photons. For appropriate phasing of pairs within the bandwidth, strong excitation results. In a simple classical model, the displacement from equilibrium of the nuclear coordinate Q for a given mode ν in the ISRS limit can be described by [104]

$$\frac{\mathrm{d}^2Q}{\mathrm{d}t^2} + 2\gamma\frac{\mathrm{d}Q}{\mathrm{d}t} + \Omega_\nu^2 Q = \frac{1}{2}N\left(\frac{\mathrm{d}\alpha}{\mathrm{d}Q}\right)_0 E_L^2,$$

where γ is the coherence decay rate, Ω_ν is the vibrational frequency, N is the number density of molecules, $\left(\frac{\mathrm{d}\alpha}{\mathrm{d}Q}\right)_0$ is the change in polarizability with intermolecular distance Q, $E_L = \frac{1}{2}\{A(t)\exp(-i\omega_L t) + c.c.\}$ is the laser field, and ω_L is the laser central frequency. Expanding the laser field as

$$E_L^2 = \frac{1}{4}\{2A_L(t)A_L^*(t) + A_L^2(t)e^{-i2\omega_L t} + A_L^{*2}(t)e^{i2\omega_L t}\}$$

gives a "dc" term corresponding to the intensity profile $I(t)$, and two second harmonic

terms. The nuclei, which have too much inertia to respond to the fundamental (or second harmonic) field, are effectively driven by $I(t)$. Thus, the strength of excitation of a vibrational mode with frequency Ω is proportional to the power spectral density $D(\Omega)$ of the intensity profile at that vibrational frequency, where

$$D(\Omega) = \int_{-\infty}^{\infty} \mathrm{d}\omega a_L(\omega) a_L(\Omega - \omega) \exp\{-i[\phi(\omega) - \phi(\Omega - \omega)]\}$$

and

$$A(\omega) = \mathcal{F}\{A(t)\} = a_L(\omega) \exp[-i\phi(\omega)].$$

Based on this simple analysis, a pulse with spectral phase described by a periodic function at the molecular vibrational frequency (e.g., a train of pulses separated by the vibrational period [4, 104]) should be as efficient as a transform-limited pulse in exciting vibrations [4, 104, 57]. Figure 4.1 illustrates this relationship, showing a shaped laser pulse and a modification of the power spectrum, illustrating the control of a given vibrational frequency is accomplished by manipulating the power spectral density of $I(t)$ at the mode frequency. (NOTE: to maximize $D(\Omega)$, $\phi(\omega) - \phi(\Omega - \omega) = const$, which defines a periodic function.) Later in the text, I compare the excitation of Raman modes with intense transform limited pulses to that of low-intensity chirped Raman excitation and observe the breakdown of the weak excitation limit described in this analysis.

4.3 Selective learning control of molecular vibrations

The experiments in this chapter employ intense shaped light pulses with a central frequency of 375 THz (800 nm), generated by an ultrashort Ti:Sapphire amplified

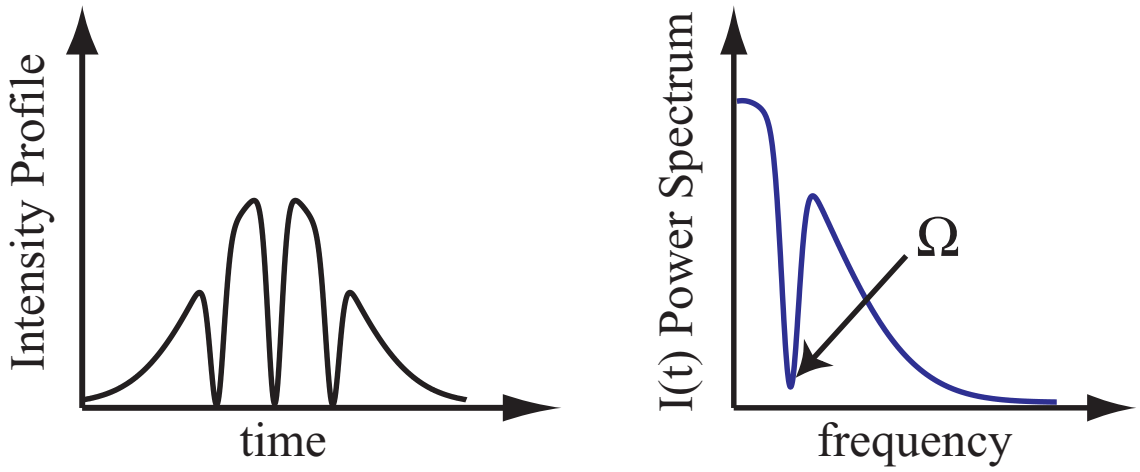

Figure 4.1: ISRS is controlled by manipulating the power spectrum of the intensity profile.

laser system. The laser system generates temporally shaped pulses as short as 15 fs, at a 1 kHz repetition rate, with over 1 mJ of energy [69]. A pulse shaper based on a 19 element deformable mirror is inserted between the oscillator and the amplifier [71]. The enormous spectral bandwidth of the pulses produced by the laser system allows for impulsive excitation of room temperature molecules in a relatively pure state, without pre-selecting a given set of molecules. The FWHM bandwidth of the output laser pulses is over 18 THz, allowing for impulsive excitation of the symmetric breathing mode (ν_1) of SF_6. At room temperature (300 K), kT = 6.24 THz, making the thermal population of the first excited level of this mode only 0.024.

The shaped, amplified pulses from the laser were focussed into a 450 μm inner diameter hollow core fiber waveguide, with a length of 30 cm. The waveguide was filled with the molecular gas, with pressures varying from 20 to 1000 torr. The waveguide could either be filled from a pressurized gas bottle, or by simply connecting a liquid cell to the waveguide and working with the vapor pressure of the molecular liquid.

Temporally delayed pulses with a frequency of 750 THz (400 nm), a bandwidth of 1.5 THz, and pulse energy of 1-3 μJ were injected collinear with the driving pulse in order to probe the vibrational excitation created by the driving pulse. The delay, which was several hundred femtoseconds, was longer than the pump pulse duration but shorter than τ_c. The probe pulse spectrum was measured as the shape of the driving pulse was varied. The spectrometer monitoring the probe spectrum was interfaced with a computer, which also controlled the pulse shaper, allowing for closed-loop control of the process. The amplitude and phase of the shaped pulses were measured using second-harmonic frequency resolved optical gating (SHG FROG) [72].

As the probe pulse propagates through the vibrationally excited gas, it encounters a periodically modulated index of refraction and therefore develops sidebands spaced by the vibrational frequency of the excited modes. As the molecules are prepared in a coherent superposition of $\nu = 1$ and $\nu = 0$, the probe pulse undergoes both Stokes and anti-Stokes scattering. There are no sidebands from the probe in the absence of the pump, since the scattering of the probe is a result of a coherence between $\nu = 1$ and $\nu = 0$. The pump pulse also contains signatures of the molecular coherence in the form of a continuous redshift (which is only present for pump pulses that excite vibrations) and a modified temporal profile at higher pressures. This modified temporal structure consisted of a pulse train at the vibrational frequency of the mode being excited and is explored in a later section of this chapter.

In order to discover optimal pulse shapes for driving and suppressing this molecular coherence, we used the evolutionary algorithm discussed in Chapter 2. The

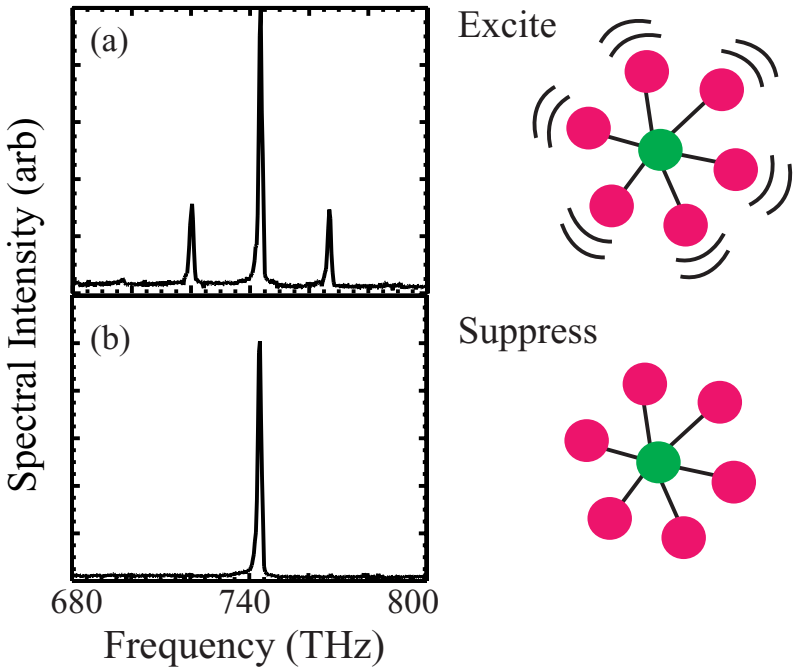

Figure 4.2: Learning control of SF_6 by feeding back the vibrational sideband energy into our learning algorithm.

fitness function used in these experiments is the total amount of energy in the probe sidebands for the mode of interest, which is a quantitative measure of the vibrational coherence. This approach allows for more general shaping of a multimode wave packet because the pulse shaper is programmable and can be guided by the learning algorithm. For example, exciting CCl_4 with a single, short pulse coherently excites all three Raman active vibrational modes (ν_1, ν_2, ν_4) simultaneously. Tailoring the intensity profile allows us to control the excitation of each vibrational mode independently.

Results demonstrating the excitation and suppression of the symmetric breathing mode (ν_1) in SF_6 at 250 torr are shown in Figure 4.2. Curve (a) shows the probe spectrum for a pump pulse optimized for mode excitation, while curve (b) shows the probe spectrum for a pump pulse optimized for mode suppression. Suppression and

enhancement is effective over a broad range of pressures (20-700 torr). We interpret the mechanism in a regime where pulse reshaping during propagation is negligible. The sideband separation of 23.25 THz is in good agreement with the frequency of ν_1 as well as previous measurements [106]. Based on the intensity of the sidebands in the probe spectrum, one can estimate that between 1-10 % of the molecular sample is excited. This result is promising for attempting bimolecular chemistry initiated by tailored laser pulses.

There are two strong Raman active modes in CO_2: the asymmetric CO stretch mode (ν_1), and two quanta of the OCO bend mode (ν_2). The corresponding Raman shifts are 38.6 THz and 41.6 THz respectively. Using the difference in intensity of the sidebands for the two modes as the feedback signal in an evolutionary algorithm, we could make either mode dominant in the excitation. Figure 4.3 shows the probe pulse spectra when the excitation pulse was optimized to drive ν_1 (top panel), or two quanta of ν_2 (bottom panel). This data was taken at a pressure of 280 torr, with similar results obtained at a pressure of 800 torr.

A similar experiment was performed in CCl_4. The evolutionary algorithm was used to direct the pulse shaper to excite a specific mode (ν_1)v while suppressing others, by adjusting the relative spectral phases in the pulse. The black bar in Figure 4.4(a) shows that the relative energy scattered into ν_1 is over ten times larger than for ν_4. The same trend is reflected in the power spectrum of the intensity profile at the vibrational frequencies [Figure 4.4 (b)]. The reverse experiment (optimizing ν_4 vs. ν_1) was also performed

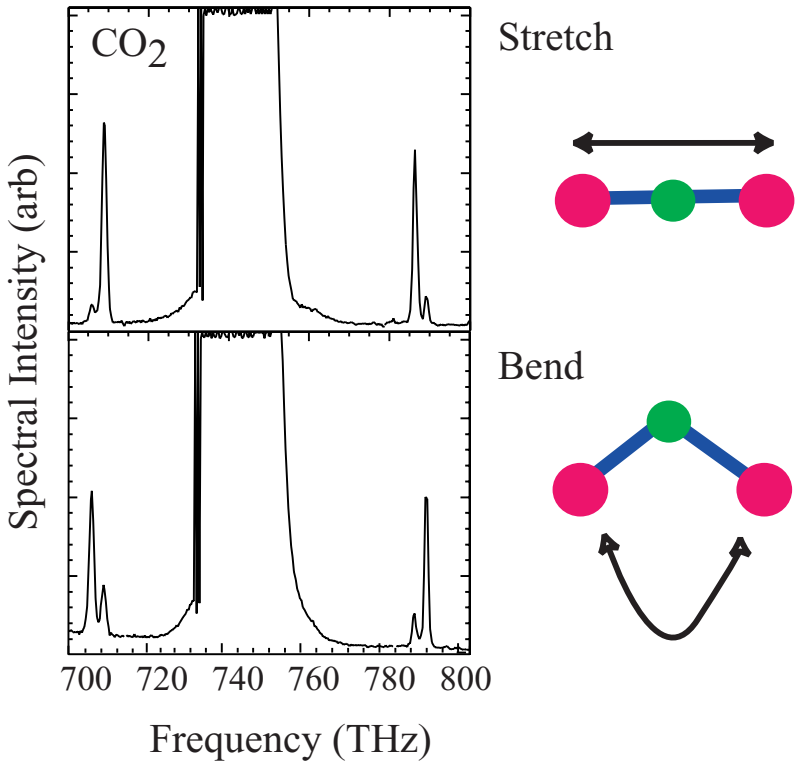

Figure 4.3: Selective learning control of both vibrational modes in CO_2 by feeding back the vibrational sideband energy difference into our learning algorithm.

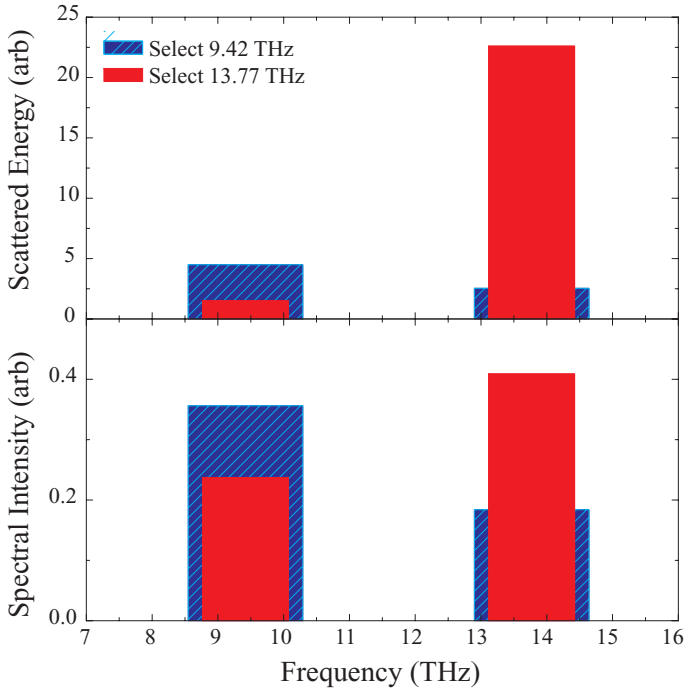

Figure 4.4: Selective learning control of vibrational modes in CCl_4 by feeding back the vibrational sideband energy difference into our learning algorithm.

The degree of control shown here is limited by the resolution of the pulse shaper. Although an algorithm is not in principle required for this technique, it is very convenient because it compensates for any experimental non-idealities and automates the tailoring of populations (mode amplitudes) in the wave packet by selecting which modes participate. In order to verify the interpretation of the results, we monitored the probe spectrum for several different gases (benzene, carbon tetrachloride, nitrogen and ethylene), and also varied the pump pulse duration without altering the bandwidth. Sideband spaced by the Stokes shift for a given mode appeared only when the pump pulse duration was less than the vibrational period.

The results shown above clearly demonstrate that the excitation of vibrational modes with frequencies less than the laser bandwidth is very sensitive to the shape

of the pump pulse. This is in contrast with the steady state and transient regimes of Raman scattering [107]. It is also in contrast to the usual case of impulsive scattering, in which the response is simply proportional to the pulse energy. However, shaping of pulses with enough bandwidth to support impulsive scattering can lead to detailed control over the molecular response [57].

4.3.1 Using modified cost functions to learn control mechanisms

In order to learn as much as possible from the solutions discovered by the algorithm, in some cases we incorporated a special cost function into the algorithm. The cost function imposes a penalty into the fitness for deviations from an unshaped pulse, limiting unnecessary variations in the optimized pulse shapes. This ensures that all of the differences between an optimized pulse and an unshaped pulse are not merely sufficient, but necessary. The control mechanism is therefore much easier to deduce from the solutions. The cost function, f_{cost}, simply multiplied the experimental fitness, and had the form

$$f_{cost} = 1 - \frac{w}{n g_{max}^2} \sum_{i=0}^{n} (g_i - g_{tl})^2.$$

Here, w is a weighting factor that was adjusted until f_{cost} was slightly less than 1, g_{max} is the maximum gene value for a given pulse shape, g_{tl} is the value of each gene for an unshaped pulse, and g_i is the gene value for the i^{th} gene for each pulse shape evaluated. Although the values of g_{tl} were set to those of an unshaped pulse in the present experiment, they can be set to bias the cost function toward any pulse shape. Thus the deviations from any given solution can be penalized, in order to discover the essential components of a solution.

Figure 4.5 shows the intensity envelopes (inset) and their transforms for two pulses optimized to excite a molecular coherence in SF_6, and two pulses optimized for suppression. The algorithm found two separate solutions for enhancing and suppressing the vibrations. Each pair of solutions have very different intensity profiles, but nevertheless have nearly the same values in the power spectrum of $I(t)$ at $\Omega_\nu = 23.25$ THz. The two solutions for optimizing excitation are shown as the green and blue curves in Figure 4.2. The red and black curves represent solutions for suppressing the vibrational coherence, exhibiting local minima at Ω_ν. The green and black curves were taken with the term f_{cost} included in the algorithm, while the red and blue curves were not so constrained. The cost function in our experiment penalized deviations from an unshaped (transform-limited) pulse. The green and black curves show pulses that deviate minimally from an unshaped pulse, while still maintaining control. The differences between the two curves for enhancing the vibrations and the two curves for suppressing the vibrations illustrate the ability of the cost function to help isolate the important features in the optimized pulses — a large or small value in the spectrum of $I(t)$ at 23.25 THz in this case. Comparison of the curves for enhancing and suppressing vibrations supports the impulsive excitation mechanism described above. Analysis of mode selectivity in other molecules (such as CCl_4) illuminates the same underlying physical mechanism as demonstrated here for SF_6: to enhance or suppress excitation of a given mode, the power spectrum of $I(t)$ at the two photon resonant frequency must be made large or small. This control illustrates how a *single broadband laser* can be used to control the excitation of N modes in a

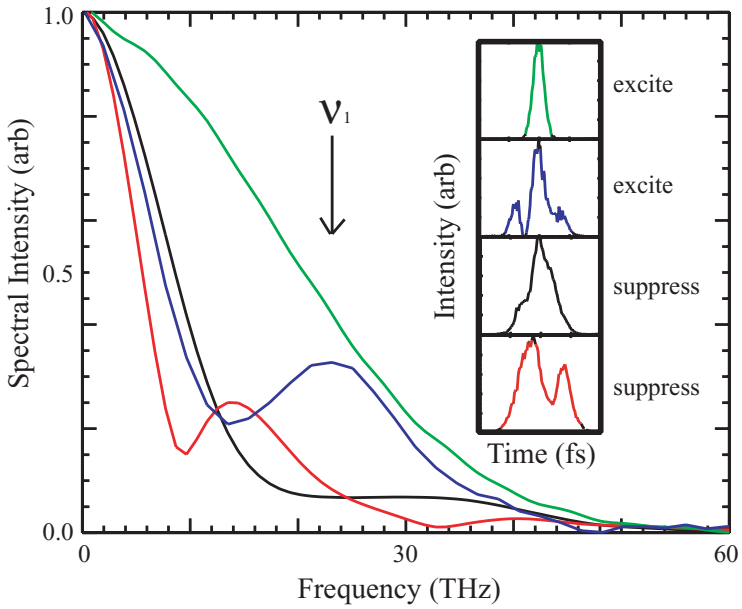

Figure 4.5: The measured power spectrum of the intensity profiles of various shapes that control vibrational excitation in SF_6. Use of the cost function modifications elucidates the control mechanism.

given molecule. This single laser replaces $N+1$ phaselocked narrowband lasers that one would have to tune to the various Raman resonances in order to gain a similar degree of control.

4.4 Chirped ISRS excitation

In order to control the excitation level of a Raman-active vibrational mode in a molecule that can be excited impulsively by our laser systems, we need only to control the power spectral density of the pulse shape at that vibrational frequency. In this section, I describe what we call impulsive Raman excitation. When a linearly chirped laser pulse is injected into a Michelson interferometer, two replica pulses with a controlled relative time delay are produced. A linearly chirped pulse has

an instantaneous frequency that varies linearly with time. When two such pulses are separated by less than their pulse duration, the instantaneous frequency from each chirped pulse beats at the difference frequency between the two pulses, as illustrated in Figure 4.6. Figure 4.6 shows the power spectrum of chirped pulse pair and demonstrates that this apparatus acts as a tunable, single-frequency ISRS excitation source by arranging photon pairs with a frequency difference proportional to the interferometer delay to appear at each point in the pulse pair. In the time domain, the interference produces an intensity modulation at the instantaneous frequency difference $\Delta\nu$.

Chirped Raman excitation is best understood in the frequency domain. A chirped broadband pulse can be thought of as a comb of $\sim 10^9$ phase-locked quasi-cw lasers spread out in time (reducing the peak intensity by spreading energy in time), tuning from red to blue. The second time-delayed pulse causes interference between two spectrally shifted combs, equivalent to detuning a cw laser by an amount proportional to the delay time and the chirp rate.

The instantaneous frequency ($\omega_i = \mathrm{d}\varphi(t)/\mathrm{d}t = \omega_L + 2bt$, where $c_R = b/\pi$ is the chirp rate as defined by $\varphi(t) = \omega_L t + bt^2$) of the pulse sweeps linearly in time, producing a constant frequency difference ($\Delta\nu$) between the two pulses from the interferometer for non-zero delays (τ). The interference between the two pulses produces a beat note with a period of $1/\Delta\nu$ in the intensity profile described by

$$I(t) = I_{in}(t) + I_{in}(t-\tau) + 2\sqrt{I_{in}(t)I_{in}(t-\tau)}\cos(\omega_L\tau + b\tau^2 - 2b\tau),$$

where $I(t)$ is the intensity profile, τ is the delay between the pulses, and $\Delta\nu = c_R\tau$.

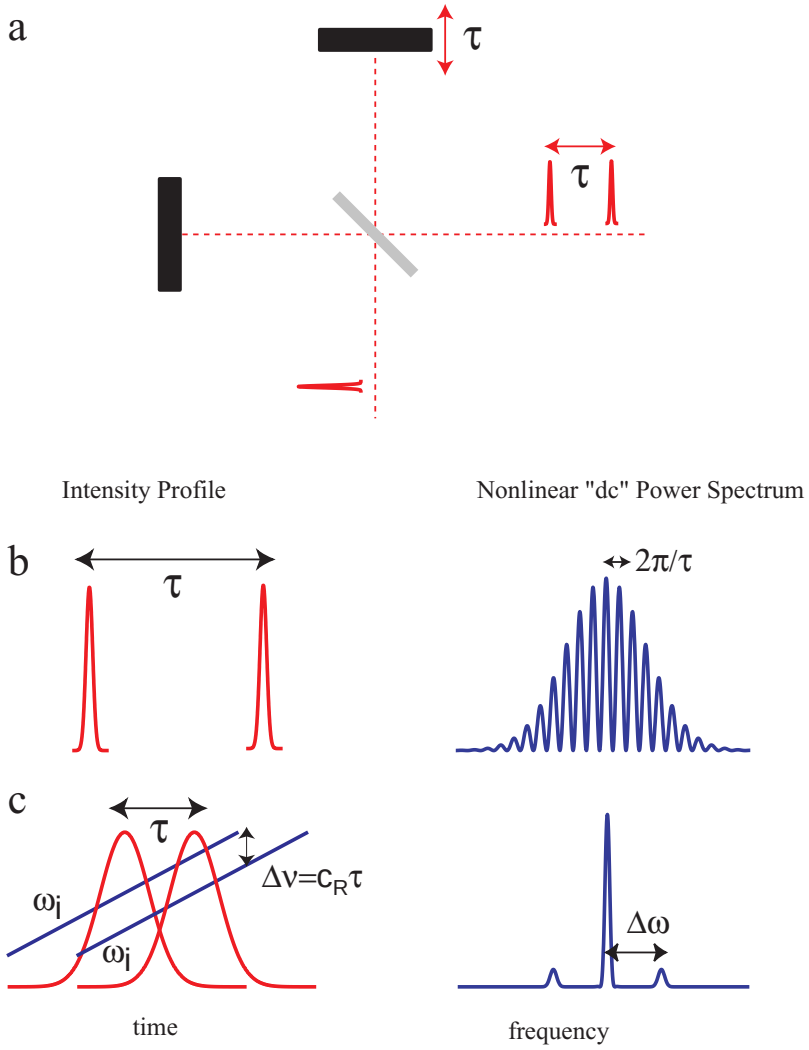

Figure 4.6: Michelson apparatus used for both transform-limited pulse-pair ISRS excitation and chirped Raman excitation (a). Time and $I(t)$ power specra of transform-limited pulse pair excitation (b), and chirped Raman excitation (c).

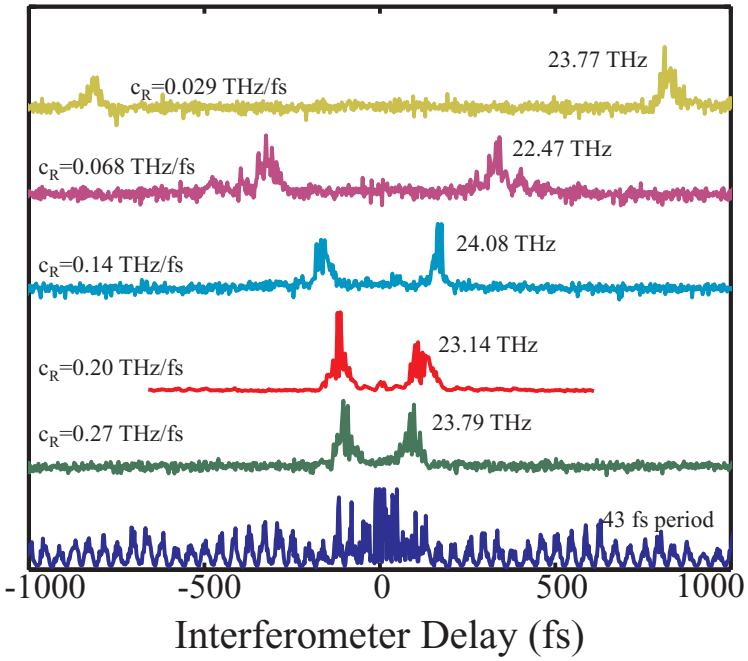

Figure 4.7: Impulsive chirped Raman excitation of SF_6 for many chirp rates.

Changing the delay tunes the frequency difference and the period of the intensity modulations, allowing for mode selective excitation of the molecule.

I first demonstrate impulsive Raman excitation of the 23.25 THz mode in SF_6. The probe pulse spectrum is measured as a function of the Michelson interferometer delay. At a time delay proportional to the chirp rate of the pulse, the molecule is excited, and vibrational sidebands appear. The chirp rate is adjusted by adjusting the grating separation in the compressor and measured using SHG FROG. Figure 4.7 shows a lineout at the Stokes sideband as a function of Michelson delay for a series, each with a different chirp rate. For each pulse, a unique time delay (and its negative delay) excites the 23.25 THz mode in SF_6 and exhibits no vibrational excitation at any other time delay.

Figure 4.8 shows the results of selective excitation of vibrational modes in CCl_4

using impulsive chirped Raman excitation. For this experiment, the pulse was first chirped in time (to $\sim$ 83 fs, with a chirp rate of 0.1125 THz/fs) prior to entering the Michelson interferometer. The chirped pulses were injected into the hollow-core fiber filled with a room-temperature vapor pressure ($\sim$ 80 torr) of CCl_4. The three Raman modes under control are ν_1, ν_2, ν_4, whose frequencies are 13.77 (459 cm^{-1}), 6.54 (218 cm^{-1}), and 9.42 (314 cm^{-1}) THz, respectively. Figure 4.8(a) shows the probe spectrum as a function of interferometer delay. As the frequency difference in the pump matches the vibrational frequency of each mode in the molecule, that mode is driven efficiently while the other modes remain relatively unaffected.

Figure 4.8(b) shows lineouts of the scattered probe intensity at frequencies corresponding to each of the fundamental modes. For a fixed chirp rate (pulse length), the optimal delay for mode ν_1 is given by $\tau_1 = \Omega_1/c_R$. The optimal time delays for modes ν_1, ν_4, ν_2 appear at 122, 88, and 58 fs, implying frequencies of 13.6, 9.9, and 6.5 THz, respectively. The data shows that vibrational modes within the laser bandwidth can be separately controlled with a properly constructed $I(t)$.

4.5 Monitoring Ro-vibrational wave packets through phase modulation

If one is interested in monitoring the evolution of a vibrational wave packet, then a technique for strobing the dynamics is required. This can be accomplished with a second probe laser pulse, which makes a measure of the vibrational wavefunction as a function of delay from the pump pulse. If the pump and probe pulses are both non-resonant and the measurement is purely optical, then the technique is fairly simple to

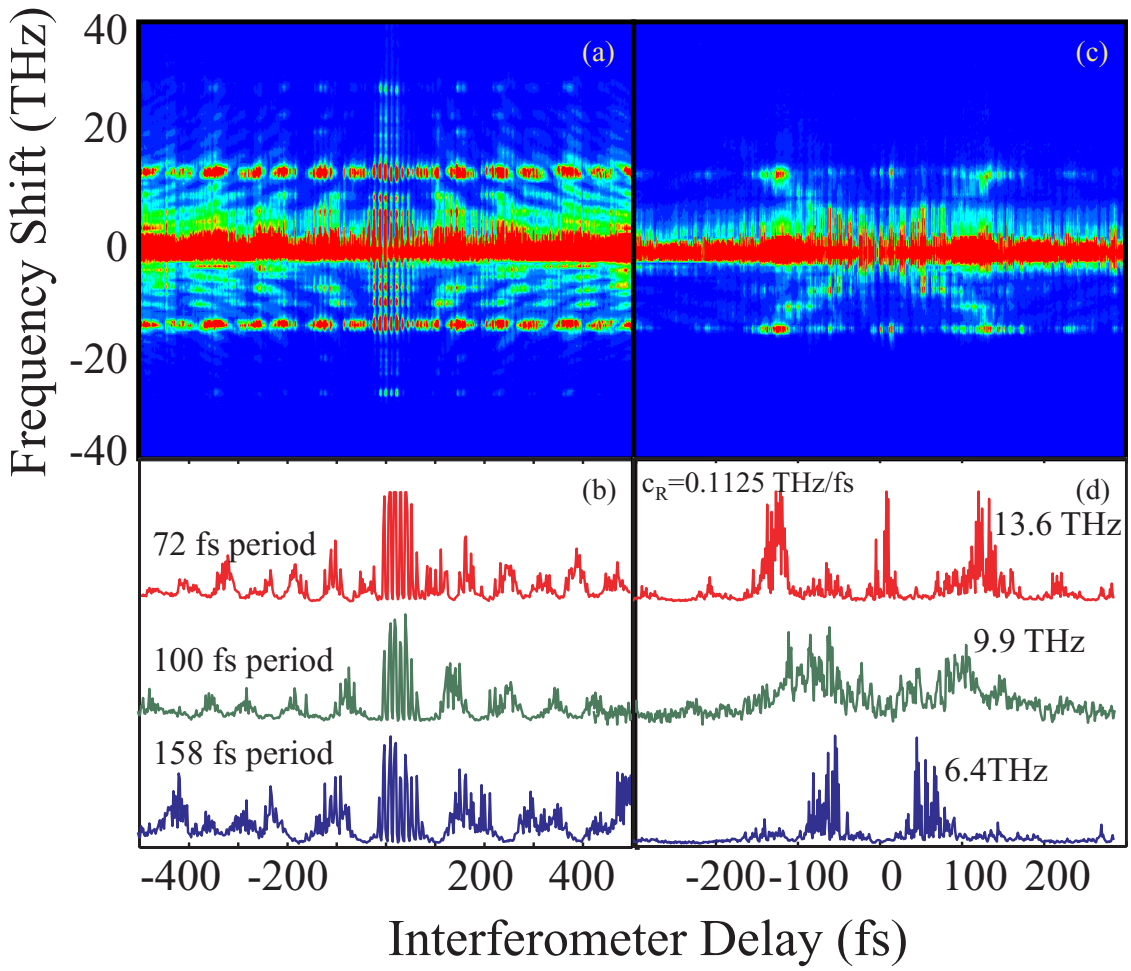

Figure 4.8: Probe spectrum of CCl_4 when excited by two chirped pulses. The shading in the figure is proportional to the scattered light intensity. The chirped pulse is still sufficiently short to drive some impulsive Raman excitation near time zero. (a) Probe spectrum vs. time delay between pump pulses. (b) Lineouts at vibrational frequencies ν_1, ν_4, ν_2. (c) Probe spectrum vs. time delay between two transform-limited pulses pump pulses. (d) Lineouts at frequencies corresponding to $\nu_1, \nu_4, \nu_1 - \nu_4$.

implement and can be used for a large class of molecules. In this section, we describe the creation and measurement of single and multi-mode vibrational wave packets in SF_6, CO_2, and CCl_4. In CCl_4 we also observe dissociation and the creation of vibrational wave packets in Cl_2.

The experimental measurement described above records the spectrum of the probe pulse after traveling through a vibrationally excited gas sample. The vibrational coherence exhibits a time-varying polarizability that modifies the power spectrum of the probe pulse. To modify the probe spectrum in such a manner requires either a nonlinear, or time-varying index of refraction, or in a scattering theory perspective, the probe pulse must undergo an inelastic scattering process with the gas molecules.

The probe pulse intensity is kept low to suppress a nonlinear response from the molecules; therefore restricting the interaction to a linear, time dependent index of refraction, $n(t)$. For a time dependent index of refraction, the power spectrum, $S_0(\omega)$, of a electric field pulse with a Gaussian temporal profile is modified according to

$$S(\omega) = \left| F\left\{E_0 A(t) e^{i[k_0 n(t) l - \omega_0 t]}\right\}\right|^2 = \left| S_0(\omega) \otimes F\left\{e^{i[k_0 n(t) l]}\right\}\right|^2, \tag{4.1}$$

where $A(t) = \exp\left[\dfrac{(t-\tau)^2}{\sigma^2}\right]$, l is the length of the sample, E_0 is the magnitude of the probe field, k_0 is the vacuum wavevector for the field, τ is the time delay between pump and probe, σ is the probe pulse duration, ω_0 is the central laser frequency, and the $\otimes$ denotes a convolution operation. The symbol F denotes a Fourier transform. The index of refraction, $n(t)$, is related to the molecular polarizability, α, (neglecting

orientational contributions of the molecules) through the expression

$$n = \sqrt{\frac{2\alpha + \frac{3\varepsilon_0}{N}}{\frac{3\varepsilon_0}{N} - \alpha}},$$

where N is the number of molecules per unit volume and ε_0 is the permittivity of free space.

When a linearly polarized pulse interacts with a molecule that has an anisotropy in its polarizability, that molecule experiences a torque as it tries to align itself to the direction of the linearly polarized field, see Figure 4.9, and a short time duration pulse exerts an impulsive torque that excites a large number of rotational states and forms a quantum mechanical rotational wave packet. The anisotropy of the molecular potential leads to dephasing and rephrasing of the rotational states, resulting in periodic revivals of the rotational states. The details of these rotational wave packet dynamics are discussed in chapter 5.

Figure 4.10 displays the measured probe spectrum as the pump and probe delay are varied and shows evidence of both rotational and vibrational motion. The vibrational sidebands appear on either side of the probe and are seen to decay, as well as exhibiting revivals associated with the vibrational anharmonicity (due to the dissociative potential of molecules, the spacing of vibrational levels is not harmonic. The deviation from the hamonicity is called the anharmonicity). The rotations have a time-scale longer than the length of the probe pulse, so instead of scattering energy to sidebands, the rotational wave packet modifies the spectrum of the probe pulse. The rephasing of the wave packet occurs periodically and results in a broadening of the probe spectrum and the revival time is dependent on the moment of inertia of

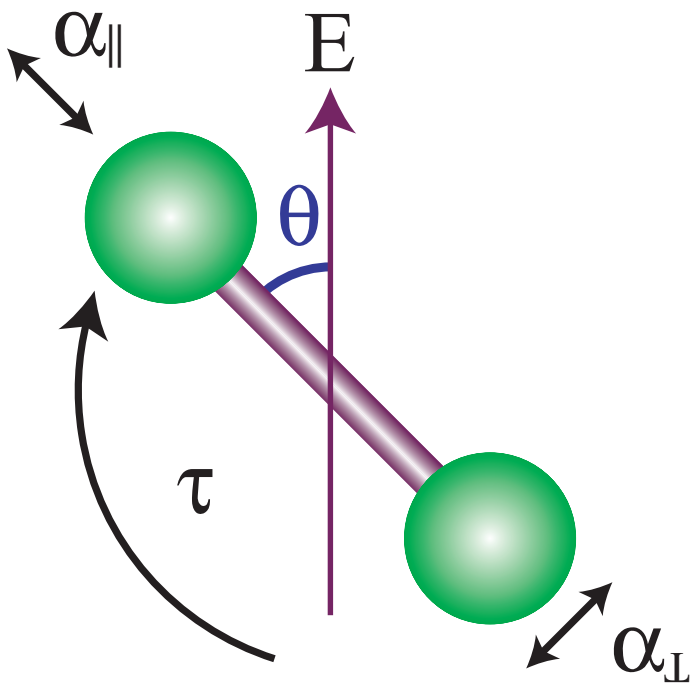

Figure 4.9: Molecules with a non-uniform polarizability experience a torque the attempts to align the molecule to the direction of polarization.

the molecule.

A molecule can be loosely regarded as a collection of balls coupled by springs, with a stiffness given by the bond strength. When the molecule rotates about its center of mass, the molecules are pulled away from the center of mass and this results in a stiffening (increase) of the spring constant. The resonant frequency of a mass-spring oscillator is proportional to the square root of the spring stiffness, so we conclude the faster the molecule rotates, the larger the vibrational frequency will become. This leads to a coupling between rotations and vibrations. Furthermore, the rotational states of a molecule are determined by the moment of inertia of that molecule. When the molecule is excited into a vibrational mode, the inter-atomic separation increases with vibrational excitation. This results in an increase in the moment of inertia of

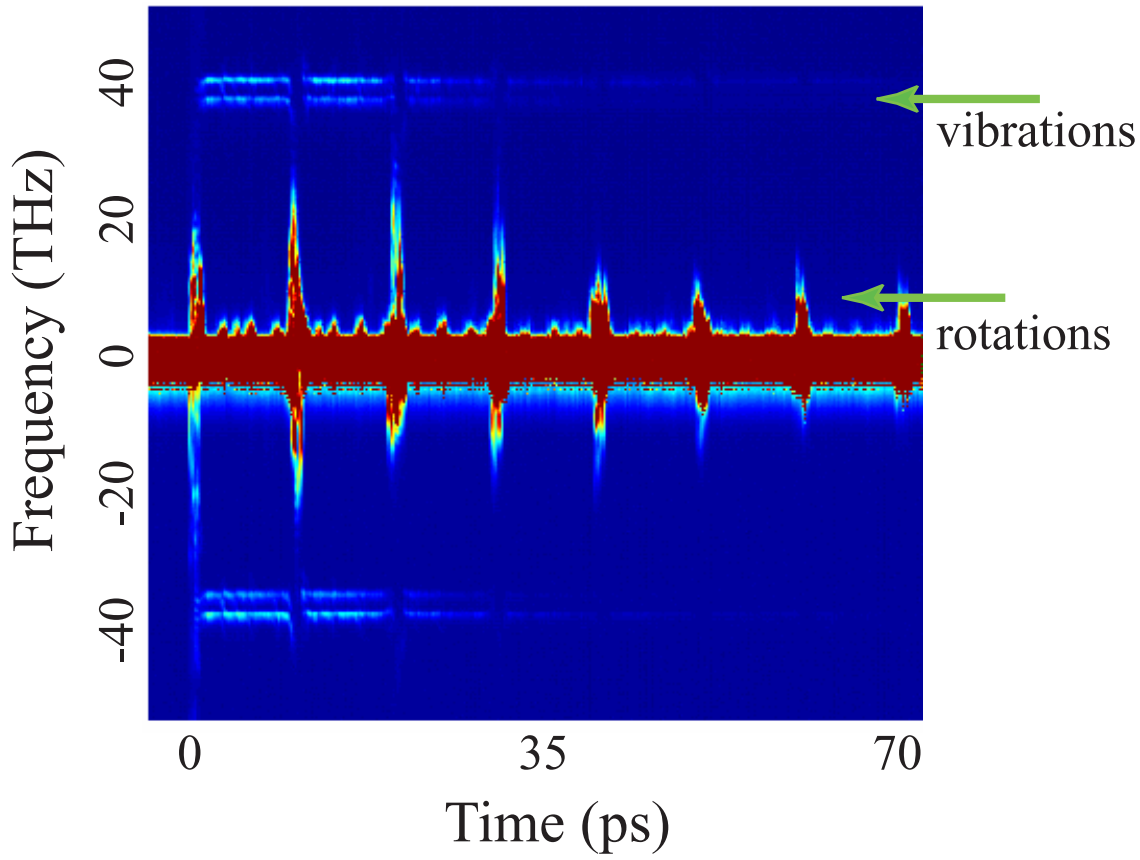

Figure 4.10: The measured probe spectrum as the delay between the pump and probe is varied leads to the observation of ro-vibrational wave packets in CO_2.

the molecule, and modifies the rotational level structure. Therefore, both rotations and vibrations are coupled, and we will see that this has a pronounced effect on our observed signal.

4.5.1 Observing molecular wave packet dynamics with polarizability

In order to understand the relationship between the probe pulse spectrum and the vibrational coherences excited by the pump, we need to calculate the quantum mechanical expectation value of the polarizability operator for each molecule in the ensemble. This will highlight which aspects of the molecular motion are being measured by the power spectrum of the probe pulse. We start by expanding the total molecular vibrational wavefunction in terms of the normal mode basis

$$\Psi_{total}(t) = \varphi_{gs} + \prod_{n}\sum_{i} a_{ni}\varphi_{ni}(q_n)\exp\left(-i2\pi\frac{E_{ni}t}{h}\right) + \chi\left(\sum\varphi_{1i}(q_1), \sum\varphi_{2i}(q_2), \cdots\right), \tag{4.2}$$

where the ground-state has been written as

$$\varphi_{gs} = \prod_{n} a_{n0}\varphi_{n0}(q_n)\exp\left(-i2\pi\frac{E_{n0}t}{h}\right)$$

and the φ_{ni} is the i^{th} vibrational eigenstate ($i = 1, 2, 3, \cdots$) of the n^{th} normal mode, q_n is the n^{th} normal mode coordinate, and a_{ni} is the complex coefficient corresponding to the projection of the total wavefunction onto the normal mode basis. Note that in general, a set of coupled *harmonic* oscillators can be diagonalized such that an orthogonal basis set can be written in terms of normal internal coordinates of the system. However, since a molecule is dissociative, its potential is, by definition, anharmonic. The anharmonicity leads to a non-orthogonality between the so-called

normal modes. The last term (χ) in Eq. (4.2) represents the non-separable portion of the molecular wavefunction that has to do with the overlap between the modes. The internal motion of the molecule is well approximated by the normal motion for low levels of molecular excitation.

In order to calculate the time dependent expectation value of the polarizability, we form a Taylor expansion (limited to second order) in terms of the vibrational coordinates for the two normal modes,

$$\alpha(q_1, q_2) = \alpha_0 + \frac{\partial \alpha}{\partial q_1} q_1 + \frac{\partial \alpha}{\partial q_2} q_2 + \frac{\partial^2 \alpha}{\partial q_1 \partial q_2} q_1 q_2 + \frac{1}{2} \frac{\partial^2 \alpha}{\partial q_1^2} q_1^2 + \frac{1}{2} \frac{\partial^2 \alpha}{\partial q_2^2} q_2^2 + \ldots$$

When we evaluate the expectation value of the polarizability, $\langle \alpha(t) \rangle$, in terms of the wave function, we arrive at the expression

$$\langle \alpha(t) \rangle \cong \alpha_0 \langle \Psi | \Psi \rangle + \frac{\partial \alpha}{\partial q_1} \langle q_1(t) \rangle + \frac{\partial \alpha}{\partial q_2} \langle q_2(t) \rangle + \frac{\partial^2 \alpha}{\partial q_1 \partial q_2} \langle q_1(t) q_2(t) \rangle$$
$$+ \frac{1}{2} \frac{\partial^2 \alpha}{\partial q_1^2} \langle q_1^2(t) \rangle + \frac{1}{2} \frac{\partial^2 \alpha}{\partial q_2^2} \langle q_2^2(t) \rangle + \ldots$$

where $\alpha_0 \langle \Psi_{total} | \Psi_{total} \rangle$ is the time-invariant polarizability determined by the population of the vibrational levels and the n^{th} order expectation value is given by $\langle q_i^n q_j^m(t) \rangle = \langle \Psi_{total} | q_i^n q_j^m | \Psi_{total} \rangle$.

The probe pulse experiences this time-varying polarizability due to propagation in the medium excited with a vibrational coherence. The phase modulation imparted in the probe pulse modifies its spectrum, and the exact nature of the spectral changes provides information about the expectation value of the polarizability, which we see from the expression above directly, provides information about the molecular wave packet dynamics. Thus, the linear expansion term, $\frac{\partial \alpha}{\partial q}$, reveals direct information

about the expectation value of the atomic motion, $\langle q_1(t) \rangle$, the second order term, $\frac{\partial^2 \alpha}{\partial q^2}$, describes light that scatters off of the coherence twice, whereas the cross-term, $\frac{\partial^2 \alpha}{\partial q_1 \partial q_2}$, reveals information about mutual coherences between normal modes in the molecule.

The time-duration of the probe pulse windows the behavior of the wave packet in that it captures the dynamics that occur over the time window defined by the pulse duration. Any wave packet structure that happens on a time-scale much faster than probe time-window appears as a sideband on either side of the original probe spectrum, where its scatter frequency labels the frequency of the dynamic. Any wave packet dynamic structure that happens on a time-scale slower than the probe window simply changes the intensity of the light scattered to the sidebands. Thus, this technique captures dynamics both faster and slower than the time-window of the probe pulse. The fast structure appears in a single-shot measurement, but the slower structure can only be resolved by measuring the probe spectrum as the pump-probe delay is varied on a time-scale longer than the slow behavior.

In our experimental configuration, the probe pulse duration is chosen to be longer than the vibrational period, but shorter than the beat period. As a result, the probe pulse acts as a window in time for observing the dynamics of the vibrational wave packet that can follow the dynamics occurring as a result of the anharmonicity. The power spectrum of the probe spectrum for a given pump probe delay is the windowed Fourier transform, with the intensity of the vibrational sidebands being proportional to the amplitude of the vibrational wave packet. If the probe pulse were longer than

the beat period, then we would resolve the vibrational frequency difference between each excited level, without being able to resolve the temporal evolution of the wave packet.

4.5.2 Rotational dephasing

Any given vibrational level has a manifold of rotational levels that will be thermally populated if the vibrational level is populated. For example, the ground vibrational state has thermally populated rotational levels. When population is transferred to a higher lying vibrational level that associated rotational manifold is also occupied. As mentioned in the introduction to this section, the rotations and vibrations in a molecule are coupled. More formally, this coupling modifies the energy levels, and introduces an additional dephasing mechanism. The spacing of the energy levels of rotational levels have a quadratic spacing given by $E_J = BJ\left(J+1\right)$,where E_J is the rotational energy level, J is the angular momentum, B is the rotational constant which is seen to increase as the vibrational level (i) increases, i.e., $B = B_e + \theta\left(i+\frac{1}{2}\right)$. This rotational dephasing modulates the amplitude of the oscillations in $\langle q(t)\rangle$, and therefore, the intensity of the sidebands as a function of delay.

Including rotational dephasing in the calculations above leads to the following modification in the expression for expectation value of the polarizability

$$\langle\alpha(t)\rangle = \langle\alpha(t)\rangle_{vib} \sum_J P_J \exp\left[-i\theta J\left(J+1\right)t\right],$$

where $\langle\alpha(t)\rangle_{vib}$ is the expectation value calculated neglecting rotational effects, and $P_J = \exp\left(-\dfrac{BJ\left(J+1\right)}{kT}\right)$ is the thermal occupation probability of the rotational

levels. The experimental results show both the behavior of the vibrational anharmonicity as well as the rotational dephasing.

4.6 Overtone excitation

In the past, work to control vibrational motion in solids and molecules has been criticized as not being particularly useful because exciting the first vibrational level ($\nu = 1$), for example, does not correspond to large changes in bond length in a molecule. One might expect that a pulse twice as short as the vibrational period of a given mode will allow efficient excitation of the second vibrational level (or 1^{st} overtone; $\nu = 2$) since this would result in a large power spectral density at this frequency. However, if we consider a harmonic oscillator, the matrix element for direct excitation across two levels ($\nu = j$ to $\nu = j + 2$) is zero. Since the vibrational levels are in an anharmonic potential this transition is allowed, but the matrix element for $\Delta\nu = \pm 2$ is roughly an order of magnitude weaker than for $\Delta\nu = \pm 1$. This prevents efficient excitation of overtone levels directly from the ground vibrational level.

The impulsive Raman excitation using two chirped pulses described in the previous section demonstrated linear excitation of the first vibrational level. Because these pulses were highly chirped, their peak intensity is relatively low. Excitation of Raman modes exhibit different behavior when driven by intense, transform-limited pulses. For transform-limited pulses, the first pulse creates a wave packet that begins to evolve. The second pulse then generates another wave packet, which interferes with the first, enhancing or suppressing modes in the wave packet depending

on the delay between pulses. For a purely linear response, we expect the two-pulse transform-limited experiment to follow the same behavior as the chirped pulse impulsive Raman excitation. Any differences between the chirped and transform-limited excitation that we observe indicate a nonlinear response of the molecular system to an intense transform limited pulse.

To consider the effect of anharmonicity on the polarizability, we consider only one, isolated normal coordinate that has been diagonalized in terms of the eigenfunctions ϕ that are orthogonal. Note that the potential considered here is anharmonic. The total wavefunctions is then written in terms of an orthonormal expansion of the eigenfunction

$$\Psi_{total}(t) = \sum_i a_i \phi_i e^{i\omega_i t}. \tag{4.3}$$

Using the Taylor expansion of the polarizability introduced above, the expectation value of the polarizability can be written as

$$\langle \alpha(t) \rangle = \left\langle \sum_i a_i \phi_i e^{i\omega_i t} \middle| \alpha_0 + \frac{\partial \alpha}{\partial q} q + \frac{1}{2} \frac{\partial^2 \alpha}{\partial q^2} q^2 \middle| \sum_j a_j \phi_j e^{i\omega_j t} \right\rangle . \tag{4.4}$$

Note, the first term in the expansion is time-independent and can represented by a constant

$$\alpha_0 \sum_{i,j} \langle a_i \phi_i | a_j \phi_j \rangle \exp\left[i \left(\omega_i - \omega_j \right) t \right] = \alpha_0 \sum_i |a_{ii}|^2 \equiv \widetilde{\alpha}.$$

Again, we note that by factoring out the expansion coefficients for the polarizability,

$$\langle \alpha(t) \rangle - \widetilde{\alpha} = \frac{\partial \alpha}{\partial q} \langle q \rangle + \frac{1}{2} \frac{\partial^2 \alpha}{\partial q^2} \langle q^2 \rangle ,$$

it is clear that, to first order, the polarizability is a direct measure of the wave packet dynamics of the vibrational coordinate $\langle q(t) \rangle$. In general, we can write the n^{th} order

expectation value of the vibrational coordinate q as

$$\langle q^n \rangle = \sum_{i,j} \langle a_i \phi_i \left| q^n \right| a_j \phi_j \rangle \exp\left[i \left(\omega_i - \omega_j \right) t \right] = \sum_{i,j} a_i^* a_j M_{i,j}^n \exp\left[i \left(\omega_i - \omega_j \right) t \right],$$

where the matrix elements are defined as $M_{i,j}^n = \langle \phi_i \left| q^n \right| \phi_j \rangle$. Thus, the time-dependent portion of the molecular polarizability along a given coordinate can be written as

$$\langle \alpha(t) \rangle - \widetilde{\alpha} = \sum_{i,j} a_i^* a_j \left[\frac{\partial \alpha}{\partial q} M_{i,j}^1 + \frac{1}{2} a_i^* a_j \frac{\partial^2 \alpha}{\partial q^2} \sum_{i,j} M_{i,j}^2 \right] \exp\left[i \left(\omega_i - \omega_j \right) t \right] \cdot$$

For a harmonic potential, $M_{i,j}^1 = 0$ for $j \neq i \pm 1$, and this means that no direct excitation of overtone levels (e.g., a transition directly from $i = 0$ to $i = 2$, etc.) is possible. The anharmonicity relaxes this selection rule, however, $M_{i,i\pm2}^1$ is typically an order of magnitude smaller than $M_{i,i\pm1}^1$. Moreover, in the case of a harmonic oscillator, each term in any given sum oscillates at exactly the same frequency and there is no dephasing or rephasing of the terms, i.e., no spreading and revival of the wave packet. However, in the case of an anharmonic oscillator, the terms in the sums will beat against each other with a characteristic beat frequency given by the anharmonicity of the potential.

The primary question is, however, how does excitation of vibrational overtones manifest itself in the expectation value of the polarizability, and, therefore, in the power spectrum of the phase-modulated probe pulse? To better understand the expected effect on the power spectrum of the probe pulse, we consider the case in which we have excited only one overtone (i.e., we have population in levels $i = 0, 1, 2$). Furthermore, let's restrict our attention to the linear component of the expansion of

the polarizability. In this approximation, the time-dependent polarizability can be written as

$$\langle\alpha(t)\rangle - \widetilde{\alpha} = \frac{\partial\alpha}{\partial q}\left\{a_0^* a_1 M_{0,1}^1 \exp\left[-i\left(\omega_1 - \omega_0\right)t\right] + a_1^* a_2 M_{1,2}^1 \exp\left[-i\left(\omega_2 - \omega_1\right)t\right] + c.c.\right\}.$$

For a harmonic potential, $\Omega_v = \omega_1 - \omega_0 = \omega_2 - \omega_1$, and this would lead to the scattering of one sideband in the probe spectrum with an intensity given by the coherent sum of the vibrational populations. However, this is not the case for an anharmonic potential, where $\omega_1 - \omega_0 = \omega_2 - \omega_1 - \Delta$ and $\Delta \ll \omega_1 - \omega_0$ is the anharmonicity. Note the conventional notation of the anharmonicity is $\Delta = 2x_e\omega_e$.

The effect of the anharmonicity on the probe spectrum depends on the time-scales involved. If the probe pulse is longer than $1/\Delta$, then two spectral resolved sidebands will appear in the probe spectrum at the scattered frequencies $(\omega_1 - \omega_0)$ and $(\omega_2 - \omega_1)$. However, as in our experimental conditions, if the probe pulse duration is longer than $1/\Delta$, the intensity of the sidebands is modulated with pump-probe delay because the anharmonic beating creates an envelope on the polarizability. As will be demonstrated in a later section, the anharmonicity is observed as modulations in the sideband scattered intensity as the pump-probe delay varies.

Generally, many overtone levels may be excited. Those overtone levels will induce a time-dependent polarizability at approximately the vibrational frequency for coherences between neighboring levels (i.e., $j = i \pm 1$). The frequency of oscillation for the polarizability between any pair of levels i and j is written as $\omega_i - \omega_{j=i\pm1} = \Omega_v - \Lambda(i)$, where Ω_v is the fundamental vibrational frequency and $\Lambda(i)$ is the change in the energy level spacing for the i^{th} level. For the Morse potential, the frequency change

can be written, to a good approximation, as $\Lambda(i) = i\Delta$.

With the energy level spacing in mind, we can write an expression for the time-dependent polarizability exhibited by a highly excited anharmonic oscillator. Considering only coherences between neighboring vibrational levels ($j = i \pm 1$), we arrive at the expression

$$\langle \alpha(t) \rangle - \widetilde{\alpha} = \frac{\partial \alpha}{\partial q} \left\{ \sum_{i=0}^{n} a_i^* a_{i+1} M_{i,i+1}^1 \exp\left[-i\left(\Omega_v - i\Delta\right) t\right] + c.c. \right\}.$$

This can be rewritten as a Fourier cosine series expansion

$$\langle \alpha(t) \rangle - \widetilde{\alpha} = 2\frac{\partial \alpha}{\partial q} \left\{ \sum_{i=0}^{n} a_i a_{i+1} M_{i,i+1}^1 \cos\left[\Omega_v t - i\Delta t\right] \right\}.$$

For our experimental conditions, the fundamental vibrational frequency is much faster than our probe pulse duration, while the time-scale of the anharmonicity is much slower than the probe pulse duration. As a result, we can separate the anharmonic contribution as a slowly-varying envelope,

$$M(t) = 2\frac{\partial \alpha}{\partial q} \left\{ \sum_{i=0}^{n} a_i a_{i+1} M_{i,i+1}^1 \cos\left[i\Delta t\right] \right\},$$

from the fundamental vibrational frequency component $\cos\left[\Omega_v t\right]$, and arrive at the expression

$$\langle \alpha(t) \rangle - \widetilde{\alpha} = M(t) \cos\left[\Omega_v t\right].$$

In the probe spectrum, we will see light scattered to a sideband of the fundamental vibration, and the intensity of that sideband will be modulated as the pump-probe time delay is varied, where the scattered intensity is proportional to $M(t)$. With a sufficiently long pump-probe scan, we can perform a Fourier transform the sideband

intensity signal, which is nearly equivalent to Fourier transforming $M(t)$, the linearity of the process is compromised by the fact that the sideband intensity is related through a Bessel function transformation. It is clear, however, that we will see a spike in the spectrum of the sideband lineout for each overtone excited, and that the relative strength of each peak in the spectrum will be determined by the relative strength of the coherences that connect neighboring vibrational levels. In the experimental arrangement, the probe pulse passes through many molecules, each with an excited vibrational coherence. We can write the overall phase modulation imparted on the probe pulse as the product of the phase-modulation of each individual molecule

$$\exp\left[-i\frac{N}{\varepsilon_0}\left\langle\alpha(t)\right\rangle\right],$$

where N is the number of molecules.

Another possible source of sideband intensity modulation is from isotopic variations of the molecules. Such isotopes exhibit a slight shift in the vibrational frequencies that are on the order of the anharmonicity, and care must be taken to carefully consider the two effects. The isotopic contribution to the time-dependent index of refraction can be approximated as

$$n^2(t) \approx 1 + \frac{N_{tot}}{\varepsilon_0}\widetilde{\alpha} + \frac{N_{tot}}{\varepsilon_0}\sum_l f_l M_l(t)\cos\left[\left(\Omega_v - \delta_l\right)t\right],$$

N_l is the number of the l^{th} isotope present, N_{tot} is the total number of molecules present, δl is the isotopic frequency shift, and $fl = N_l/N_{tot}$ is the isotopic fraction. If the resolution of the spectrometer that detects the probe spectrum is sufficient to resolve the isotopic frequency shift, each isotopic contribution will appear as a

separate sideband. However, as in the case of our experiment, if the spectrometer can not resolve the individual isotopes, there is an additional modulation on the sideband intensity due to the beating of the isotope frequencies in the spectrometer. This additional beating must be separated from the anharmonic beating in the experiment.

4.6.1 Experimental measurements

In order to observe the evolution of a vibrational wave packet in a single mode, created by a single intense, non-resonant impulsive pump pulse, we monitored the probe pulse power spectrum as a function of pump probe delay after ISRS excitation by a transform-limited pump pulse. The result of such a scan in SF_6 is shown in Figure 4.11. There is one strong Raman active mode in this molecule, the symmetric $S-F$ stretch breathing mode, which is not strongly coupled to any other mode. The frequency of this mode is 775 cm^{-1} (23.25 THz). Figure 4.11(a) shows the probe pulse power spectrum as a function of the delay and Figure 4.11(b) shows the intensity of the light scattered at 775 cm^{-1} (23.25 THz) away from the probe central frequency as a function of the delay. The position of zero delay is marked by a significant distortion and broadening of the probe power spectrum as a result of cross phase modulation of the probe pulse as it co-propagates through the gas with the pump. The data shows the dephasing of the wave packet and its subsequent rephasing at a time delay of about 26 ps. The overall decay of the signal is consistent with rotational dephasing. Identical measurements were made at several different pressures between 20 and 100 torr in order to ensure that the decay is not a result of collisional dephasing.

The probe pulse spectrum vs. pump probe delay was also recorded for CO_2,

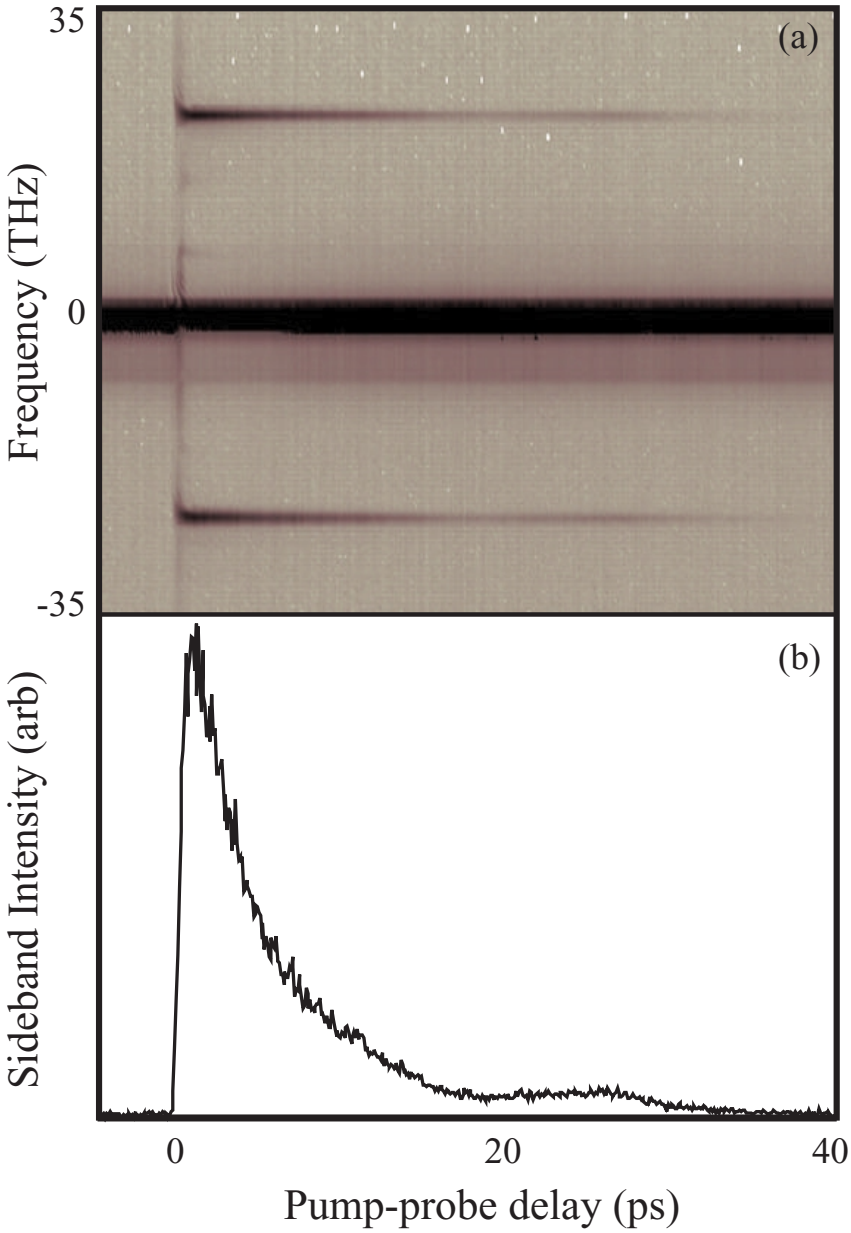

Figure 4.11: The probe spectrum measured as a function of delay from the pump pulse (a). The sideband intensity, corresponding to the symmetric breathing mode, shows beating structure due to overtone excitation.

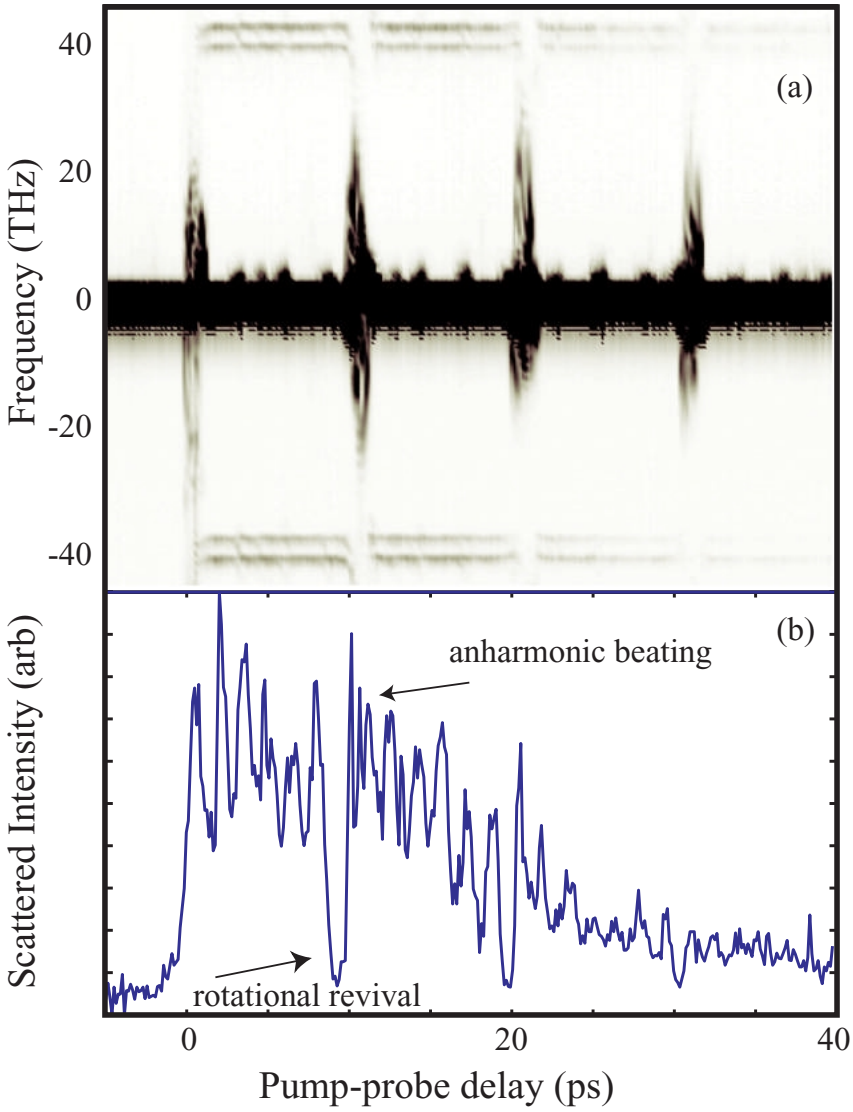

Figure 4.12: The probe spectrum measured in CO_2 as a function of delay from the pump pulse (a). Scattered probe light at 41.64 THz in CO_2 shows beating due to overtone excitation (b).

and this data also exhibits observe evidence for overtone excitation as illustrated in Figure 4.12. The pump pulse used here is short enough to impulsively excite both of the Fermi resonance coupled Raman active modes: ν_1 and ν_4. Figure 4.12(a) shows the excitation of both modes in addition to the excitation of a rotational wave packet. The effect of the rotational wave packet is a periodic broadening of the probe spectrum at full and fractional revivals of the wave packet.

The apparent disappearance of the vibrational sidebands at rotational revivals is simply a result of the fact that the probe spectrum becomes extremely broad, reducing sideband visibility. Figure 4.12(b) shows the probe intensity scattered as by ν_1 as a function of pump probe delay. Modulations are evident which can be attributed once again to the dephasing and rephasing of the vibrational wave packet. We measure rephasing with a period of 1.47 $\pm$ 0.1 ps, implying a 0.681 $\pm$ 0.093 THz (22.7 $\pm$ 3.1 cm^{-1}) anharmonicity, in agreement with published values [108]. An alternate technique can measure the anharmonicity of IR active modes in organic molecules by observing the beating of vibrational echo signals initiated by pairs of IR free-electron laser (FEL) pulses [109]. In contrast, our technique measures the anharmonicity of Raman active modes with non-resonant ISRS excitation.

Figure 4.13(a) shows the probe spectrum for CCl_4 as a function of pump probe delay and Figure 4.13(b & c) shows the intensity of the probe at frequencies of 460 cm^{-1} (13.77 THz) and 556 cm^{-1} (16.8 THz), respectively. Note that there are sidebands at frequencies that do not correspond to Raman active modes in CCl_4, such as the ones at 556 cm^{-1} (16.8 THz), and that the modulations in Figure 4.13(b

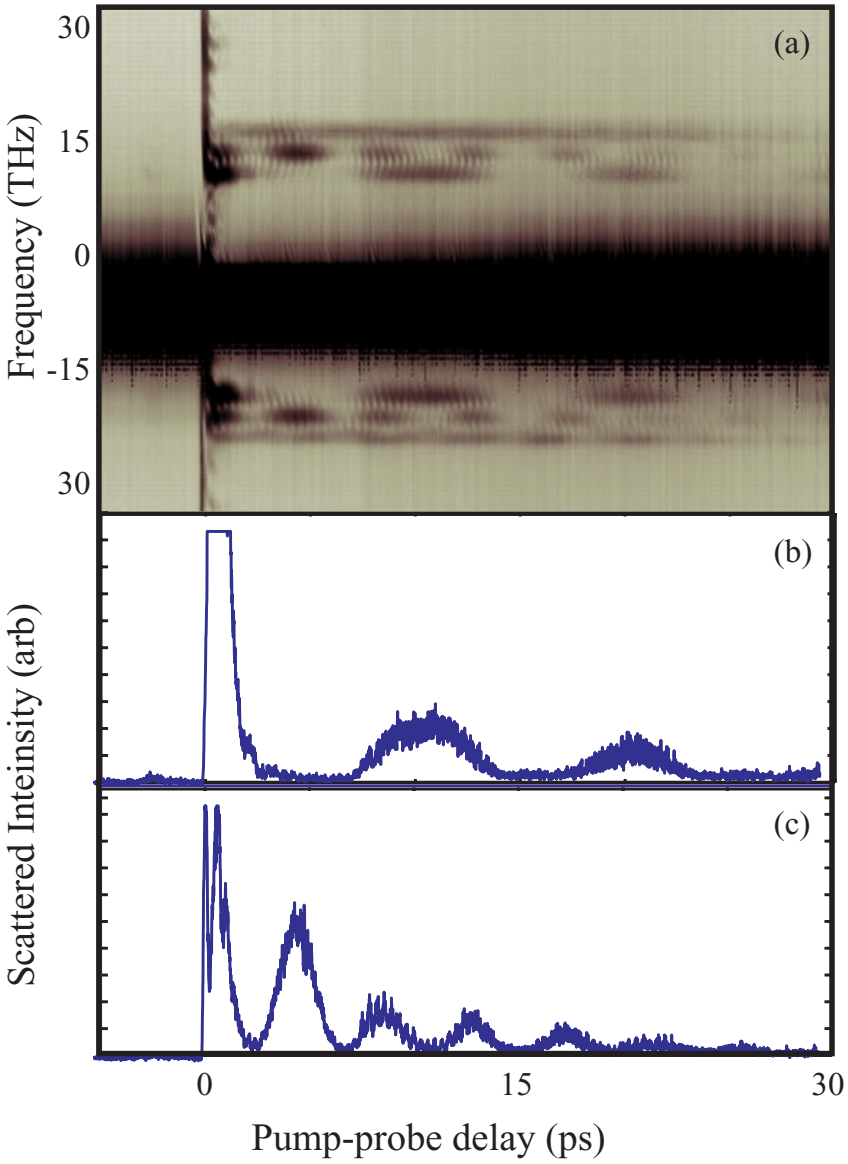

Figure 4.13: The probe spectrum measured in CCl_4 as a function of delay from the pump pulse (a). Scattered probe light at 13.77 THz in CCl_4 shows beating due to overtone excitation (b). A new mode not attributable to CCl_4 at 16.8 THz also demonstrates vibrational overtones.

& c) are much more pronounced than those in Figure 4.12(b). The new sidebands can be explained in terms of photo dissociation of the CCl_4 and the depth of modulation is a result of two independent factors, which come to light in a detailed analysis of the data.

In order to understand the pronounced beats in the CCl_4 wave packets as well as the new sidebands, we performed a Filter Diagonalization decomposition of the data shown in Figure 4.13(b & c). This allows us to discern features in the spectrum of the sideband evolution data that are not resolvable in a Fourier transform. Panels (a) and (b) of Figure 4.14 show three representations of the spectra of the curves shown in Figure 4.13(b & c). The decomposition assumes that the signal, $S(t)$ can be fit to the functional form $S(t) = \sum_i a_i e^{-\Gamma_i t} \cos(\omega_i t + \phi_i)$. The decomposition provides information on the frequencies, ω_i, phases, ϕ_i, and decay constants, Γ_i of the signal. These results for the data shown in Figure 4.14(a & b) are shown in Table 4.1. The table contains two major contributions to the spectrum of each data set in Figure 4.13 and both of these frequencies are evident as peaks in Figure 4.14(a & b) .

Filter Diagonalization of Figure 4.13(b & c)		
Mode Frequency	ω_i (cm^{-1})	$a_i(relative)$
460 cm^{-1}	8.2	0.52
460 cm^{-1}	3.3	0.48
556 cm^{-1}	7.8	0.67
556 cm^{-1}	5.5	0.33

Table 4.1: Filter Diagonalization of Figure 4.13(b & c).

The table contains two major contributions to the spectrum of each data set in Figure 4.13 and both of these frequencies are evident as peaks in Figure 4.14 panels

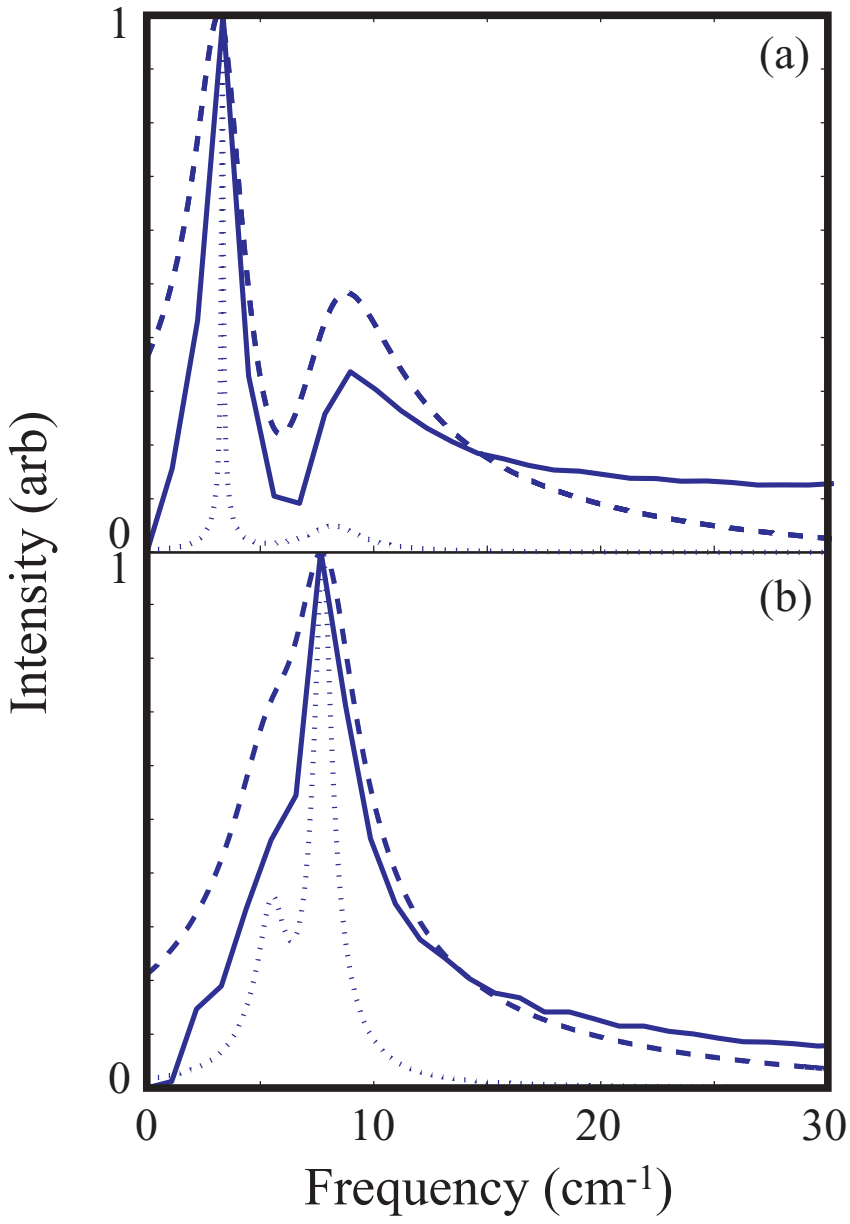

Figure 4.14: Filter Diagonalization decomposition of scatter light from CCl_4.

(a) and (b). The three curves in Figure 4.14(a & b) are two spectra calculated from the fitting coefficients in Table 4.1 as well as Fourier transforms of the data in Figure 4.13(b & c). The spectra, $S_1(\omega)$ and $S_2(\omega)$, were calculated from Table 4.1were calculated according to

$$S_1(\omega) = \sum_i \frac{a_i}{\omega + i\Gamma - (\omega + i\Gamma)_i}$$

$$S_2(\omega) = \sum_i \frac{-|a_i|\,\Gamma_i}{(\omega - \omega_i)^2 + \Gamma^2}$$

The solid curves in Figure 4.14 are the Fourier transforms of the data in Figure 4.13, the dashed lines are $S_1(\omega)$, and the dotted lines are $S_2(\omega)$. The two spectra, $S_1(\omega)$ and $S_2(\omega)$, illustrate the ability of the Filter Diagonalization technique to resolve contributions to the structure in the Fourier transform of the datasets. The pair of peaks in both data sets can be explained in terms of an isotopic mixture of Cl in the CCl_4, and beating between vibrational levels with an anharmonic energy spacing.

In the case of the mode at 460 cm^{-1} (13.77 THz), the contributions from the isotope beating and the beating between the overtone states are similar in magnitude, indicating that they are roughly equally responsible for the depth of modulation evidenced in the data shown in Figure 4.13(b). There are three different measured frequencies of vibration for ν_1 in CCl_4 , which beat against each other. These are 465 cm^{-1}, 462 cm^{-1}, and 459 cm^{-1}, leading to a beat frequency of 3 cm^{-1}. The low frequency peak at 3 cm^{-1} is a result of the beatings of wave packets in molecules with different isotopic content. The higher frequency peak is presumably due the beating of many vibrational states whose energy differs by the anharmonicity of the potential.

Note that in Table 4.1, the contributions from the isotope beating and the beating between the states are similar, indicating that they are roughly equally responsible for the depth of modulation evidenced in the data shown in Figure 4.13(b). This depth of modulation is much deeper than the modulation in the CO_2 data (i.e., more distinct dephasing and revivals), indicating the participation of more states in the wave packet

The wave packet excited in CCl_4 consists of more states than the wave packet in CO_2, resulting more distinct dephasing and revivals. The CO_2 sideband signal never completely disappears between revivals, as it does in the case of CCl_4, because the wave packet is composed of mostly $\nu = 0$ and $\nu = 1$ with small contributions from $\nu = 2$ and higher states. This is consistent with a simple classical picture of the impulsive excitation. The pump pulse duration is several times shorter than the vibrational period of modes at 460 cm^{-1} (13.77 THz) and 556 cm^{-1} (16.8 THz), whereas in the case of CO_2, the pump pulse duration is barely shorter than the frequency of both excited modes. In a simple classical excitation picture, the excitation is a highly nonlinear function of pulse duration that grows rapidly with decreasing pulse duration [104] $Q(\tau) = \int \cos(\omega_0 t) \exp\left[-(t/\tau)^2\right]$, where Q is the impulse transferred to the molecule and is the pulse duration for a Gaussian pulse profile. Therefore, modes with vibrational periods much greater than the pulse duration will feel a much greater 'kick' than modes with periods near the pulse duration.

The second factor contributing to the large depth of modulation in Figure 4.13(b) and (c) is the excitation of wave packets in molecules containing difference isotopes

of Cl. There are two dominant naturally occurring isotopes: Cl^{35} and Cl^{37}. This gives rise to three different frequencies of vibration of ν_1 in CCl_4, which beat against each other. These are 465 cm^{-1},462 cm^{-1} and 459 cm^{-1}, leading to a beat frequency of 3 cm^{-1}.

Further evidence of overtone excitation in CCl_4 is provided by Figure 4.8(c), which shows the probe spectrum obtained after excitation of CCl_4 with two time-delayed transform-limited pulses. This can also be seen by performing a 1-D Fourier transform of the data in Figure 4.8(c) to produce a data set similar to that of Figure 4.8(a). Figure 4.15 shows such a transform in which various modes and mode combinations can be seen. The two transform-limited pulses excite not only the normal modes of the system, but also overtones and combination modes not observed in the chirped pulse data of Figure 4.8(c).

The light scattered at the frequency $2\nu_1$ in Figure 4.15 shows two local maxima, only one of which lies on the line of slope 1. The maximum occurring with a pulse periodicity of $1/\nu_1$ cannot be unambiguously assigned to light scatter from the overtone as it may include light scattered twice from ν_1. The second spot marked is scattered to a frequency $2\nu_1$ and has a periodicity of $\sim 1/2\nu_1$, providing unambiguous evidence for overtone excitation.

4.6.2 Excitation of dissociated molecular fragments

Figure 4.16 reveals more interesting rotational structure. In addition to the rotational revivals that can be attributed to CO_2, we see additional structure resulting in more minor modifications to the probe spectrum. The spacing of these can be

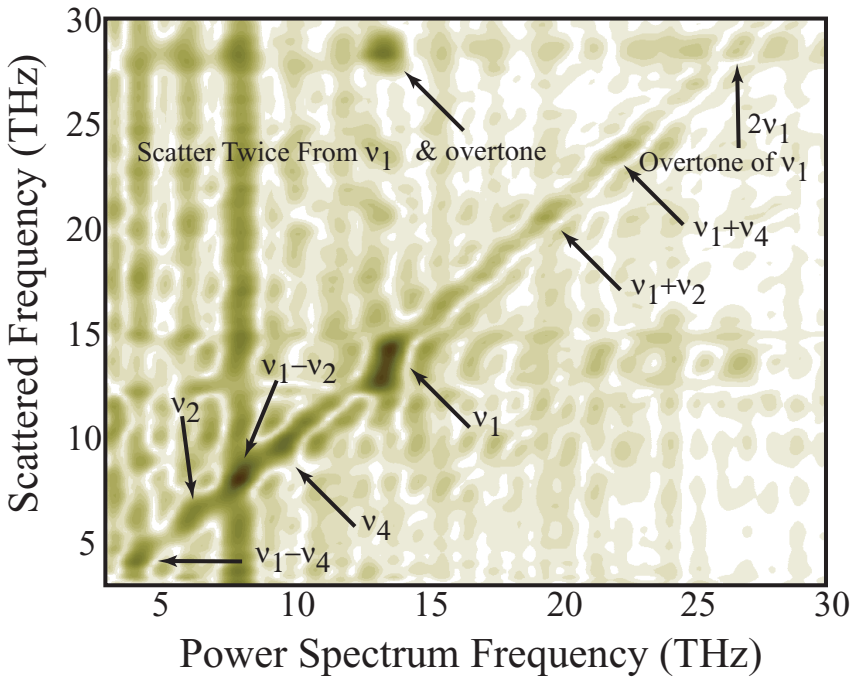

Figure 4.15: Data from Figure 4.8(c) where the temporal data at each scattered frequency is Fourier transformed. The shaded regions indicate the power spectral density.

exactly matched to the expected revival times of rotational wave packets of O_2 and CO. This provides evidence that this structure is due to dissociation of CO_2 leading to the formation of O_2 and CO.

Photo-dissociation of CCl_4 is evident by examining the 556 cm^{-1} mode of Figure 4.13(c). The two corresponding peaks in Figure 4.14(b) provide a key for understanding the source of the new sidebands. The vibrational frequency of 556 cm^{-1} is consistent with that of Cl_2^{35} and the two peaks in Figure 4.14(b) agree exactly with the measured anharmonicity of Cl_2 and the vibrational energy differences between molecules composed of different isotopes. The vibrational frequencies for Cl_2^{35}, $Cl^{37}Cl^{35}$ and Cl_2^{37} are 556 cm^{-1}, 548 cm^{-1} and 540 cm^{-1} respectively. This gives rise to a beat frequency between the isotopes of 7.8 cm^{-1}. The anharmonicity is 5.53

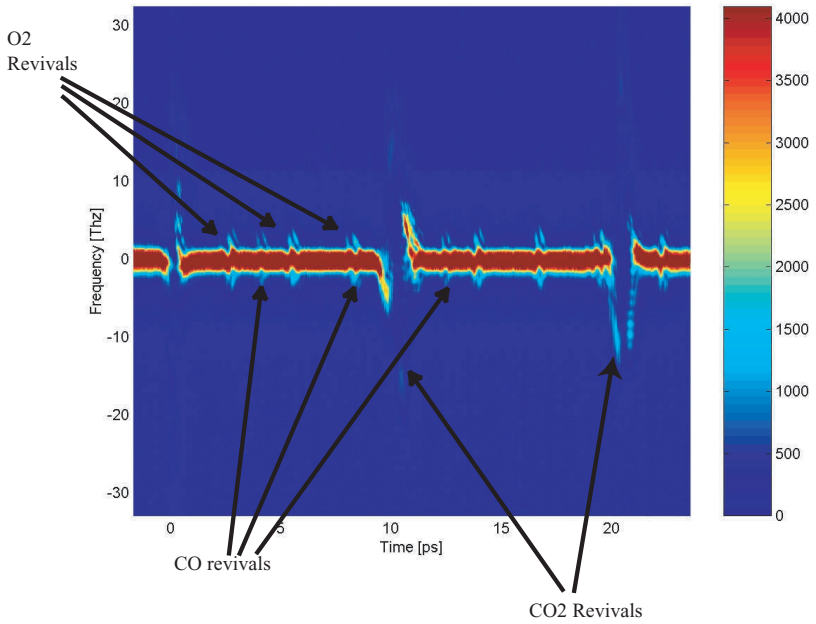

Figure 4.16: Rotational revival structure indicating that the CO_2 is dissociated into CO and O_2.

cm^{-1}.

Perhaps the most important evidence for assignment of the new modes in the probe spectrum is that they only appeared after several pump laser pulses were incident on the sample. Figure 4.17 shows the buildup of the new Raman peak at 556 cm^{-1} and the decay of the signal at 460 cm^{-1} as measured by the sideband intensities at those frequencies. The growth of the peak at 556 cm^{-1} is accompanied by a decay of the signal at 460 cm-1, which is consistent with a laser driven dissociation of the CCl_4 to produce Cl_2. We also monitored the decay of the new peaks with time and found the decay to be consistent with diffusion of the new products to locations in the waveguide assembly where they do not interact with the laser pulse. Further studies are underway to improve our understanding of the dissociation process and determine

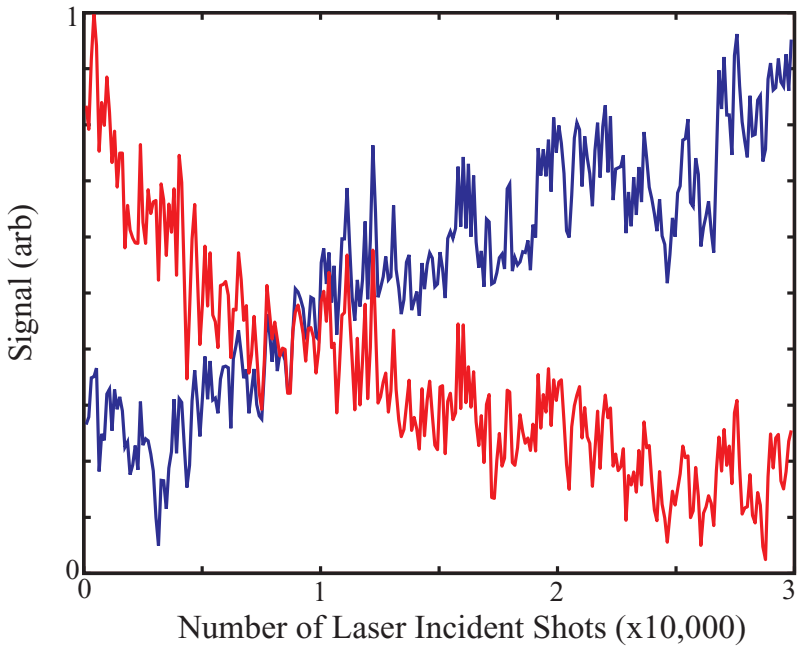

Figure 4.17: Growth of Cl_2 at the expense of CCl_4, indicating macroscopic photodissociation.

whether or not the formation of the Cl_2 is the result of a concerted reaction.

4.6.3 Observation of combination band evolution

Figure 4.18 shows three lineouts from Figure 4.8(a) and demonstrates our ability to excite a combination mode that is a coherent sum of two different normal modes. By adjusting the delay between pump pulses to $1/(\nu_1 - \nu_4)$, we can excite vibrational motion that is a combination of the ν_1 and ν_4 modes of the molecule (lowest lineout in Figure 4.18, at position A) where no individual excitation of modes ν_1 or ν_4 is observed. This indicates that the probe does not simply acquire modulations at the difference frequency through optical mixing of the two normal mode frequencies, but rather that it is modulated by the motion of the molecule in the combination mode. Position B marks a delay between pump pulses for which the excitation of both

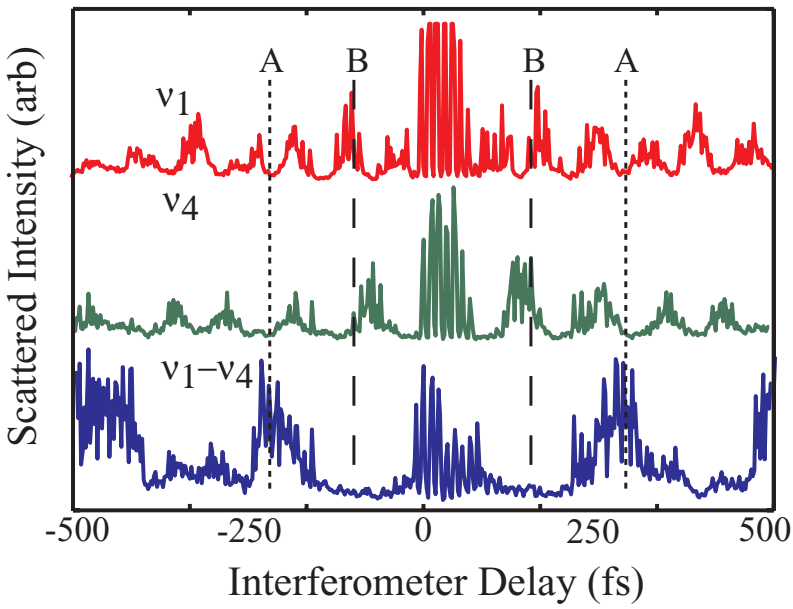

Figure 4.18: Probe spectrum of CCl_4 excited by two transform-limited pulses. (a) Probe spectrum vs. time delay between pump pulses. (b) Lineouts at frequencies corresponding to ν_1, ν_4, and $\nu_1 - \nu_4$.

normal modes is maximum, but where there is no excitation of the combination mode. Excitation of such combination modes is an important step toward bond selective excitation, since reaction coordinates do not always correspond to normal modes of molecules.

4.7 Modification of a bimolecular reaction rate

From the example in the previous section, we see that new product formation can be determined by monitoring the vibrational or rotational spectroscopic information obtained from probe energy scattered by molecular motion. This was an example of a unimolecular reaction. We have also observed evidence of a bimolecular reaction occurring in the hollow core fiber. When we introduce both carbon tetrachloride vapor and carbon dioxide gas along with the laser pulses, we observe new Raman

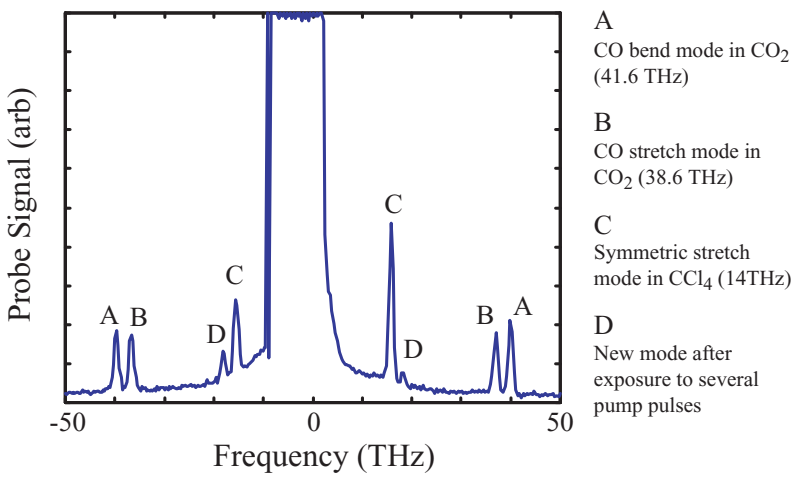

Figure 4.19: We observe new modes that appear and grow with time when Carbon Dioxide, Carbon Tetrachloride, and laser pulses are introduced into the gas cell.

active vibrational modes that appear as sidebands at a frequency of 580 cm^{-1}, as shown in Figure 4.19. These sidebands match those of Phosgene (CCl_2O). To confirm the presence of Phosgene as a reaction product, we sampled a gas mixture that had been exposed to many laser shots. An FTIR scan of the sample revealed IR absorption features that matched those present in Phosgene. As an initial test to determine if this reaction was sensitive to the shape of the driving laser pulse, we used the learning algorithm to feed back on the intensity of Phosgene sideband signal. The algorithm converged to an optimal solution.

The main question that arises is whether or not this reaction is due to coherent control, or due to photochemistry? A possible explanation is that a multiphoton process causes photo-induced dissociation of the reactants, which in turn drives the reaction. To rule out this possibility, we normalized the shaped and transform-limited pulses so that they had the same integrated second-harmonic intensity. When the pulse energies were adjusted to fulfill this condition, we then measured the sideband

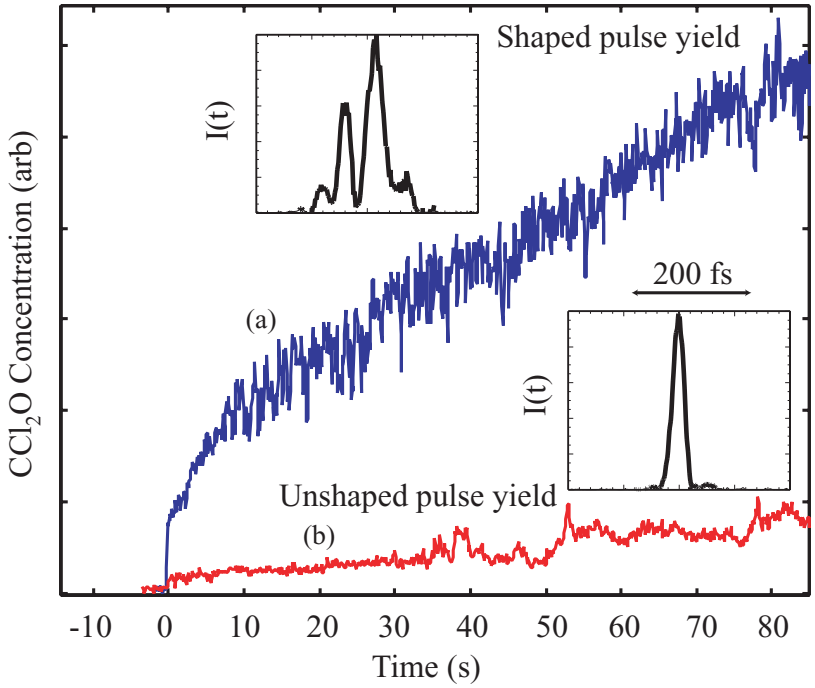

Figure 4.20: Comparison between the reaction rates measured for an optimally shaped (a) and transform-limited (b) laser pulse.

intensity of the Phosgene production as a function of the number of laser shots introduced into the reaction cell. The results in Figure 4.20 show that the shaped laser pulse induces a much higher reaction rate than the unshaped laser pulse. This indicates that there is a pulse-selective modification of the bimolecular reaction rate. Further experiments are required to confirm this. The ideal experiment would show that for equal pulse energies that the shaped laser pulse has a higher reaction rate. These results do show, however, that the difference in the reaction rates is not simply due to a high-order multiphoton induced chemistry.

In should also be noted that this experiment is **dangerous**. Phosgene is a chemical weapons agent used in WWI, and gas that escapes into the laboratory will kill the occupants. For this reason, once the product was identified, we stopped this series of

experiments. I strongly discourage anyone reading this document from attempting this experiment because it *may result in death.*

4.8 Self-seeding of vibrational motion

In order to control vibrational motion in molecules with ISRS, it is necessary to "hit" the molecule with an excitation pulse whose time duration is shorter than the vibrational period we wish to excite. Moreover, the molecular motion must result in a change in the molecular polarizability so that there is a finite Raman cross-section. This excitation pulse need not be a single, isolated short pulse, but can also be a longer pulse with structure that has time duration shorter than the vibrational period. As explained in this Chapter, the ability of a pulse to excite a given vibrational mode is determined by the spectral density of the intensity profile at the vibrational frequency. This provides a quantitative measure of the amount of structure in the intensity profile at that frequency.

In this section, I detail the results of a set of experiments that show that pulse propagation in a medium prepared with a Raman coherence reshapes the excitation pulse, increasing the structure at the vibrational frequency in the pulse. This is in essence a "self-modification" phenomenon where the molecules reshape the excitation pulse to be "more optimal" in exciting the molecules vibrational mode.

4.8.1 Reshaping of the ISRS pump pulse

When a laser pulse causes ISRS excitation, the pump pulse spectrum experiences a red-shift as a result of the energy lost in exciting the vibrational mode. For ISRS, the amount the pump spectrum shifts is determined by the number of Raman modes

excited (and therefore energy lost) [104], and we routinely observed this effect in all of the molecular systems we excited. The modification to the spectrum and phase of the pump pulse will certainly be reflected in the time-domain. I studied this effect by measuring the change in the pulse shape in the bend mode (41.64 THz) of CO_2 as I varied the pressure of the gas. I measured the pulse shape out of the fiber using SHG FROG [72] to quantify the changes.

Figure 4.21(a) shows a series of pump pulses that excite a vibrational coherence in CO_2 at pressures ranging from 20 - 800 torr. Notice that as the gas pressure increases, the intensity profile of the pulses is modified. The increase in the level of excitation of the vibrational mode is accompanied by an increase in the power spectral density of $I(t)$ at the vibrational frequency, as shown in Figure 4.21(b). At higher pressures, the spectral density at the vibrational frequency becomes larger than the transform-limited value. This provides a clear indication that the fraction of the pulse energy that has structure at 1/(41.6 THz) (see Figure 4.21(c)) in the temporal structure is increasing as the pressure, and therefore, the excitation of the vibrational motion. Thus, a pump pulse that impulsively excites a vibrational mode in a molecule will experience a reshaping of its intensity profile in a way that more efficiently excites that vibrational mode. This implies that a pump pulse that is too long to excite a given vibrational mode may be able to excite that mode provided it somehow develops a small amount of temporal structure that allows it to initially excite, or "seed", the vibrational mode.

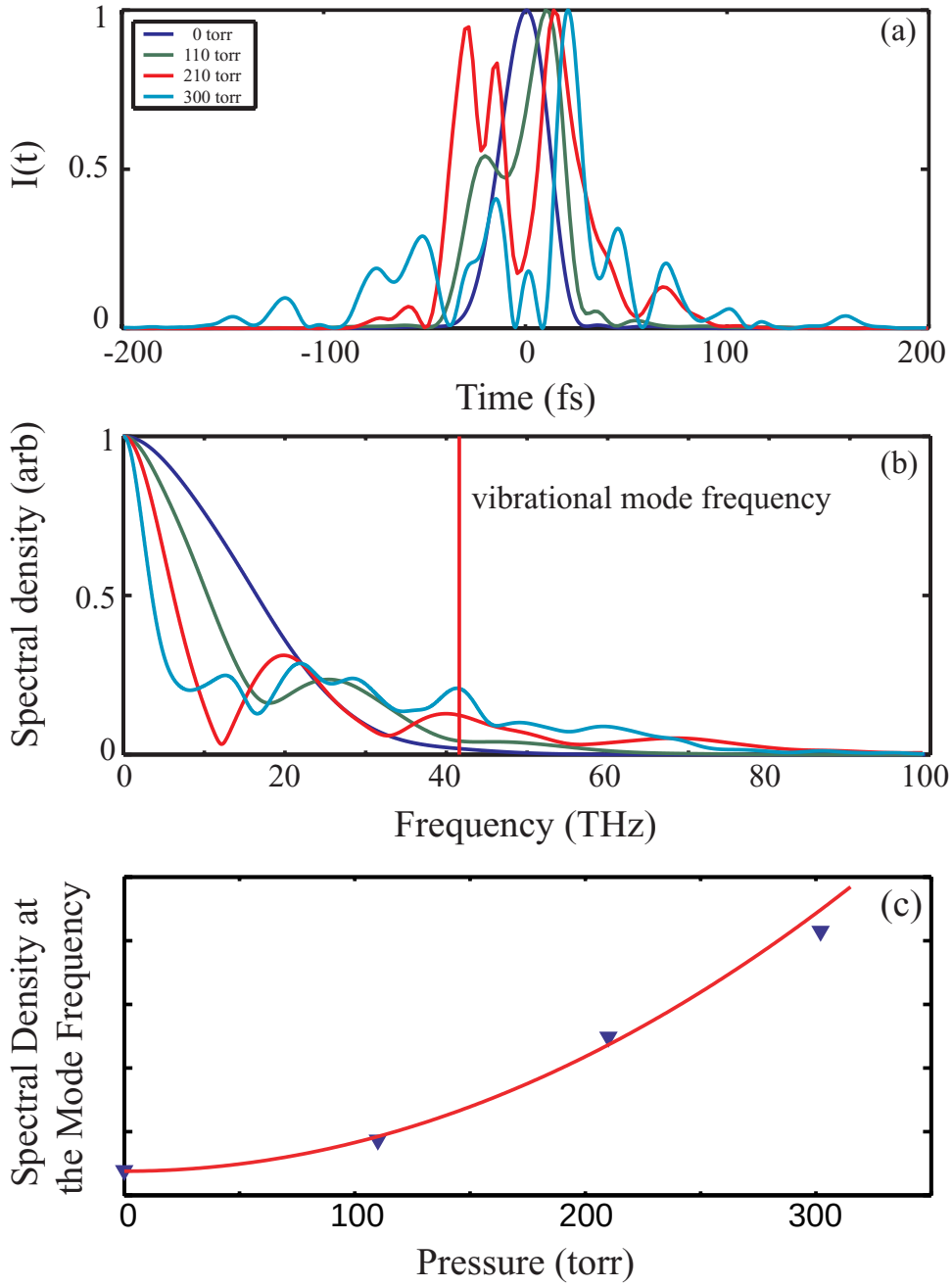

Figure 4.21: As the pump pulse that impulsively excites vibrations in a molecule is seen to reshape into a pulse with more structure at the mode frequency. The measured pulse shapes (a) show significant distortion at higher pressures. The power spectra of the intensity profiles (b) reveals the energy redistribution adds significant energy to the vibrational mode. The energy redistribution into structure at the vibrational period grows quadratically with increased gas pressure.

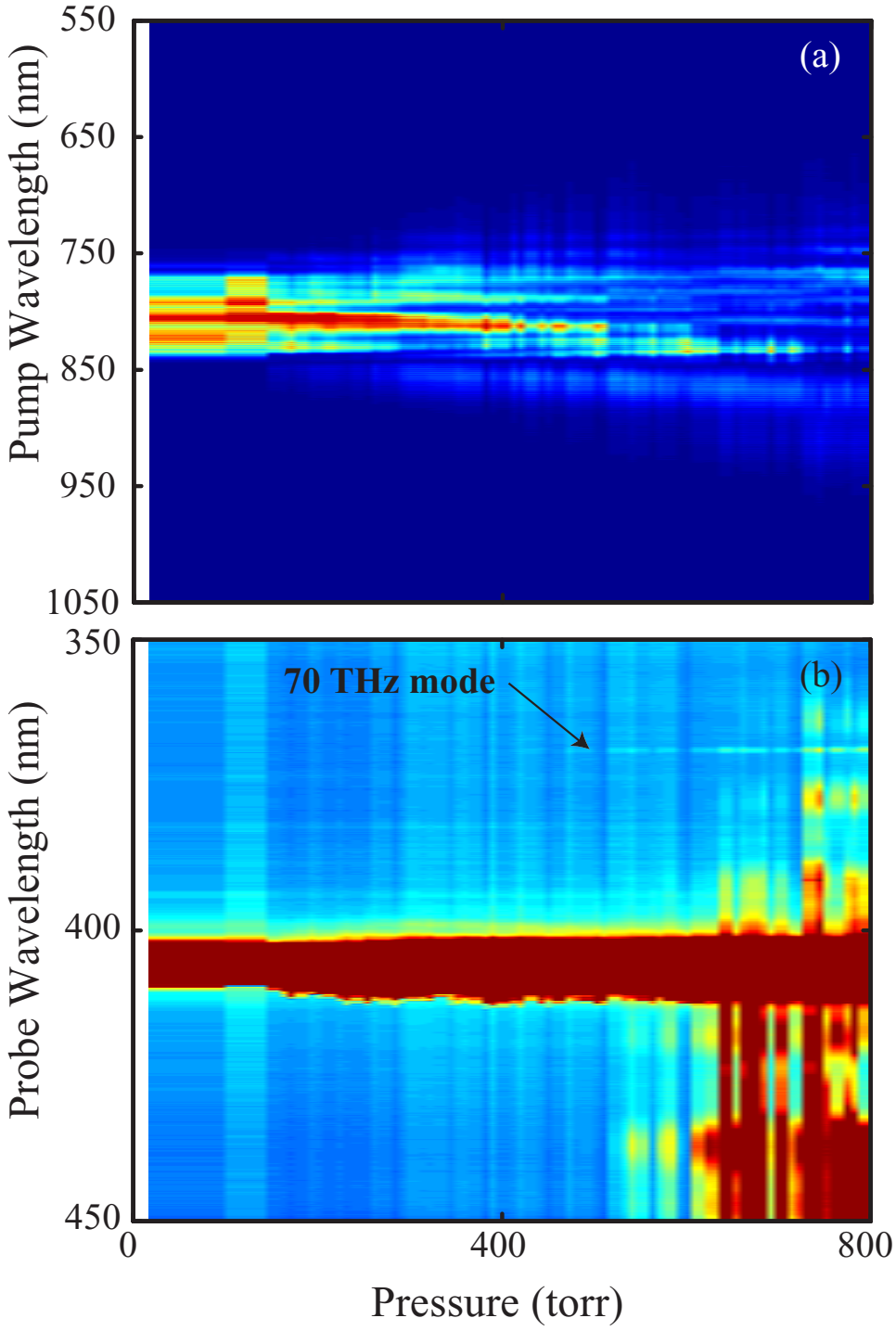

Figure 4.22: The measured spectrum of the pump pulse (a) and the probe pulse (b) as Nitrogen pressure is increased in the hollow core fiber.

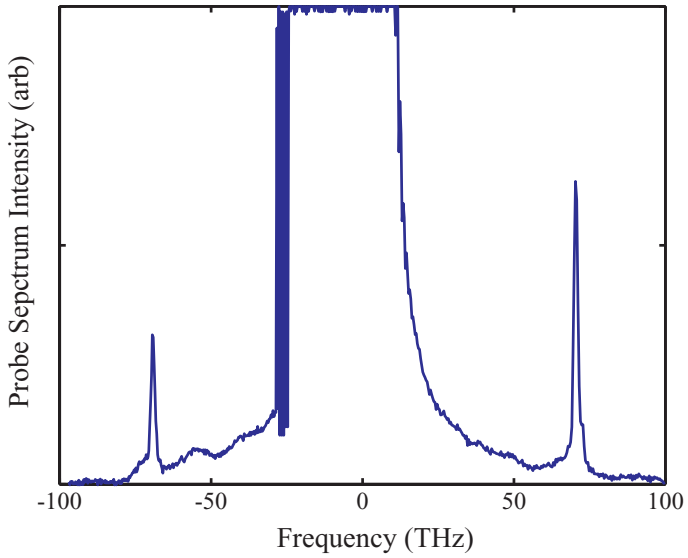

Figure 4.23: Probe spectrum demonstrating excitation of the 14 fs vibrational mode in N_2.

4.8.2 Excitation of self-seeded vibrational motion in N_2

The vibrational period of N_2 is 14 fs, and is normally inaccessible for ISRS excitation to a pump pulse with a 20 fs duration. However, the spectrum of the pump pulse can be increased with propagation in a gas as a result of the Kerr-induced temporal phase modulation experienced by the pulse. In a non-dispersive medium, the pump pulse intensity profile is unmodified as the bandwidth increases. However, in the presence of dispersion, the pulse can acquire structure. If this medium is a molecular gas and the structure developed is shorter than the vibrational period of previously inaccessible vibrational modes, those modes will be weakly excited. However, with increased propagation, the reshaping of the pulse will become more dramatic, and the vibrational mode will be more heavily excited.

Figure 4.22(a) shows the spectrum of the pump pulse propagating though a hollow core fiber filled with N_2 gas as the gas pressure is increased. The probe spectrum

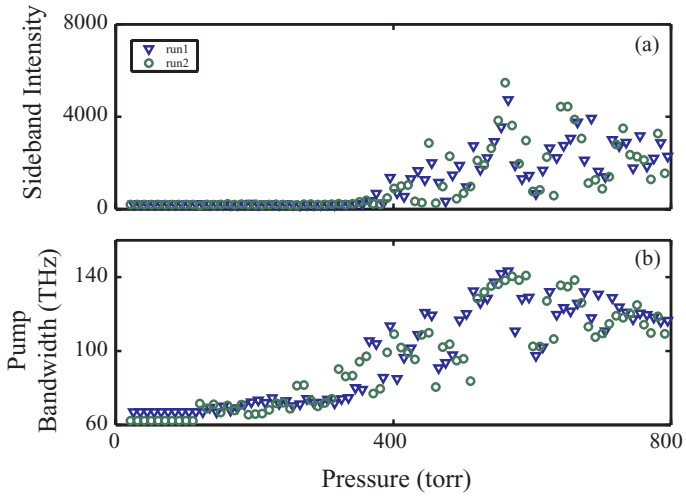

Figure 4.24: The variance of the probe bandwidth in Figure 4.22 (a) and the sideband intensity at the vibrational mode at 70 THz in Nitrogen in the probe spectrum (b).

is broadened due to self phase modulation (SPM). Notice that at a pressure of 400 torr, a sideband in the probe spectrum (Figure 4.22(b)) appears at 70 THz (see Figure 4.23), which indicates the excitation of the 14 fs (70 THz) N_2 vibrational. A closer inspection of Figure 4.22(a) also reveals that as the pressure is increased over 400 torr, there is a more substantial red-shift evident in th pump pulse.

Figure 4.24(a) shows this sideband intensity as a function of pressure. We see that the standard deviation of the spectral distribution (pump bandwidth shown in Figure 4.24(b)) increases continually. Notice that at 400 torr, we begin to observe light scattered to 70 THz from the probe central frequency, indicating there is a threshold pressure for the excitation of the N_2 vibrational motion. The reason for this threshold pressure is elucidated by Figure 4.25, which shows the correlation between the intensity of the sideband due to excitation of vibrational motion in N_2 and the pump spectral bandwidth. In Figure 4.25(b), I have rescaled the pump bandwidth

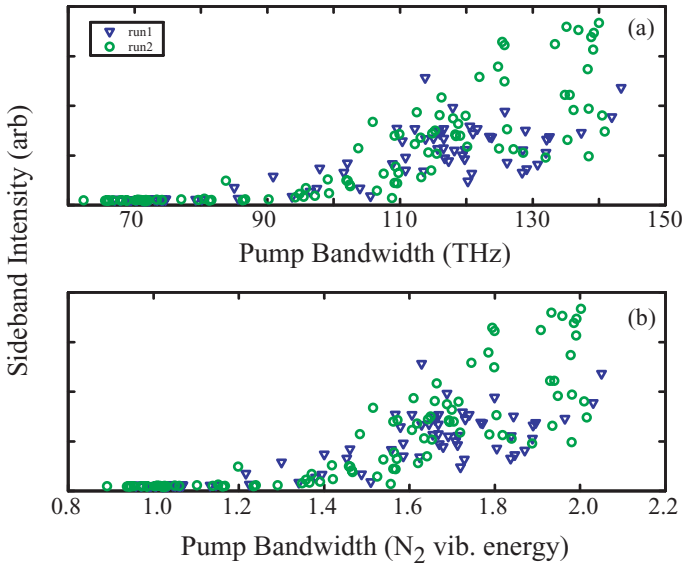

Figure 4.25: The correlation between sideband intensity of the 70 THz mode in Nitrogen and the probe bandwidth shows that once the probe bandwidth has exceeded 70 THz, the vibrational mode is excited.

in terms of the Raman frequency (70 THZ). This clearly shows that the "threshold" corresponds to the pressure where the bandwidth of the pump laser has increased to be as large as the vibrational frequency, which implies that upon compressed, the pump pulse duration would be shorter that the vibrational period. However, in the self-seeding approach, the bandwidth is created with SPM, and the dispersion and ISRS processes reshape the pump pulse to efficiently excite the vibrational mode. I am currently developing a model to test the validity of this explanation, however, the experimental evidence clearly shows that it is indeed possible to achieve ISRS excitation with a pump pulse longer than the vibrational period under the correct conditions.

4.9 Summary

To summarize, in this Chapter I demonstrate coherent and selective vibrational excitation of molecular gases at room temperatures and high densities. A learning algorithm incorporating a cost function is used to achieve control and demonstrating the ability to create "custom" multimode vibrational wave packets in molecular systems at STP, yielding a simple interpretation of the control mechanism in terms of impulsive Raman scattering. Significant fractions of the molecular samples were excited. Furthermore, significant vibrational amplitude is achieved as evidenced by strong overtone excitation. In addition to creating shaped molecular wave packets, we measure and observe dynamics using temporally resolved nonlinear spectroscopy. These techniques are general and can be applied to many transparent molecular gases, or liquids with high vapor pressures at room temperature. The results are encouraging for the prospect of using tailored laser pulses to provide selective excitations for influencing bimolecular reactions. We have seen preliminary evidence of controlling the reaction rate of a bimolecular reaction with a shaped laser pulse; however, more work is needed to unequivocally prove this result. In the future, since shaped pulses with durations of 5-10 fs are now becoming experimentally practical, it will be possible to extend this approach to all Raman active molecular modes, including H_2. Finally, we have also shown that Raman vibrational modes can be excited in spectrally broadened pulses that have not been time compressed, provided that the broadened pulse develops some structure with a time duration shorter than the vibrational period. Further propagation in the molecular gas will reshape the

pulse to more efficiently excite vibrational motion in that gas, thus self-seeding the process.

CHAPTER V

Applications of Controlled Atoms and Molecules

5.1 Introduction

The main point of controlling quantum mechanical systems, other than to learn about those systems, is to use control and use those systems in a beneficial way. In this chapter, I present two applications of the work I presented in the previous chapters. The first section of this chapter, we demonstrate that by creating rotational wave packets with a 20 fs ultrafast pulse, a time-delayed pulse can be spectrally broadened, then compressed after propagating through a transparent window. This experiment shows that we can use a quantum mechanical system that has been prepared in a desirable way to do something useful in the laboratory, essentially using light to control a quantum mechanical system that can be used to control another light pulse, with very important and wide-ranging applications.

The second application is the use of EUV radiation for coherent imaging. Imaging does not make use of the coherent control of the HHG process. The imaging work described here was done as a feasibility demonstration for time-resolved coherent imaging with EUV radiation. Because we require a high degree of coherence

for our imaging experiments, we did a series of experiments studying the spatial coherence properties of phase-matched HHG. These experiments demonstrate that the phase-matched HHG radiation generated in a hollow core fiber has the spatial characteristics of a high-quality laser beam, with essentially perfect spatial coherence. We also showed that we could obtain the frequency spectrum of our EUV light simply by a deconvolution of the interference pattern generated by a double-slit. This is to our knowledge the first application since Young's experiments 200 years ago [110].

5.2 Controlled rotational wave packets as phase modulators

Ultrashort pulses have a wide variety of applications in science and technology. For some applications such as high-harmonic generation, THz measurements, surface SHG generation, or time-resolved chemical reaction dynamics, very short optical pulses are desirable [111, 112, 113]. However, the bandwidth available directly from laser systems is limited. To circumvent these limitations, several techniques have been developed for broadening the spectrum of a light pulse. Typically, this creates a positively chirped pulse that can be compressed to a shorter pulse. Recent advances in the field of coherent control of atoms, molecules, and solid-state systems [67, 11, 13, 2, 5, 10] made possible a number of new techniques that can be used to manipulate light pulses. In this section, we describe a technique where use a rotational wave packet created by an ultrashort light pulse to induce a rapid phase modulation on a time-delayed probe pulse. This technique has distinct advantages over previous schemes of pulse compression because the phase-modulation can be independently controlled by the pulse that excites the rotational wave packet and

as a result, the modulated pulse can be time-compressed by propagation through a transparent window, eliminating the use of pulse compressors that suffer from high loss.

The most common pulse compression scheme is to use the electronic Kerr nonlinearity to produce a temporal self-phase modulation (SPM) that is proportional to the pulse intensity [114, 115, 116, 117]. The SPM process imparts a positive chirp on the pulse, which must then be compensated for by a diffraction grating or prism pulse compressor [118, 119]. Moreover, because SPM is a third-order nonlinear process, it is very sensitive to variations in the input pulse shape and energy and amplifies any instabilities in the input pulse. Nevertheless, this technique has been responsible for the generation of the shortest optical pulses to date, with a duration under 5 fs [116].

In recent years, however, several alternative approaches to the modulation of light have emerged. One method is to use intense quasi-CW lasers to excite a series of high-order vibrational Raman lines, producing a broad frequency spectrum that consists of a series of discrete lines [120]. In another technique, an ultrafast laser pulse excites a strong vibrational coherence in SF_6, also results in the generation of many high-order Raman sidebands [121]. Compressing the spectra from either technique produces a pulse train with narrow temporal structure (predicted to be sub-fs) given by the separation of the highest-order Stokes and anti-Stokes sidebands. Compression schemes based on rotational modulation of the index of refraction of a molecular gas have recently been proposed, predicting compression to 3 fs duration using rotationally-excited H_2 [122] and to $\sim$1 fs using N_2 [123].

In this work, which was a collaboration involving Tom Weinacht, Mark Baertschy, and myself, we demonstrate experimentally that rotational wave packet revivals [124] in a molecule (CO_2) can be used to phase-modulate and self-compress single, ultrashort, light pulses. A short pump pulse excites a rotational wave packet in the gas that undergoes periodic full revivals at time delays of $T_r = h/2B$, where h is Planck's constant and B is the rotational constant of the molecule. In the case of CO_2, full revivals occur at $T_r = 42.8$ ps. Because these revivals are separated by many ps (even though they contain rapid structure during each revival), the probe pulse experiences a non-periodic phase modulation allowing for single pulses to be generated that are phase modulated in a simple, controlled way. We also measured the phase induced by the time-dependent index of refraction during the rotational revival of a wave packet. Finally, we show that soliton-like pulses can be generated at arbitrary intensities using this scheme.

5.2.1 Theoretical description

The pump pulses used in this series of experiments are linearly polarized. When such a linearly polarized pulse interacts with a molecule that has an anisotropy in its polarizability, that molecule experiences a torque as it tries to align itself to the direction of the linearly polarized field, see Figure 4.9. This feature of molecules has been exploited for years as a mechanism for trapping. When excited by a short time duration pulse, these molecules experience a large, impulsive torque that excites a large number of rotational states and forms a quantum mechanical rotational wave packet.

Provided electronic excitations and rovibronic couplings are negligible, the rotational motion of the molecules can be described by a simple rigid rotor model [125, 126]. The total wave function Ψ will be expanded in terms of rotational eigenstates $|JM\rangle$ of the field-free Hamiltonian H_0, whose corresponding energy eigenvalues are $BJ(J+1)$, where J is the angular momentum quantum number and M is its laboratory frame z-axis projection. The interaction between the linearly polarized pump pulse and a linear molecule is through an induced electric dipole moment, describable in terms of the effective angular potential energy $V = -\left[\frac{\varepsilon^2(t)}{2}\right]\left(\alpha_{\|}\cos^2\theta + \alpha_{\perp}\sin^2\theta\right)$. Here $\varepsilon(t)$ is the electric field of the laser pump pulse, θ is the angle between the electric field and the internuclear axis, and $\alpha_{\|}, \alpha_{\perp}$ are the components of the anisotropic polarizability for fields respectively parallel and perpendicular to the axis. The full Hamiltonian for a rotating molecule interacting with the pump pulse is

$$H(t) = H_0 - \frac{1}{2}\varepsilon^2(t)\left(\Delta\alpha\cos^2\theta + \alpha_{\perp}\right), \tag{5.1}$$

where $\Delta\alpha = \alpha_{\|} - \alpha_{\perp}$.

A quantum system initially in a pure $|JM\rangle$ state will be excited by the pump pulse into a coherent superposition of different $|J'M\rangle$ states. Selection rules require that the $J' = J, J\pm2, J\pm4, \cdots$ have the same exchange symmetry as the initial J. After the pump pulse, the rotational wave packet evolves under the field-free Hamiltonian. There are exact, periodic, full wave packet revivals at a period of $T_r = h/2B$. In addition, due to the quadratic dependence of the energy on the rotational quantum number, partial revivals occur with a period $T_{partial} = \dfrac{h}{\mathrm{d}^2E(q)/\mathrm{d}q^2}$ [127], where q is a quantum number that must increase by unity.

Our detailed model begins with a thermally averaged ensemble of different pure $|JM\rangle$ states weighted according to the Boltzmann distribution function. Next, we propagate them in time through the duration of the pump pulse, using the time-dependent Schroedinger equation, with the Hamiltonian defined in Eq.(5.1). In the case of a symmetric, linear molecule, e.g. CO_2, only even J-values are included in the ensemble (i.e., $J = 2q$). The dephasing and rephasing of the quantum states induces a periodic modulation of the index of refraction of the gas, which is given by

$$n^2(t) \approx 1 + \frac{N}{\varepsilon_0}\left(\alpha_\perp + \Delta\alpha \left\langle \cos^2\theta(t)\right\rangle\right) \tag{5.2}$$

where N is the gas number density. The alignment cosine, $\langle\cos^2\theta(t)\rangle$, is the thermally averaged expectation value of $\cos^2\theta$. Figure 5.1 shows the calculated index of refraction as a function of time, for rotating CO_2 molecules at temperatures of 293 K and 195 K, excited by a 20 fs, 800 nm pump pulse at intensity $3x10^{13}W/cm^2$. At $t = 0$, the pump pulse creates the coherent rotational wave packet. The peaks in $n(t)$ that occur every $T_r \sim 42.8$ ps are due to the rotational revivals where the wave packets rephase completely. Partial rephasings occur at intervals of $T_{partial} = T_r/4 \sim 10.7$ ps. The partial rephasings at odd multiples of $T_{partial}$ would not exist if both even and odd J states were allowed, e.g, for a heteronuclear molecule. Note that in Figure 5.1, the molecular alignment is improved by cooling the molecular gas. Cooling increases the purity of the initial state, resulting in a more coherent alignment of the ensemble of molecules and therefore a larger variation in the index of refraction.

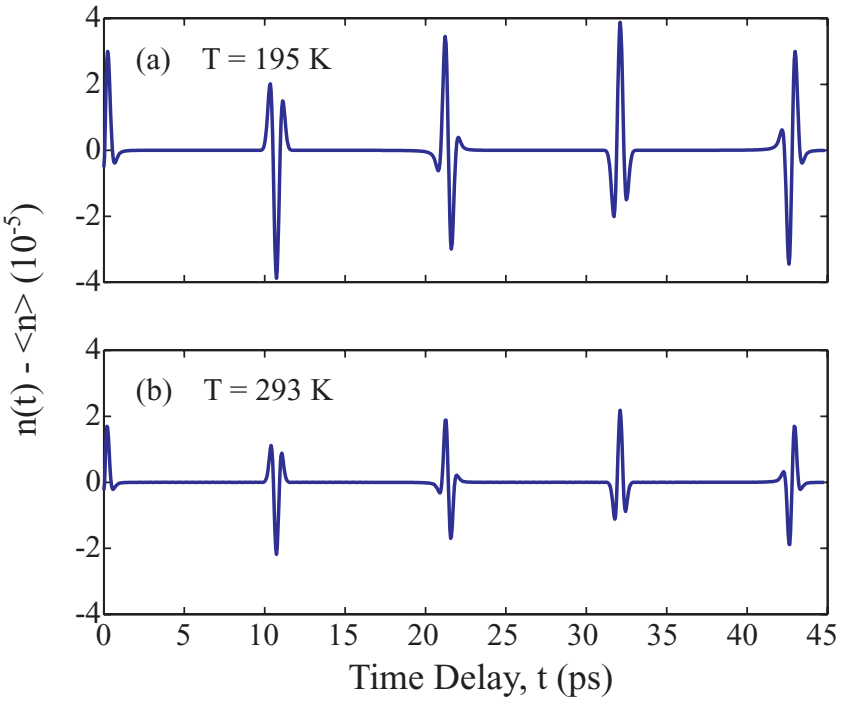

Figure 5.1: Calculated index of refraction, $n(t)$, as a function of time for rotating CO_2 molecules at 195 K (a) and room temperature [293 K] (b). The plots show deviations from the average value, $< n >$, where $< n > -1 = 2.6\text{x}10^{-4}$ for 195 K and $1.7\text{x}10^{-4}$ for 293 K.

5.2.2 Molecular phase modulation for pulse compression

The phase modulation imparted on the probe pulse is maximized when the delay coincides with a full or partial rotational wave packet revival. By adjusting the delay of the probe pulse to coincide with the minimum or maximum of the index of refraction, we sample a region of curvature that provides predominately either positive or negative quadratic temporal phase modulation. Furthermore, by adjusting the duration of the probe pulse to match the time separation of the inflection points of $n(t)$, we can maximize the total phase modulation. This is desirable for two reasons. First, by confining the pulse energy to that region of the phase modulation where the curvature is of the same sign (within the inflection points), we ensure that the chirp is always of the same sign. This results in a smooth spectral broadening of the pulse, ensuring a high-quality compressed pulse. In contrast, for SPM, the time-dependent refractive index $n(t)$ generated by the pulse intensity envelope has inflection points. These lead to identical frequencies being created in different temporal regions of the pulse. Interference between these frequencies leads to modulations in the spectrum of the broadened pulse, which makes temporal compression difficult.

The second reason for matching the probe pulse length to the width of the curved portion of the induced $n(t)$ is to maximize the resultant bandwidth. Using a probe whose length is matched to the rotational revival width will result in more spectral broadening than for a shorter probe pulse. This result is seen by considering a simple expression that predicts the broadening induced on Gaussian pulses that experience

a quadratic temporal phase modulation (or linear chirp)

$$f = \sqrt{1 + \left(\frac{\pi c_R \tau_i^2}{2 \ln 2}\right)^2}$$

[128]. Here τ_i is the input pulse duration and the curvature of the temporal phase, $\varphi(t) = \omega_L t + \pi c_R t^2$, defines the chirp rate c_R. The output pulse duration is $\tau_o = \tau_i / f$ and follows a $1/\tau_i$ dependence. Therefore, increasing the input probe pulse duration can yield shorter output pulses until the probe pulse length exceeds the region of curvature in $n(t)$. Group velocity walkoff between the pump and probe pulses could cause the probe to shift in time with respect to the rotational revivals into a region of opposite chirp, but it is negligible in our case ($\sim$0.56 fs/cm).

For our experiments, we used 15-20 fs laser pulses generated by an amplified Ti:sapphire laser system, at a 1 kHz repetition rate, a wavelength of 800 nm, and an energy of $\sim$1 mJ [129, 69]. A portion of the pump pulse ($\sim$ 30 %) is split off for use as a probe pulse. This probe pulse is frequency doubled in either a long (25 mm KDP) nonlinear crystal to generate a long probe pulse ($\approx$ 0.6 nm, 270 fs, 400 nm) or in a short (2.5 mm KDP) crystal to generate a short probe pulse ($\approx$ 2.2 nm, 52 fs, 400 nm). The pump and probe pulses are combined with an adjustable delay and focused into a 30-60 cm long, 450 μm diameter, hollow-core fiber filled with CO_2 gas at pressures of 100-500 torr. For our first experiment, a rotational coherence was prepared using a 0.3 mJ, 20 fs, 800 nm pump pulse propagating through 280 torr of room temperature CO_2 gas in a 30 cm, 450 micron, hollow-core fiber. Using the short probe pulse to sample the instantaneous index variation, we measured the frequency shift (proportional to dn/dt) of the temporal phase modulation due to the

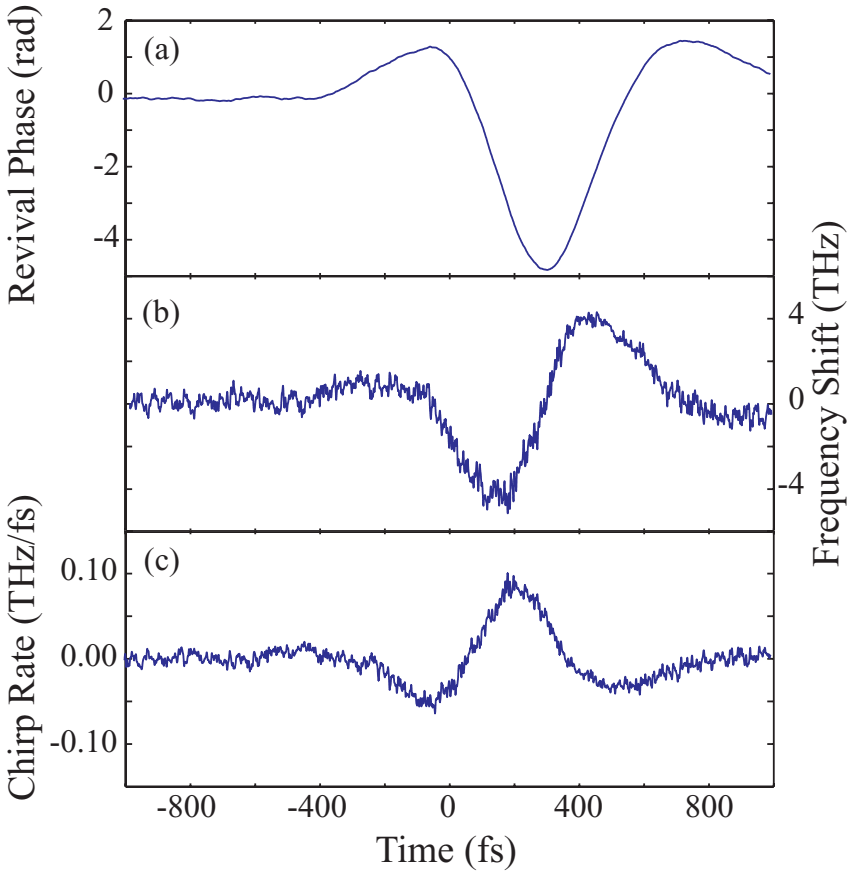

Figure 5.2: Measured phase (a), frequency shift (b), and chirp rate (c) for the first observable partial rotational revival.

1st observed partial rotational revival, as shown in Figure 5.2(b). These results can be integrated to obtain the phase $\varphi(t) = \frac{n(t)\omega_0}{c}L$ [Figure 5.2(a)], while the chirp rate can be obtained by differentiation [Figure 5.2(c)]. The probe pulse spectrum was measured as a function of delay in the vicinity of the 1^{st} observed partial rotational revival. As expected, for a 52 fs probe pulse very little broadening results from the peak chirp rate of ∼0.10 THz/fs, corresponding to $f \sim 1.17$.

5.2.3 Demonstration of self-compression of ultrafast optical pulses

We then repeated the experiment with a longer probe pulse of duration 270 fs, generated by doubling in a 25 mm thick KDP crystal. Here we used a 60 cm long

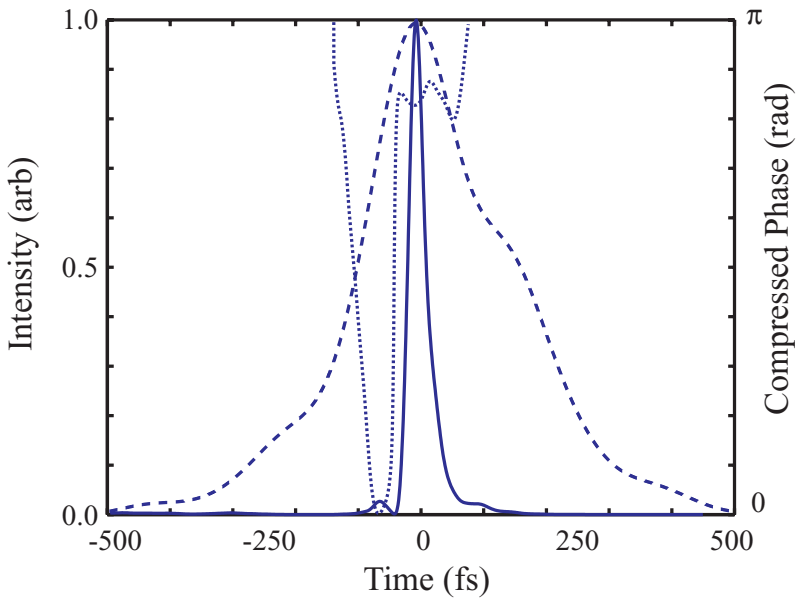

Figure 5.3: Temporal profiles of the injected 270 fs pulse (dashed) and the self-compressed 30 fs pulse (solid) and phase (dotted).

fiber filled with 300 torr of CO_2 gas. The probe delay was adjusted to coincide with the 1st full rotational revival to give the maximum output bandwidth in a region of negative chirp. The input pulse shown in Figure 5.3 (dashed line), has a minimum pulse duration of 270 fs as determined by the Fourier transform of the probe spectrum. The output probe pulse was characterized using self-diffraction, frequency-resolved optical gating (SD FROG). A 1" length of fused silica glass was inserted into the beam before the SD FROG measurement apparatus to compress the pulse. The deconvolved pulse shape and phase, shown in Figure 5.3 (solid and dotted lines, respectively), indicates that the pulse duration has been reduced to 30 fs, corresponding to a compression ratio of 9. This compression is achieved without the use of gratings, prisms, or chirped mirrors, so the efficiency is limited only by coupling into a hollow core fiber.

This approach to molecular modulation of light has several desirable characteristics. First, it allows for some tunability of the compressed pulses by shifting the delay of the probe pulse to a region of either positive or negative slope of the wave packet revival. Second, it can impart either a positive or negative chirp on the pulse. Third, since the phase modulation imparted by the molecular rotations is independent of the intensity of the probe pulse, spectral broadening is stable. Fourth, since a separate pulse prepares the rotational wave packet, this technique offers the potential for some control over the phase modulation [130, 131, 132]. Fifth, this process can lead to the generation of extremely short light pulses, possibly as short as 1fs [123]. Sixth, this technique works best for long pulses that are relatively easy to produce, generating shorter output pulses when the duration of the probe pulses matches that of the rotational revival. Seventh, under some conditions, the time dependent phase modulation of the rotational revival will balance the dispersion of the gas and will therefore support soliton-like propagation that is independent of pulse energy, i.e., the pulse is co-propagating with an index "bubble" caused by molecular alignment. Finally, and perhaps most importantly, this technique is very general and should allow for self-compression of light over the entire transparency range of the molecular gas, spanning from the IR into the UV region of the spectrum. This is particularly important in the UV, where the higher index of refraction may make this technique more effective, and where other pulse compression techniques suffer either from high-order dispersion or high loss.

5.2.4 Improving the pulse compression

Further improvements such as lengthening the fiber, increasing its diameter, increasing the gas pressure, cooling the molecular gas, using a more intense pump pulse, and using a molecule with a larger difference in polarizabilities, will yield even shorter, higher power, shaped pulses. By choosing a different molecule, we can adjust the time scale of the width of the rotational revivals to optimize for different input pulse durations. Lastly, our model predicts that shaping the spectral phase of the pump pulse can modify the structure of the revival. This presents the possibility of tailoring the wave packet to pre-compensate for high-order spectral phase aberrations in the compression window. Unlike techniques involving the excitation of a single vibrational or rotational level, this is possible in a wave packet because the relative phases of many rotational levels can be adjusted so that they rephase in an optimal way. If the modulation of the revival structure is strong enough, this technique could be used as a programmable molecular phase modulator operating with bandwidths exceeding 50 THz.

As mentioned above, it is extremely difficult to compress pulses to sub-100 fs duration in the deep-UV. This is mainly due to the absence of very-broad bandwidth optical gain media at short wavelengths Furthermore the conventional SPM technique is difficult since gratings suffer from high loss and prism materials introduce large amounts of high-order spectral dispersion. The rotational compression technique is, however, ideally suited to this wavelength range. This is in large part because of the counter-intuitive finding that it is easier to compress a long pulse to sub-5 fs

duration, than to start with a shorter pulse, because the longer pulse experiences more time-dependent phase modulation. Furthermore, the compression only requires the pulse to be propagated through a transparent window for time compression, for which Flouride salts are ideally suited.

To determine if compression to a short pulse was feasible in the UV, we simulated the pulse compression process by using the time-dependent index of refraction to phase modulate a 100 fs pulse centered at 248 nm (e.g., from a KrF laser). We utilize the split-step technique, which is the standard approach for computing the effects of SPM in dispersive media [133]. In this approach, the dispersion of the medium is calculated in the frequency domain, while the phase modulation is applied in the time domain. The length of the fiber is split into small steps so that the change imposed on the propagating pulse is small for any given step and simulates both effects occurring simultaneously. After propagating the pulse with the split-step method, the pulse was propagated through a 1 mm thick window of LiF to time-compress the pulse.

To perform the split-step calculation, the fiber length L_f was split into N_L segments, where each slice is denoted as dz. The spectral phase response of a "fiber slice" due to the CO_2 gas was calculated from the relation, $\phi(\omega) = \frac{n(\omega)\omega_0}{c}dz$, where c is the vacuum speed of light, ω_0 is the central frequency of the field, and $n(\omega)$ is the dispersion relationship given by the expression [134]

$$n - 1 = 0.012055\left[\frac{5.79925\lambda^2}{166.0196\lambda^2-1} + \frac{0.12005\lambda^2}{79.609\lambda^2-1} + \frac{0.0053334\lambda^2}{56.3064\lambda^2-1} + \frac{0.0043244\lambda^2}{46.0196\lambda^2-1} + \frac{0.000121845\lambda^2}{10.0584738\lambda^2-1}\right]$$

Whereas the temporal phase was calculated from the relation $\phi(t) = \frac{n(t)\omega_0}{c}dz$, where $n(t)$ is obtained from the theoretical model and is shown in Figure 5.1.

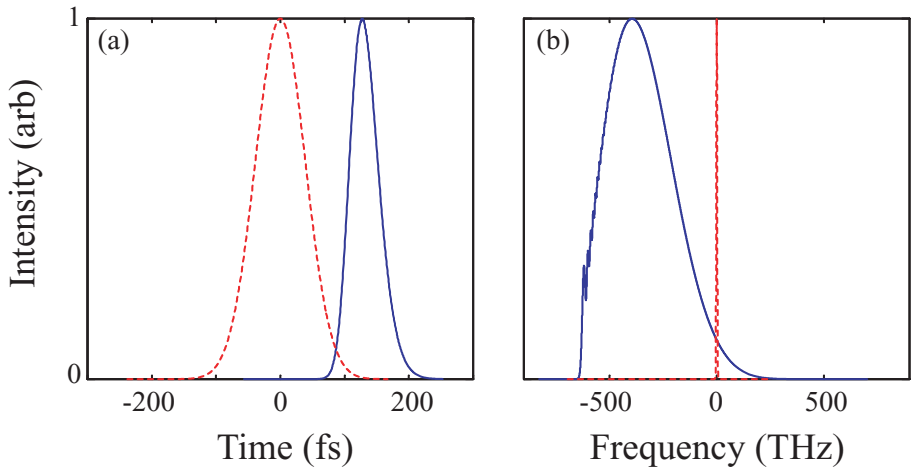

Figure 5.4: Intensity distribution of the input (dashed) and output (solid) pulses in both the temporal (a) and spectral (b) domains for the simulated pulse compression of a 100 fs, 248 nm, KrF laser pulse.

Once temporal and spectral phase quantities have been computed, the input field $E_{in}(t)$ is computed (see Figure 5.4). For this calculation, an input pulse duration of 100 fs FWHM center at a wavelength of 248 nm (KrF) was assumed. The fiber length in this simulation was 1 m and for the purposes of the calculation, it was broken into 500 step corresponding to a fiber slice, dz, of 2 mm. Figure 5.5 shows the evolution of the pulse spectrum as it propagates along the fiber. Note that in the output pulse shown as the solid line in Figure 5.4(a) is time-shifted with respect to the input pulse. This shift is due to the mismatch in the group velocity between the pump pulse that excites the rotational coherence and pulse to be compressed. The walkoff caused by the group velocity mismatch causes the pulse to move to a region of time-dependent index where there is a non-zero slope, leading to the frequency shift evident in Figures 5.4(b) & 5.5.

Once broadened, the pulse must be compressed. To do this, we simulate propagation through a 1 mm LiF window. The dispersion of LiF is given by the expres-

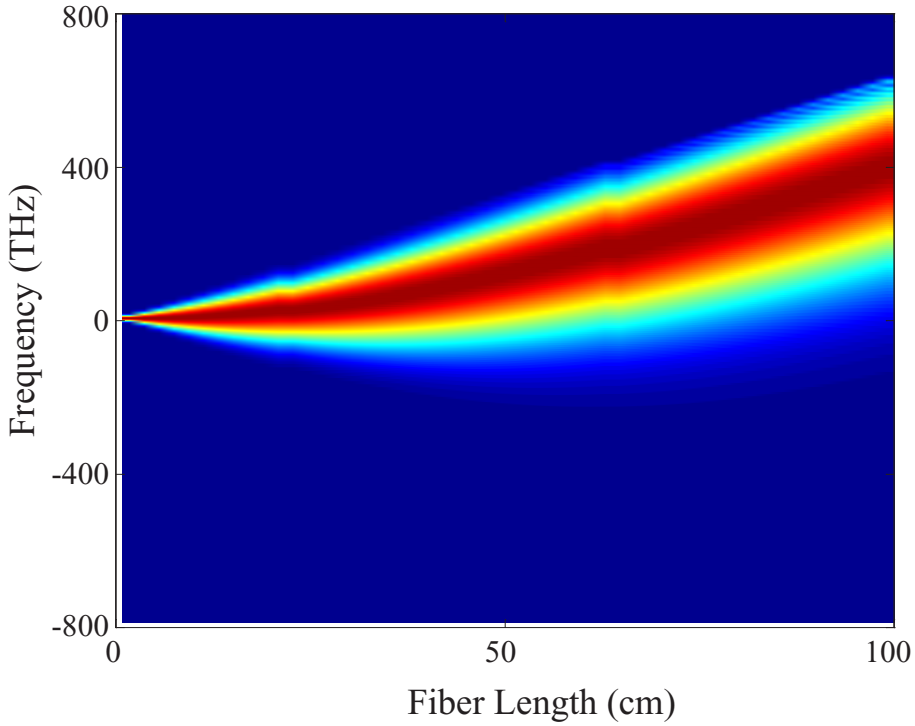

Figure 5.5: Normalized spectrum of the compressed pulse as it propagates in the fiber.

sion [135]

$$n^2 - 1 = \frac{0.92549\lambda^2}{\lambda^2 - (0.07376)^2} + \frac{6.96747\lambda^2}{\lambda^2 - (32.79)^2}$$

The pulse obtained after compression by the 1 mm LiF window has been compressed to a duration of 2 fs FWHM, as illustrated in Figure 5.6(a). If the entire bandwidth of the broadened pulser were to be time-compressed, it would yield a 1 fs FWHM duration light pulse as shown in Figure 5.6(b). Our models have shown that by reshaping the pump pulse that excites the rotational coherence, it may be possible to remove higher-order spectral phase from the compressed pulse, resulting in 1 fs pulses in the deep-UV.

In the demonstration experiment, the coupling of the blue probe pulse was not optimal, and as a result only a fraction of the energy of the pulse was phase-modulated.

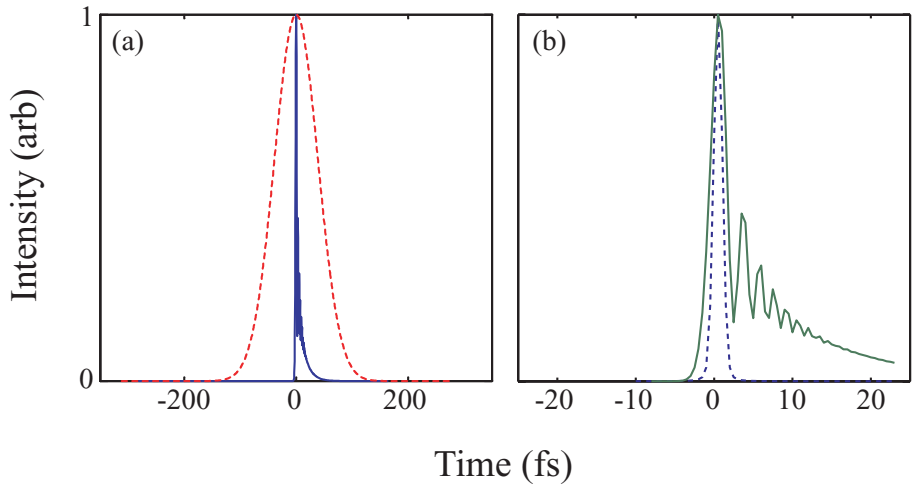

Figure 5.6: Input (dashed) and self-compressed (solid) pulses (a), along with the transform-limited (dashed) and self-compressed (solid) pulses (b) for simulated KrF pulse compression.

Furthermore, CO_2 is a difficult molecule to align, resulting in low levels of alignment, and thereby weaker phase modulation. Another limitation of this technique with the current setup is that the group-velocity walkoff limits the effective distance over which the rotational phase modulation will result in broadening to a smooth spectrum. In order to optimize this experiment, the group velocity of the pump and the probe pulses should be matched with an appropriate choice of both fiber diameter and gas pressure. A gas that can be more easily aligned (e.g., CS_2) should be attempted so that the phase modulation will be more effective. And finally, the molecular gas (or vapor) can be cooled to improve the alignment as well. Implementing this combination of improvements should lead to dramatic improvements in this technique and make available sub-5 fs laser pulses across the spectral range from the near-IR to the deep-UV.

5.2.5 Summary

In summary, we present a first measurement of the phase induced by a rotational wave packet revival and demonstrate its use for phase modulation and self-compression of an ultrashort pulse. We also demonstrate the possibility of novel, energy-independent, soliton-like propagation. This scheme is relatively insensitive to the input wavelength and provides a method for self-compression in spectral regions where traditional techniques are not efficient. We expect this technique will also provide a convenient and flexible tool to manipulate and shape pulses in a wide spectral range for a wide variety of experiments.

5.3 Spatial coherence of HHG radiation

5.3.1 Introduction

One of the fundamental properties the laser is the ability produce spatially coherent beams, that can focus to a very small spot size (on the order of the wavelength of the light). To date, the generation of fully-coherent beams has been limited to the visible/ultraviolet and longer-wavelength regions of the spectrum. A properly-designed optical resonator will allow only a single transverse "mode" to oscillate within it, allowing for efficient extraction of light in a single, "TEM_{00}" mode. Although any light can be made fully spatially-coherent by passing it through a small-enough aperture, this comes at a (usually very large) expense of beam energy. It is currently not possible to make practical optical resonators at short wavelengths because of the poor reflectivity of mirrors in the extreme-ultraviolet. Short-wavelength light sources such as electron impact sources [136], synchrotron sources [137], x-ray lasers [138],

and free-electron lasers [139] all do not use resonators, and generate at-best partially-coherent light.

High harmonic generation (HHG) is a useful way of generating coherent light throughout the ultraviolet and extreme ultraviolet (EUV) regions of the spectrum. However, experiments to date have shown that the HHG radiation is only partially spatially coherent, and does not retain the full coherence of the fundamental driving beam [140, 141, 142]. In this section, we show that EUV radiation generated by phase-matched HHG in a hollow core fiber has nearly-perfect spatial coherence. Such an EUV source, with good beam quality and high spatial coherence, can be used for experiments in high-precision metrology, inspection of optical components for EUV lithography [143], for and for microscopy and holography with nanometer resolution. This source, with its short-wavelength and diffraction-limited output, represents the smallest inherent effective source-size of any light source yet created.

The high-harmonic generation process is driven by coherent light from a laser, and is itself a coherent process in that the atoms' nonlinear-optical response is fully deterministic. Thus, one might expect that the HHG process would generate fully-coherent light. However, measurements to date have shown that mechanisms such as plasma refraction, as well as a complex spatial and temporal phase of the generated light that results from the physics of the HHG process, limit the coherence of HHG-generated EUV light. The HHG process is unique as a coherent optical process in that high-harmonics are generated by atoms in the process of ionization - electrons ionized by the strong field created by an ultrashort laser can "recollide" with their

parent ion as they begin to oscillate in the laser field [80, 18]. This recollision results in the EUV emission where the wriggle energy of the electron in the light field is released as an EUV photon; however, it also dramatically and dynamically changes the index of refraction of the medium. This large, time-varying index has been identified as the reason why early experiments have measured only partial spatial coherence [140, 141, 142]. Degraded coherence also results from the fact that emission at any particular wavelength can result from many electron recollision trajectories, creating a complex and spatially-varying multimode wave front [141]. Ionization, and the subsequent recollision event, occurs twice each optical cycle as the electric field reaches its peak value; however, for a particular harmonic, two separate electron trajectories (corresponding to slightly differing ionization times within the optical cycle), generate the same photon energy [18, 97]. Moreover, for HHG excited by relatively long laser pulses, many different optical cycles contribute to a given harmonic order. All these effects can reduce the coherence of the source. Although the proper selection of experimental conditions — such as the position of the focus with relation to the position of the nonlinear medium — can mitigate these effects by optimizing phase-matching in the forward direction [142], these techniques do not appear to fully regain the coherence of the source.

In recent work, we have shown that the HHG process can be phase-matched over a long interaction region using a hollow core fiber [90, 91]. This geometry increases the conversion efficiency of light into the EUV by up to two orders of magnitude over what would be possible using similar pulse energies in a free-space focus

configuration. In this section, we show that this phase-matching over an extended region also dramatically improves both the beam mode quality and the spatial coherence, by phase-matching only the emission of individual atoms that contribute to a fully-coherent, forward-directed, beam. Additionally, we demonstrate that the power spectrum of a coherent EUV beam, consisting of four harmonic orders generated by high harmonic emission (HHG), can be measured by analyzing the far-field intensity distribution produced by a pinhole pair. Such a spectral measurement can be calibrated by a straightforward measurement of the geometry of the experiment, providing absolute wavelength and relative intensity information. This approach proves particularly useful in the EUV since wavelength calibration can be achieved to high accuracy using straightforward measurements, and that the only element that has a spectral response that must be separately calibrated is the CCD. This experiment is, to our knowledge, the first spectral measurement of a source at any wavelength by analyzing the pinhole pair interference pattern.

5.3.2 Analysis of a double-slit pattern

Although Young performed his original double slit experiment two hundred years ago [110], it continues to yield new insights into the properties of light sources. The interference pattern resulting from a double slit (or pinhole pair) is commonly used to measure the spatial coherence properties of a light source in the visible [144], as well as in the extreme ultraviolet (EUV) [145, 146] regions of the spectrum. This interference pattern results from the path difference of the incident light field from each slit to the observation point. In a standard spatial coherence measurement, the incident

field is assumed to be quasi-monochromatic, so that temporal coherence effects are isolated from a measurement of spatial coherence [147]. However, under conditions where a broad bandwidth source illuminates a pinhole pair, the interference pattern will contain both temporal and spatial coherence information of the source, as well as the power spectrum [148].

Our analysis is based on coherence theory [144, 147, 148, 149]. In the far-field, the path length difference between two sampled portions of a field [P1 and P2 in Figure 5.7] gives rise to an interference pattern, which is determined by the spatial and temporal coherence. This path difference also introduces a time delay $\tau = \dfrac{\Delta r}{c} = \dfrac{dx}{zc}$ that generates an autocorrelation, $\int E(t)E(\tau - t)dt$, of the incident field. The Wiener-Khinchin theorem shows that the power spectrum is the Fourier transform of the field autocorrelation [147]. Therefore, measuring the pinhole pair interference pattern is equivalent to measuring the power spectrum of the field incident on the pinhole pair — provided that the field is spatially coherent and the spatial extent of the field autocorrelation is less than the width of the Airy pattern from a single pinhole in the observation plane. This connection has been known for some time [148], but to date has not been exploited for a determination of the power spectrum of a light field.

The exact relationship between the interference pattern and power spectrum can be derived as follows. The intensity distribution in the observation plane after illuminating two pinholes equally can be written as

$$I(x) = 2I^{(0)}(x)\left[1 + \gamma_{12}(x)\cos\left(2\pi\frac{d}{\lambda_0 z}x\right)\right], \tag{5.3}$$

where $I^{(0)}(x)$ is the Airy distribution due to diffraction through a pinhole of width δ,

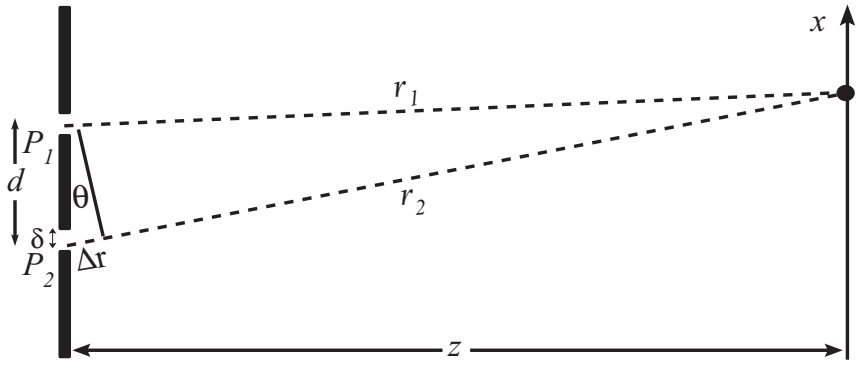

Figure 5.7: Experimental setup used to measure the spatial coherence and determine the power spectrum of the EUV beam.

d is the pinhole separation, z is the distance from the pinhole pair to the observation plane, λ_0 is the central wavelength of the light field, and γ_{12} is the degree of mutual coherence defined as the real envelope of the complex degree of mutual coherence ($\gamma_{12}(x) = \gamma_{12}(x)\exp\left(-i2\pi\frac{d}{\lambda_0 z}x\right)$). Here the time delay has been transformed to the spatial coordinate $x = \frac{zc\tau}{d}$. At any particular wavelength, the fringe visibility [147]

$$\mu_{12} = \frac{I_{\max}(x) - I_{\min}(x)}{I_{\max}(x) + I_{\min}(x)}$$

is simply the value of γ_{12} at $x = \tau = 0$, i.e., $\mu_{12} = \gamma_{12}(0)$. More generally [149],

$$\gamma_{12}(\tau) = \mathcal{F}^{-1}\left\{\widehat{S}(\nu)\mu_{12}(\nu)\right\}, \tag{5.4}$$

where $\widehat{S}(\nu)$ is the power spectrum normalized such that $\int_0^\infty \widehat{S}(\nu)d\nu = 1$. Eq. (5.3) shows that the interference pattern from a pinhole pair will have a broad spatial extent determined by the Airy distribution from a single pinhole. The modulations within the Airy disc are due to interference of the two pinholes. The slow modulations are due to the interference of the broad bandwidth associated with several harmonics, while the fast oscillations are determined by the central wavelength. The depth of

modulation is determined by the spatial coherence of the beam, and therefore this technique also applies to light fields with imperfect spatial coherence.

A Fourier transform of Eq. (5.3) is written as

$$\mathcal{F}\{I(x)\} \equiv F(f_x) = 2T(f_x) \otimes \left\{ \delta(f_x) + \frac{1}{2}\widehat{S}(f_x)\mu_{12}(f_x) \otimes [\delta(f_x + f_0) + \delta(f_x - f_0)] \right\}, \tag{5.5}$$

where $\otimes$ is the convolution operator, $T(f_x) = \mathcal{F}\left\{I^{(0)}(x)\right\}$ is a "dc" spike, $\delta(f_x)$ is the Dirac delta function, $f_0 = \dfrac{d}{z\lambda_0}$ is the carrier spatial frequency due to the pinhole-pair interference pattern, and $\widehat{S}(f_x)\mu_{12}(f_x) = \mathcal{F}\{\gamma_{12}(x)\}$. Thus, a Fourier transform of the interferogram produced from a Young's pinhole pair measurement should yield three terms — a dc term corresponding to a "spike" at zero (or dc) frequency and two terms containing information on the power spectrum convolved with the dc spike and weighted by the spatial coherence function at that frequency. As a result, the resolution of a spectral measurement is determined by the width of the dc spike. This resolution limit approximately corresponds to the number of interference fringes that can be resolved under the Airy distribution from a single pinhole, and is thus proportional to the diameter of the pinhole and inversely proportional to the pinhole separation. Equation 5.5 only yields information on the product of the power spectrum and the spatial coherence function at any frequency. However, in the case of high harmonic generation (HHG) generated in a hollow-core fiber [90], the 4-5 harmonics that emerge are phase-matched. As a result, we expect the spatial coherence $\mu_{12}(\nu)$ across the entire 4-harmonic spectrum to be very high and nearly constant. Recent spatial coherence measurements made under the same conditions and with

the same harmonics irradiating an aperture simultaneously confirm this assumption. Fringe visibilities of unity were observed over most of the beam [23], and for this pinhole separation, the average coherence as a function of wavelength $\int_0^\infty \widehat{S}(\nu)\mu_{12}(\nu)d\nu$ is $\sim$0.9, indicating that the average spectral deviation of the spatial coherence is $< 10^{-2}/nm$.

In the case of quasimonochromatic radiation and pinholes with negligible size, the modulation of spatial coherence factor, γ_{12}, is simply twice the height of one of the sideband terms after the maximum value of the dc spike has been normalized to unity. More generally, we can sum the integral of the sidebands and divide by the integral of the dc term, resulting in the following expression

$$\tilde{\mu}_{12} = \frac{\int T(\nu) \otimes \widehat{S}(\nu - \nu_0)\mu_{12}(\nu - \nu_0)\mathrm{d}\nu + \int T(\nu) \otimes \widehat{S}(\nu + \nu_0)\mu_{12}(\nu + \nu_0)\mathrm{d}\nu}{\int 2T(\nu)\mathrm{d}\nu}, \quad (5.6)$$

Note that this expression defines an average fringe visibility weighted by the spectral intensity ($\tilde{\mu}_{12} = \int \widehat{S}(\nu)\mu_{12}(\nu)\mathrm{d}\nu$) [144, 24]. For the case of monochromatic light, the spectrum is a delta function and the fringe visibility at the central frequency is obtained directly.

5.3.3 Determination of the spectrum

In this work, a 5 kHz, 1mJ, Ti:sapphire laser system [150] operating at a central wavelength of 760 nm, and with a pulse duration of 25 fs, was focused into a 10 cm long, 150 μm diameter, hollow core fiber filled with Argon gas. The EUV radiation is phase-matched at a pressure of 29 Torr in Ar. The pump pulse propagates predominantly in the EH_{11} mode of the hollow core fiber [151], while the high-harmonic generation is restricted to the central, most intense portion of the fundamental mode.

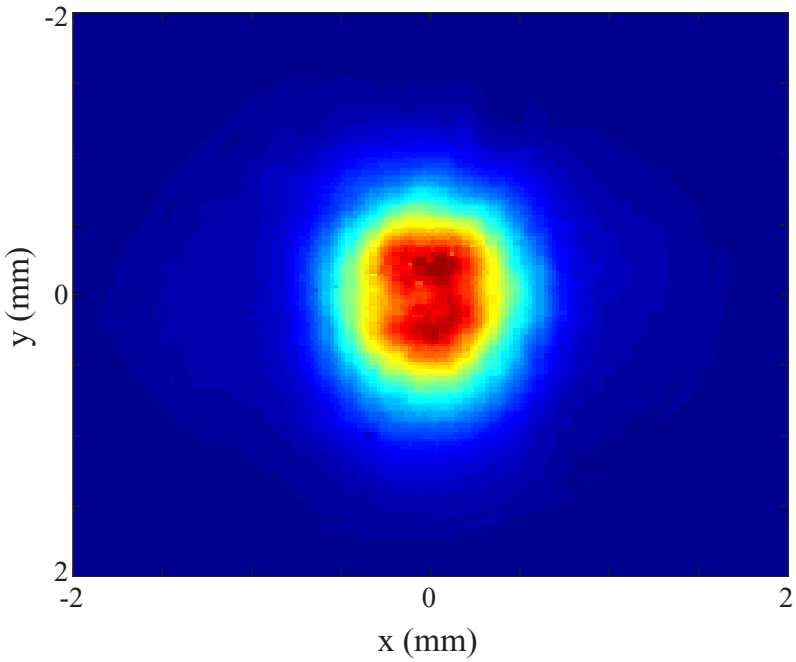

Figure 5.8: EUV beam measured with the Andor CCD camera place 95 cm from the exit of the fiber.

Figure 5.8 is an image of the EUV beam 95 cm after the exit of the hollow core fiber. At this propagation distance, the diameter of the EUV beam is ∼1 mm at the $1/e^2$ point, with a slight ellipticity (∼1.3) due to imperfections in the hollow-fiber shape, and with a beam divergence of < 1 mrad. A 0.35-μm thick Al filter is used to remove the fundamental IR beam, after which a 20 μm diameter pinhole pair with a 574.6 μm center-to-center separation (as verified by a scanning electron microscope) is placed 95 cm from the fiber exit.

The far-field diffraction pattern observed 2.85 m from the pinhole pair using an EUV sensitive CCD camera (Andor) with an exposure time of 60 seconds is shown in Figure 5.9(a). An additional 0.35-μm thick Al filter is placed immediately before the CCD camera to eliminate unwanted IR scattered light. The HHG spectra were also measured by an imaging EUV spectrometer (Hettrick Scientific HiREFS SXR-1.75),

which measures $\eta(\nu)\widehat{S}(\nu)$, where $\eta(\nu)$ is the relative efficiency of the spectrometer.

Figure 5.10 shows the spatial frequency distribution along the x-dimension obtained from a Fourier transform of the interferogram produced by the pinhole pair [shown in Figure 5.9]. The high quality of the data of Figure 5.10 is due in large part to the fact that the 2-D Fourier transform of the interferogram (with substantial random detector noise) implicitly averages over all 256 lines of data in the y-dimension. In essence, we take 256 simultaneous single-shot field autocorrelation traces; the interferogram averaged over all y is shown in Figure 5.9(b). The optical frequency axis is obtained by multiplying the spatial frequency axis by zc/d. Therefore, the pinhole diameter, separation, and the distance to the detector determine the calibration of the optical frequency axis in Figure 5.10. Each of these quantities can be determined to a very high accuracy. The three terms expected from Eq. (5.5) are clearly shown in Figure 5.10. The dc spike appears at the zero spatial frequency and has a fractional width of $\Delta\nu/\nu_0 = 0.022$, which agrees well with the predicted resolving power of $\Delta\nu/\nu_0 = 0.8\delta/d$, or 0.027 for our experimental geometry. The HHG spectrum appears as two sidebands well separated from the dc term. The harmonic peaks are broadened because of the intrinsic resolution of this measurement, i.e., we measure a convolution $T(\nu) \otimes \widehat{S}(\nu)\mu_{12}(\nu)$ or $T(\nu) \otimes \widehat{S}(\nu)$ assuming constant $\mu_{12}(\nu)$, as is the case for this experiment. The broadening is evident from the comparison of the spectrum measured by the x-ray spectrometer (dashed line of Figure 5.11) compared with the pinhole spectrum (solid line of Figure 5.11). However, the width of the spectrum obtained from the x-ray spectrometer after being convolved with the dc spike

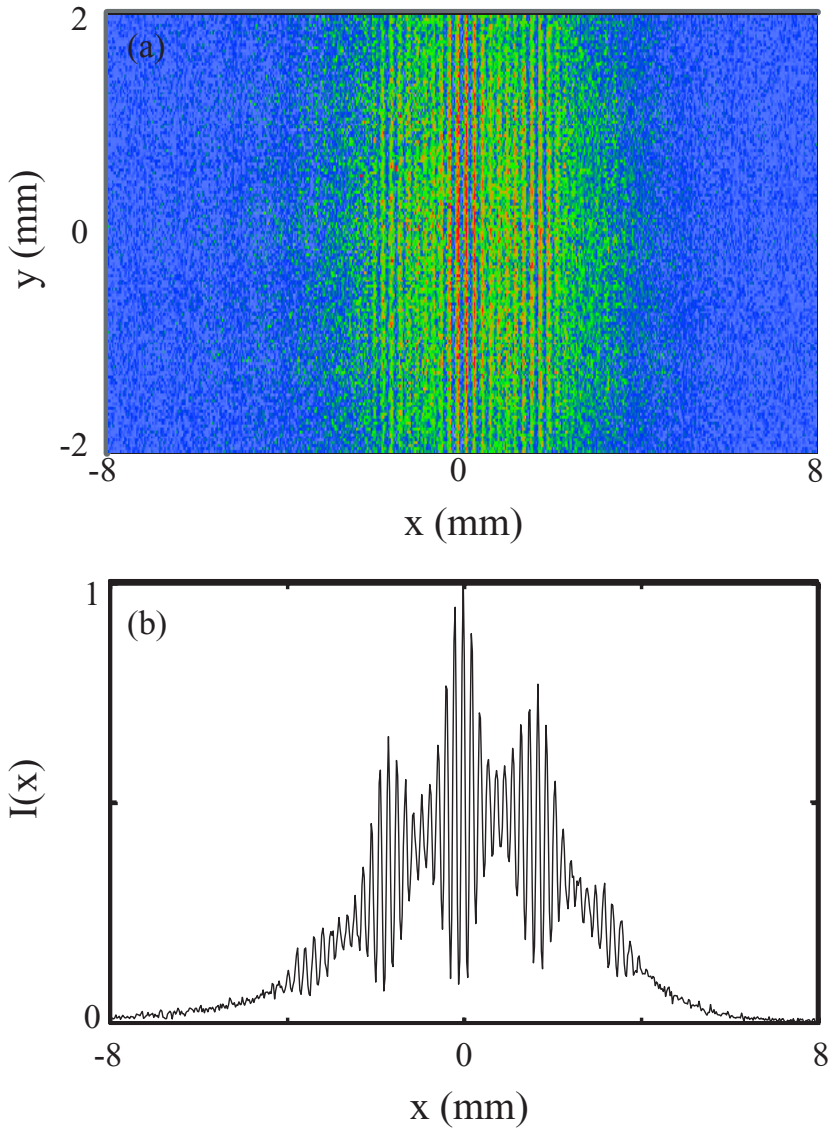

Figure 5.9: Interferogram used to determine the EUV beam power spectrum (a) and an average of the interferogram along the x direction (b).

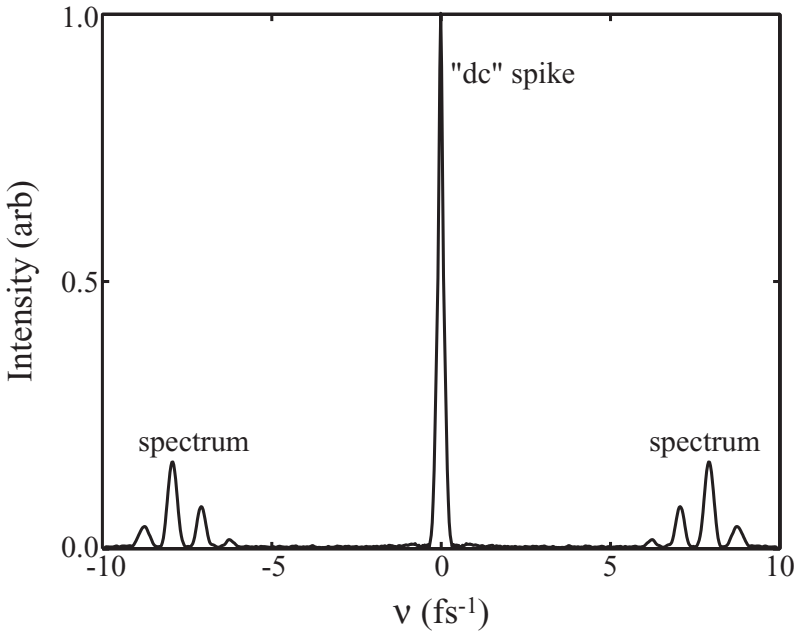

Figure 5.10: The spatial frequency distribution scaled in optical frequency showing the three terms form the Fourier transform of the interferogram.

is identical to that obtained from the pinhole pair. The difference in the intensity of the two spectra is due to the varying efficiency of spectrometer response, assuming constant spatial coherence across the harmonic spectrum, as explained above. The inset of Figure 5.11 plots the ratio of the two spectra $\frac{\widehat{S}(\nu)\eta(\nu)}{\widehat{S}(\nu)} = \eta(\nu)$.

5.3.4 Full spatial coherence of HHG

The spatial coherence of the EUV light was measured using the well-established double-pinhole (or double slit) interference technique [144]. The depth of modulation of the fringes generated after passing a beam through a pinhole pair depends on the correlation between the phase of the wavefront of the beam at the two points where it is sampled. If the phase difference between the two points is constant and deterministic (and therefore completely correlated), the fringe depth will be

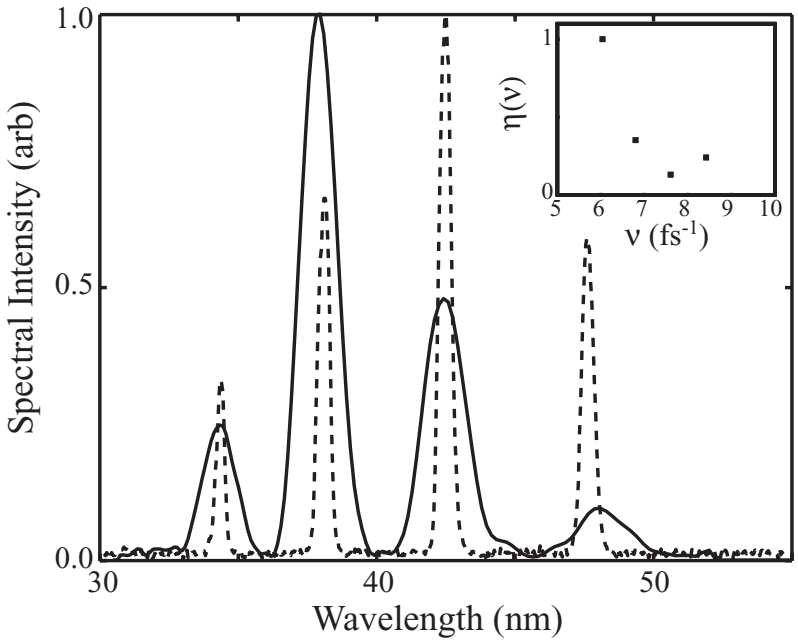

Figure 5.11: EUV spectrum obtained from a spectrometer (- -) and from the spatial coherence measurement (-). The inset shows the inferred efficiency of the spectrometer from this data.

unity. However, if there are random variations in the phase between the two points, the fringe contrast will be degraded due to implicit detector averaging. The fringe visibility was measured across the width of the EUV beam by sampling the beam with pinhole pairs separated by between 150 and 800 μm. We used apertures (National Aperture, Inc) fabricated with 20 or 50 μm diameter pinhole pairs, placed 95 cm from the exit of the fiber. The image distribution due to the pinhole pair diffraction was captured by a back-illuminated x-ray CCD camera (Andor Technology) placed 2.85 m from the pinhole pair. The integration time of the CCD camera ranged between 20 and 240 s (100,000 — 1,200,000 laser shots). The observation of high spatial coherence over such a long integration time indicates both high spatial coherence and long-term stability in beam phase.

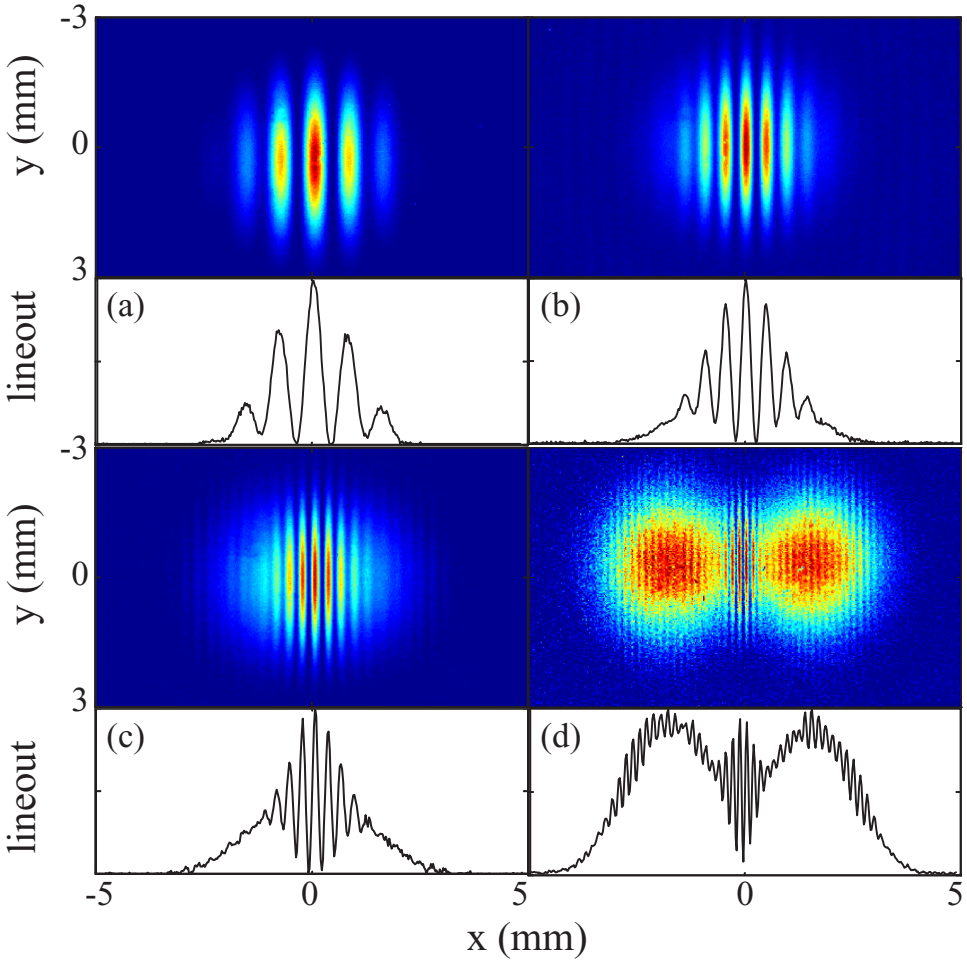

Figure 5.12: Interferogram and lineouts captured on a CCD camer for double-pinhole separations of 150 (a), 250 (b), 400 (c), and 800 (d) μm.

Figure 5.12 shows the measured diffraction pattern for a set of pinholes, together with a corresponding lineout. Note that the fringe visibility varies across the diffraction pattern. Normally, spatial coherence measurements are performed with quasi-monochromatic radiation. Under those conditions, the fringe visibility is constant over the entire interference pattern. When the incident radiation is broadband, consisting of several EUV harmonics, the depth of modulation at the center of the fringe pattern (equidistant from the two pinholes) gives the fringe visibility of the interference pattern. Analysis of the full modulation depth of the interference pattern over the entire field can yield information about the spectrum of the incident radiation [148, 24], as demonstrated in the previous section.

The EUV beam is sampled at 15, 25, 30, 40, 60, and 80 % of the beam diameter using pinhole pair separations of 150, 250, 300, 400, 575, and 800 μm respectively (as verified by an SEM). A sample set of data measured by our x-ray CCD camera is shown in Figure 5.12. In all cases, the interferograms were recorded in the far field. Under these conditions, analysis using Eqn. (5.5) is valid — we simply make a Fourier transform of the data, identify the sidebands, and integrate to obtain the average spatial coherence. Notice that Figure 5.12(d), showing the interference pattern produced by a pinhole pair at a separation of 800 μm, contains two circular Airy distribution patterns with fringes across it. The two Airy distributions are separated by $\sim$3.2 mm, even though this is the diffraction pattern generated by a pinhole pair at a separation of 800 μm. The increased separation is due to the fact that the pinholes are sampling the curvature of the EUV phase front, since the

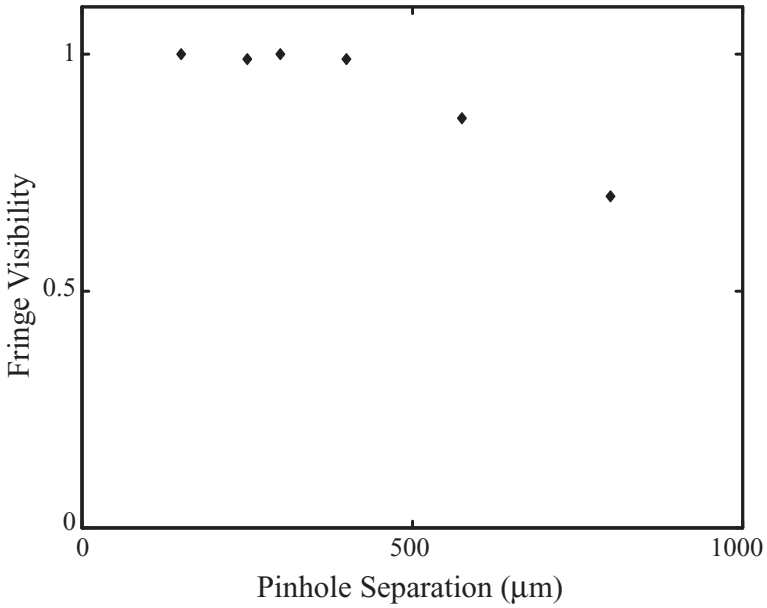

Figure 5.13: Fringe visibility across the beam.

pinhole separation (800 μm) is comparable to the beam diameter (1mm). At the location of the pinholes on the beam, the local tilt of the EUV wavefront is larger than the divergence due to the diffraction. Under these conditions, the two Airy distributions are not well overlapped. In this case, Eqn. (5.3) does not apply, and the fringe visibility varies due to the different intensities from each pinhole. In the central region where the two Airy patterns have approximately equal intensities, highest fringe visibility is observed, and corresponds to the correct measure of γ_{12}. Figure 5.13 shows the magnitude of the complex coherence function as a function of pinhole separation. It is evident from this plot that we maintain near unity spatial coherence over the majority of the EUV beam. At the larger pinhole separations, the EUV flux on the CCD detector degrades quite significantly making the error bars at the extremes quite large.

5.3.5 Summary

In summary, phase-matched EUV light generated in a fiber using the process of high-harmonic generation exhibits the highest inherent spatial coherence yet demonstrated. Since this source exhibits full spatial coherence at very short wavelength, it also possesses the smallest inherent effective source-size of any light source in existence. Coupled with previous measurements that demonstrate that coherent control techniques can be applied to obtain nearly-full temporal coherence from these sources [11, 12, 13], this means that fully spatially and temporally coherent laser-like beams of EUV light can now be generated. We also experimentally demonstrated a robust and accurate technique that allows the absolute wavelength and spectrum of a light field to be determined from the far-field interferogram produced by a pinhole pair. Furthermore, this technique provides a convenient method of absolute calibration in the EUV region of the spectrum where few tunable sources currently exist. The spectrum obtained is verified with the spectrum measured by a conventional grating spectrometer. The resolution of pinhole pair spectrum can be improved by a simple change in geometry — by either shrinking the pinhole diameter or increasing the pinhole separation, at the cost of reduced photon flux. The quality of the data is extremely high due to the implicit averaging of the 2-D Fourier transform. This experiment provides verification of an important link between the spatial coherence properties of an optical field and its power spectrum. Furthermore, because HHG is generated using a table-top setup, this EUV source will be particularly useful for a variety of application including nanoscale probes and imaging, and for precision metrol-

ogy of EUV optical components for the next generation of optical lithography, as well as for applications that take advantage of the sub-10 femtosecond time-duration of these pulses such as time-resolved photoelectron spectroscopy [152, 153, 154].

5.4 EUV Gabor holography with HHG radiation

5.4.1 EUV Microscopy with HHG radiation

Soft x-ray and EUV radiation is an important technology for microscopy. The fundamental reason EUV microscopy has been pursued is to take advantage of the superior resolution that can be obtained using short-wavelength radiation. Work at national facilities, such as Brookhaven National Laboratory and Lawrence Berkeley Laboratory, has resulted in dramatic improvements in soft x-ray microscopy, with the best images obtaining 45 nm resolution [155], and tomographic images that give 3-D information. However their use is restricted to a few large and well-funded facilities. HHG as a table-top source of EUV light has the capability of making possible soft x-ray microscopy in a small-scale laboratory setup.

Many optical microscopy techniques exist that use varying degrees of sophistication. To extract more information from the sample under study, a more complicated optical setup can be used. Alternatively, on can use a simple optical setup in combination with extensive signal processing. However, regardless of gthe technique, EUV microscopy is a difficult proposition. The EUV power in a HHG beam average power is limited to a few microwatts. EUV light can not use refractive optics, furthermore, because all materials scatter and absorb strongly in this wavelength regime. Moreover, EUV reflective optics are scarce and on-average exhibit a 70 % loss per bounce.

As a consequence, the preferred approach is to build as simple of an optical setup as possible, then use computer processing on the acquired image to extract information.

Our goal in this work is to construct an EUV imaging apparatus that allows for high-resolution microscopic images that can be processed at high speed. High-speed processing rules out using a photo-sensitive material (e.g., PMMA) to record the image, and restricts us to solid-state image acquisition devices. In this work, we utilize an x-ray CCD camera from Andor Scientific (HiREFS SRX1.75). This section describes the first coherent imaging experiment ever done with HHG radiation. This initial demonstration was done to test a basic imaging setup and study the resolution limitations.

5.4.2 Gabor holography

The simplest imaging experiment one can perform is to insert an object into a beam and capture the intensity distribution formed some distance away. This holographic imaging experiment, invented by Gabor in 1948 [156], is performed without the use of any optical components and requires both a recording and a reconstruction step. A Gabor hologram is recorded by simply placing an object in an optical beam, and therefore requires no critical alignment. The hologram is recorded by placing an object in a coherent beam of radiation as shown in Figure 5.14. The object will scatter some of the incident radiation, resulting in an object beam (u_o), and the remaining background radiation serves as a reference beam (u_r). The image and reference beam interfere in the recording medium, creating fringes that record both amplitude and phase information. Because we record the intensity, the sign of the

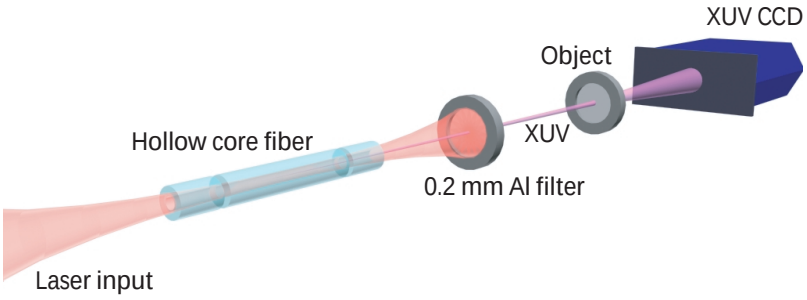

Figure 5.14: Experimental setup used for Gabor holography.

phase information is lost in the recording process, and the intensity distribution is given by

$$I = (u_r + u_o)(u_r^* + u_o^*) = |u_r|^2 + |u_o|^2 + u_r^* u_o + u_o^* u_r.$$

For a linear recording medium, the intensity distribution is faithfully represented in the hologram. The first two terms ($|u_r|^2 + |u_o|^2$) are due to a background image from the object and reference beams, the third term ($u_r^* u_o$) produces a real image, and the fourth term ($u_o^* u_r$) produces a conjugate image. The formation of this conjugate image is also referred to as the twin-image problem.

The hologram is reconstructed by diffracting radiation from the interferogram (either optically or numerically), and the original waveform (with both amplitude and phase information) is retrieved. The loss of sign information results in the largest noise source in the Gabor holography process because both a real and conjugate image are formed.

When a collimated reference beam is used to illuminate the object in Gabor holography, the image is formed without magnification. In our experiment, we have

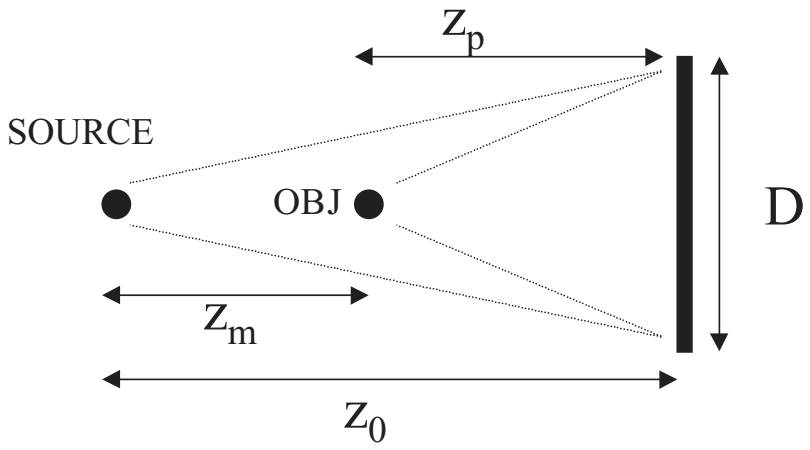

Figure 5.15: Diagram depicting Gabor holography geometry for illumination of the object with a spherical wave.

an uncollimated EUV beam with a ~ 1 mrad divergence. This can be approximated as a spherical reference beam as depicted in Figure 5.15. The magnification of the object during the recording phase is simply the geometric projection $M_c = \dfrac{z_p}{z_o - z_p} = \left(\dfrac{z_o}{z_p} - 1\right)^{-1}$.

5.4.3 Resolution of Gabor holography

Holography is a type of interference between a (presumably known) reference wave and an object wave that is to be recorded. A point object produces a series of concentric rings that is identical to a Fresnel zone plate lens (FZP) [157], which is an optical element that either blocks or rephrases the transverse distribution of an incident field so that it will act as a lens. It follows that the smallest object we can resolve depends on the properties of the lens that we can record. This depends on both the wavelength and coherence of the light used, as well as the resolution of the recording medium.

The Rayleigh resolution limit states that the distance to the first zero of the Airy distribution determines the minimum transverse separation, δ that can be resolved between two spots and is given by $\delta = \frac{1.22\lambda}{N.A.}$, where $N.A. = D/f$ is the numerical aperture of the FZP, $D = 2r_N$ is the FZP diameter, f is the focal length, and r_N is the radius of the outermost zone of the FZP. The focal length of a FZP can be approximated as $f \cong \frac{2r_N\delta_{r_N}}{\lambda}$ [158], where δ_{r_N} is the width of the outermost zone of the FZP. Thus, by combining the above equations, we arrive at the result $\delta \cong 1.22\delta_{r_N}$. The width of the smallest FZP zone we can record is twice the detector resolution. This tells us that the resolution of the Gabor holography process is limited by the smallest zone we can write, and is thus limited to the resolution of the detector. From this analysis, we see that the only way to use Gabor holography for high-resolution imaging is to use a high-resolution recording medium or to magnify the holographic image. The Andor CCD camera that we utilize for our experiments has a resolution of 26 μm, which severely restricts the resolution that can be obtained from our experimental setup.

5.4.4 Gabor hologram generated by HHG radiation

Although our CCD camera lacks the ability to record a high-resolution Gabor hologram, Gabor holography is still an excellent way to demonstrate the coherent imaging capabilities of our system. The experimental setup for this experiment is the same that was used in the previous section. However, instead of placing an opaque pinhole pair in the EUV beam, we used a 260 μm diameter wire as an object. The object was placed 95 cm away from the exit of the HHG fiber and the hologram

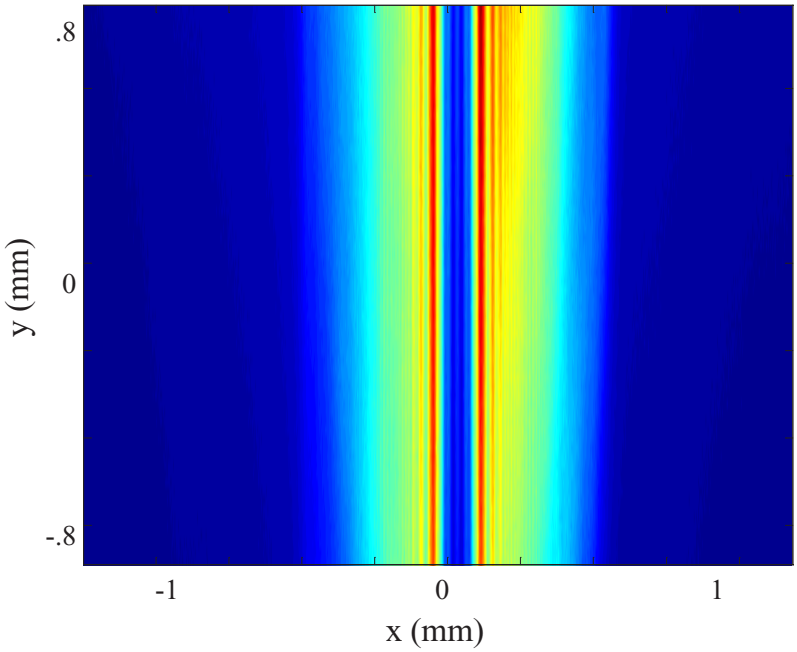

Figure 5.16: Hologram recorded with HHG radiation of a 260 μm diameter wire.

(Figure 5.16)was recorded on the Andor CCD camera 2.17 m away from the object.

The hologram shown in Figure 5.16 was reconstructed numerically by illuminating the recorded interferogram with a reconstruction wave and back-propagating to the object plane. In this reconstruction, the wave was assumed to be a plane wave, which is unity across the entire beam. Therefore, the reconstruction requires the back-propagation of the hologram to the object plane. In the Fresnel approximation, the propagated field is computed by convolving the field, $u(x)$ with the impulse response function of free space, $h(x) = \exp\left(-\frac{i\pi x^2}{\lambda z}\right)$. The convolution is easily computed as the product in the Fourier domain, $U \cdot H$. Therefore, to compute the reconstructed field, u_r, we simply Fourier transform the hologram, u_h, multiply by the Fresnel propagation kernel, then take the inverse Fourier transform, i.e., $u_r = FFT^{-1}\{FFT\{u\} \cdot H\}$. The information along the vertical direction of the hologram

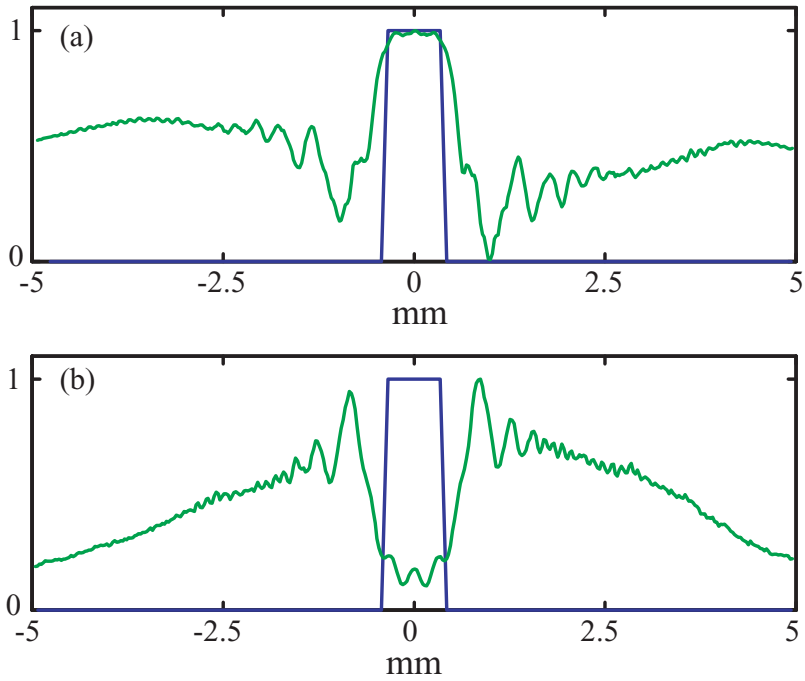

Figure 5.17: Numerical reconstruction (a) of a wire hologram (b).

is redundant, so this calculation was performed with a single lineout, and is shown in Figure 5.17(a), with the accompanying hologram lineout from Figure 5.16 shown in Figure 5.17(b).

The recording and reconstruction stages of this hologram were simulated to verify the reliability of our reconstruction algorithm. For the comparison, I numerically simulated a spherical wave with a 95 cm radius of curvature incident on a wire (i.e., with a transmittance of unity outside of a 260 μm width). The transmitted field was propagated in the manner described in the previous paragraph. The intensity of the forward-propagated field is the hologram and is shown in Figure 5.18(b) and compares well to the data shown in Figure reffig:recon(b). The simulated hologram was numerically reconstructed in the identical manner (Figure 5.18(a)) described above and the result compare well to the experimental results in Figure 5.17(a).

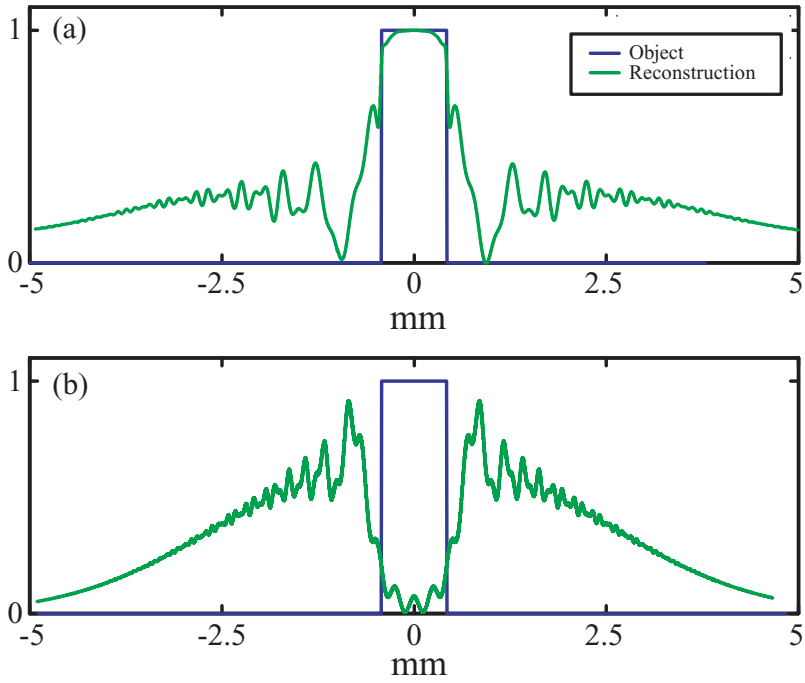

Figure 5.18: Numerical reconstruction (a) of a simulated wire hologram (b).

5.4.5 Summary

The proceeding section demonstrated that EUV light generated using HHG in a hollow-fiber phase-matched geometry produces a beam with full spatial coherence. The high beam quality and spatial coherence make this source an excellent tool for microscopy applications. This section demonstrates the recording and reconstruction of a Gabor hologram with this HHG radiation and demonstrates the use of this source for coherent imaging. The ultimate goal is to make use of the high resolution afforded by the short wavelength of this source, and to acquire and analyze data in real time. The latter requirement necessitates the use of a CCD camera and limits the recording resolution to micron scales. I have shown that the resolution of Gabor holography for such a setup is limited by the detector resolution, and thus this current setup fails to provide high-resolution microscopy. Furthermore, Gabor holography uses

the undiffracted portion of the incident beam as the reference wave. This limits the complexity of objects that may be studied with Gabor holographic imaging. If the object distribution is large and complex, the reference wave is destroyed and a quality image cannot be reconstructed. Future work will be needed to determine the best approach to obtaining high resolution microscopy images from the HHG light source.

CHAPTER VI

Summary

Controlling the dynamics of atoms and molecules gives us new abilities to manipulate matter. This work was enabled by new ultrafast laser technology and the lessoned learned by 30 years of attempts at using coherent light to control atoms and molecules. It has only been in recent years that very successful coherent control experiments have emerged. My work has demonstrated that very high-order nonlinear systems can not only be controlled, but that we can understand the control mechanisms involved. By selectively optimizing a single harmonic order in the HHG spectrum, the learning algorithm found an unexpected solution. This new solution taught us about a new phase-matching mechanism that occurs in extreme nonlinear optics. This demonstrates that a learning algorithm can non-only control a very high-order nonlinear system, but it can also teach us new science.

The work presented in this thesis is an initial contribution to what will, in my view, become a widely applied approach to the manipulation of matter. As new applications for coherently controlled atoms and molecules are found, interest in this field will grow. This new ability to manipulate matter will likely create new field of

technology in the future.

Control over HHG, and in particular, sculpting a quasi-monocromatic HHG spectrum is directly applicable to time-resolved coherent EUV imaging applications and monitoring chemical reactions on a surface [152]. Furthermore, the increase in conversion efficiency makes this source more practical for applications that require a large photon flux.

Controlled molecular rotational wave packets have, in this thesis, been shown enable a new pulse compression technology that promises to provide sub 5 fs laser pulses in the deep-UV, which are particularly interesting for studying excited-state molecular dynamics.

Furthermore, the molecular control experiments I performed were done nominally at STP conditions, and is a promising avenue for laser-catalyst chemistry with macroscopic yields.

6.1 Towards EUV radiation for table-top coherent imaging

This thesis described work that separately showed both the control over the HHG spectrum by tailoring the driving pulse shape, and the use of HHG radiation for coherent imaging applications. One solution to the shaping of the HHG spectrum demonstrated the selection of a single harmonic order, creating a nearly monochromatic EUV spectrum. A monochromatic spectrum is desirable for coherent imaging applications since a broad spectrum can average out observed fringes, and reducing resolution. Applying the shaped HHG spectrum to coherent imaging will provide greater resolution for HHG microscopy experiments.

Gabor holography has limited applicability for imaging with a relatively low-resolution CCD camera. To improve the resolution, other imaging schemes should be explored. The most straightforward improvement of resolution will be to magnify the hologram with an optical component placed between the object and the CCD camera. We are currently constructing an off-axis reflective Swarzchid object for this purpose. However, each optical element offers a reflectivity of $\sim$ 30 %, so the magnification comes at a high cost in terms of photons. Furthermore, the aberrations of this objective are very sensitive to alignment.

Other approaches depend on the type of object to be imaged. For the case of mostly opaque objects, imaging can be accomplished with phase retrieval algorithms, and the resolution can be higher than the detector with the correct geometry. Hybrid holography, which is a variation of Lensless Fourier Transform microscopy, has led to microscopy with 1 μm resolution using a CCD camera with 24 μm and 545 nm light [159]. This variation of the Leith-Upatnieks off-axis hologram uses a reference wave with a low carrier spatial frequency that is introduced with an opaque mask with a small hole that serves as a reference beam and a larger window in which the object is placed. The object image is retrieved from the inverse Fourier transform of the portion of the spatial frequency distribution at the carrier frequency. These two approaches are just two of the many techniques used for coherent imaging in the visible domain that will be explored for application to the EUV.

6.2 The future of laser-controlled chemical reactions

This thesis has demonstrated that control over molecular degrees of freedom at STP is possible using pulses that are not resonant with any particular electronic transition. In the past, work has focused on control in crossed-beam experiments or in systems with excitation levels well below a percent. We have observed behavior that indicates we have modified the reactivity of two products with a shaped light pulse. However, since a light pulse can also initiate a simple photochemistry reaction, great care must be taken to show that the reaction is not simply due to the breaking of the weakest bond, thus providing new products that may react. The goal is to demonstrate a concerted reaction in which a specific pulse shape enhances the reaction between two molecular reactants.

The apparatus used in the experiments described in this thesis was a hollow-fiber that was filled with the reactants. The benefit of macroscopic conversion makes this setup difficult to use for learning control experiments to manipulate chemical reactions since each laser shot substantially changes the concentrations of each chemical in the cell. Therefore, tracking the changes in the product concentrations becomes difficult. A better approach is to make a cell flow so that the initial conditions are reset for each trial pulse shape that only measures the effect of the reactivity of the trial pulse shape. Once an optimal "catalyst" laser pulse is discovered, the system can be operated in a "production mode" where laser pulses can be focused into large volumes of reactants in order to drive the desired chemical reaction and synthesize a target product.

APPENDICES

APPENDIX A

Evolutionary Algorithm

A.1 Evolutionary Algorithm

This appendix details the Evolutionary Algorithm (EA) used in this thesis work. A broad description of Evolutionary Algorithms in general as well as this algorithm was given in Chapter 2. EAs are a generic problem solving tool, and are not optimal for all problems [62, 63, 103]. In fact, many simple problems are easily solved either analytically or with methods such as steepest descent. EAs are better suited for problems with a complex, diverse parameter space. Nevertheless, the algorithm should be tweaked and tailored to each problem being tackled. The use of adaptive operators and operator constants has made algorithms a bit more general. However, it is difficult to say which algorithm is optimal a given problem.

The specific algorithm used here was arrived at more by convenience rather than by design, and is based on the code written by Erik Zeek. It is quite general, using only one operator to perturb the solutions as the parameter space is explored, and it adapts the amount of perturbation as the optimization progresses. This allowed us to use the same algorithm easily in both atomic and molecular systems with

very different algorithm requirements. The bottom line is the algorithm works well and rapidly finds an optimal solution. Primarily for that reason, the simple version of an EA used in this work was never "upgraded" with other operators. I have observed that the algorithm can act as a "local hill climber" towards the end of an optimization. In my work, I did not employ cross-over, but I suspect that the cross-over operator will help to add diversity to the population and might explore parameter space a bit more than the current algorithm. Other more complicated problems may require the modification of this algorithm, but for the purposes of this thesis, the algorithm worked well, and as they say, "If it ain't broke, don't fix it."

Below I have the details of the EA. I start with pseudocode, then describe the pseudocode, then briefly discuss the Gaussian noise function.

A.2 Pseudocode

Definitions:

j is a test solution, integer ($j = \{0, 1, \cdots, M\}$)

M=number of individuals in a population

k is a control knob number, integer ($k = \{1, 2, \cdots, N\}$)

N=the number of control knobs

V_k =solution variable (pad voltage on pulse shaper $\rightarrow$ spectral phase control)

$\mathbf{V} = \{V_1, V_2, \cdots, V_N\}$

p_j = individual solution = $\{V_{j,1}, V_{j,2}, \cdots, V_{j,N}\}$

F_j is a function that evaluates solutions (spanning$\mathbf{V}$) and is maximized by an "optimal" solution

μ = parents

λ = offspring

$M = \mu + \lambda$

$\mathbf{P}$ = population = $\{p_1, p_2, \cdots, p_M\}$

R = uniform random number generator

G = Gaussian white noise generator

r = standard deviation ratio

Initialize:

Set an initial standard deviation σ_{init} (we typically use $\sim$500 and the max$(V) = 2^{16} - 1$) and choose the number of members of parents (μ) and offspring (λ). We typically use $\mu = 20$, $\lambda = 100$. Note a standard deviation is attached to each member of the population set. Chose a standard deviation ratio $r = 20$.

Start with a set of random voltages for pulse shaping: $p_j = \{R * \max(V), \cdots\}$,for $j = 1 \ldots M$

Loop:

Test the population of solutions and generate harmonic spectra from each solution H_j

Evaluate each harmonic spectrum H_j with the fitness function F_j Here there are a couple of options. The most successful have been:

(a) pick a harmonic and maximize its brightness

(b) maximize the energy of a given harmonic

(c) maximize the brightness difference between a harmonic and the average of

neighboring peaks

Sort the solutions p_j according to the fitness value F_j. Keep the μ top solutions (largest fitness values) and discard the others—these are the new parents.

Make λ/μ copies of the new parents (I set λ/μ = integer).

You now have a population $\mathbf{P}$ with $M = \mu + \lambda$ members

Take each member of the offspring population λ and generate a new standard deviation then use that to perturb (mutate) the solutions:

$for\ j = 1 : \lambda$

$\sigma_{new} = \sigma + G(\frac{\sigma}{r})$

Then for that population member, calculate

$for\ k = 1 : N$

$V_k = V_k + G(\sigma_{new})$

end

end

The mutated solution now forms a new population set (the unmutated parents and the mutated children); the loop is repeated until the increase in the fitness value saturates.

A.3 Description of the pseudocode

In my program, I track a set of information about a given solution: $\{p_j, \sigma_j, F_j, H_j\}$. For the initial step, the σ_{init} is unused, however, it is used in the loop to adaptively modify the standard deviation. The idea is that as the solution approaches an optimal one, we want to perturb the solutions less so that the changes in pulse shape

are smaller and to allow the algorithm to converge better for narrow fitness peaks.

In the initialization stage, parents and children (as defined in Chapter 2) are irrelevant. They simply define the number of solutions (pad voltages for the mirror) that will be generated by the uniform white noise generator (to allow complete random coverage of the parameter space). That is, we take a population with M solutions and generate pad voltages with a random number scaled from 0 to 1, then multiply by the maximum voltage to distribute the random solutions all over the pad voltage parameter space. This set of (M) randomly distributed voltages controls the spectral phase of the input pulse. However, this is uniform random noise, not a Gaussian probability density function.

The next step involves the evaluation of the fitness function. This is highly system dependent, as well as dependent on the final goal. For the HHG control experiments, this involved measuring the HHG spectrum. The spectrum was then divided into sub-arrays (s_j) that each contains one harmonic. Then operations can be performed on the harmonic arrays individually to affect each harmonic separately and the results of those operations can be combined to produces relative changes in the harmonic spectrum. In the case of the molecules, a similar approach was taken, but in that case the spectrum of interest was the probe spectrum and the sub-arrays corresponded to locations of vibrational scatter.

The next step is the all-important solution perturbation (or mutation). The children for the next generation are formed from mutated copies of the new parents (as selected above). For example, if we have 5 times the number of children as parents,

we will now make 5 copies of each of the parents selected as described above. This set of children will then be evaluated as follows:

(a) we will loop through λ children (note the error on the previous psuedocode document)

(b) for each child, the standard deviation of the parent from which it was copied is contained in it's set of information $\{p_j, \sigma_j, F_j, H_j\}$ and a new standard deviation is computed from:

$\sigma_{new} = \sigma + G(\frac{\sigma}{r})$

so the set for that member of the population of children is now:

$\{p_j, \sigma_{new}, F_j, H_j\}$

the new standard deviation is used to mutate the pad voltages of this particular child:

$for\ k = 1 : N$

$V_k = V_k + G(\sigma_{new})$

end

The mutated voltages give a new trial solutions $p_{new} \longrightarrow \{p_{new}, \sigma_{new}, X, X\}$, where X to indicates the harmonic spectrum and fitness value no longer applies to the new trial solution. This information will be gathered in the step after the mutations of all of the children are completed.

(c) step b is repeated for all of the children created for the next generation

(d) The next generation population has then been completed and consists of the parents (the top μ members of the previous generation, unmutated) and children for

the next generation (mutated [with a new standard deviation] copies of the top μ members of the previous generation)

(e) Use the new population set (the new generation) the pad voltages on the deformable mirror one-by-one and then measure the generated harmonic spectrum by downloading the information from the ccd camera. Then the fitness values are computed and the process is repeated.

The role of standard deviation ratio, r, is to help convergence later in the running of the algorithm. Assuming you have evaluated the spectra to get a fitness value, the solutions are then sorted by the fitness value from largest to smallest (larger fitness values mean better solutions). This is when the concepts of children and parents come into play. For the current generation, we just have a population set. This population set is evaluated by the fitness value to choose parents and then consequently create children for the next generation. The number of parents is μ, so the solutions (pad voltages) with the μ highest fitness values are selected from the current generation. These are now referred to as the parents for the next generation ("new parents"). The remainder of the current generation solutions are discarded.

Note: The new population for the next generation is constructed from the solutions whose harmonic spectra evaluated with the fitness function have the μ largest fitness values in the current generation. λ identical copies are made and modified versions of those constitute the children for the next generation. When I referred to the ”new parents”, I mean the parents for the next generation, which are the top μ fitness values from the current generation.

A.4 Mutation operator

The mutation operator uses a Gaussian noise generator. This perturbs the solutions, but limits the size of most perturbations to a value of roughly σ. It utilizes the probability density function:

where σ is the root of the second moment (standard deviation).

and $E\{\}$ is the expected value defined as

$E(x) = \int x f(x) \mathrm{d}x$

The first moment (expected mean value) $\mu = E\{x\} = 0$

and $\sigma = \sqrt{E\left\{(x-\mu)^2\right\}}$

Note that I utilize two different random number generators. In the initialization step, I use the uniform white noise generator. This provides numbers scaled from 0 to 1.0 uniformly. That is, if we ran the generator for a long time, the histogram would have an equal distribution of "hits" for number in the range of 0 to 1. Once the main loop is entered, I switch to a colored noise. That is the histogram will not have equally probability for generating all numbers. The histogram will have a Gaussian profile with a certain standard deviation σ.

BIBLIOGRAPHY

BIBLIOGRAPHY

[1] W.S. Warren, H. Rabitz, and M. Dahleh. Coherent control of quantum dynamics: the dream is alive. *Science*, 259:1581, 1993.

[2] H. Rabitz, R. de Vivie-Riedle, M. Motzkus, and K. Kompa. Whither the future of controlling quantum phenomena? *Science*, 288:824, 2000.

[3] R. Judson and H. Rabitz. Teaching lasers to control molecules. *Phys. Rev. Lett.*, 68:1500–1504, 1992.

[4] A. Weiner, D. Leaird, G. Wiederrecht, and K. Nelson. Femtosecond pulse sequences used for optical manipulation of molecular motion. *Science*, 247:1317, 1990.

[5] D. Meshulach and Y. Silberberg. Coherent quantum control of two-photon transitions by a femtosecond laser pulse. *Nature*, 396:239–42, 1998.

[6] T. Weinacht, J. Ahn, and P. Bucksbaum. Controlling the shape of a quantum wave function. *Nature*, 397:233, 1999.

[7] T. Hornung, R. Meier, D. Zeidler, K. Kompa, D. Proch, and M. Motzkus. Optimal control of one and two photon transitions with shaped femtosecond pulses and feedback. *Appl. Phys. B*, 71:277, 2000.

[8] R. Uberna, Z. Amitay, R. Loomis, and S. Leone. Phase-tailoring molecular wave packets to time shift their dynamics. *Chem. Phys.*, 267:141, 2001.

[9] A. Assion, T. Baumert, M. Bergt, T. Brixner, B. Kiefer, V. Seyfried, M. Strehle, and G. Gerber. Control of chemical reactions by feedback optimized phase shaped femtosecond laser pulses. *Science*, 282:919, 1998.

[10] R. J. Levis, M. Menkir, and H. Rabitz. Selective covalent bond dissociation and rearrangement by closed-loop, optimal control of tailored, strong field laser pulses. *Science*, 292:709, 2001.

[11] R. Bartels, S. Backus, E. Zeek, L. Misoguti, I. Christov, M. Murnane, and H. Kapteyn. Shaped-pulse optimization of coherent emission of high-harmonic soft x-rays. *Nature*, 406:164, 2000.

[12] R. Bartels, S. Backus, I. Christov, H. Kapteyn, and M. Murnane. Attosecond time-scale feedback control of coherent x-ray generation. *Chemical Physics*, 267:277–289, 2001.

[13] I. P. Christov, R. Bartels, H. C. Kapteyn, and M. M. Murnane. Attosecond time-scale intra-atomic phase matching of high harmonic generation. *Phys. Rev. Lett.*, 86:5458–5461, 2001.

[14] M. Lewenstein, P. Balcou, M. Y. Ivanov, and P. B. Corkum. *Phys. Rev. A*, 49:2117, 1993.

[15] P. Salieres, P. Antoine, A. de Bohan, and M. Lewenstein. *Phys. Rev. Lett.*, 81:5544, 1998.

[16] I. P. Christov, M. M. Murnane, and H. C. Kapteyn. *Phys. Rev. Lett.*, 78:1251, 1997.

[17] I. P. Christov, M. M. Murnane, and H. C. Kapteyn. *Phys. Rev. A*, 57:R2285, 1998.

[18] M. Lewenstein, P. Balcou, M. Y. Ivanov, A. Lhuillier, and P. B. Corkum. Theory of high-harmonic generation by low-frequency laser fields. *Physical Review A*, 49:2117–2132, 1994.

[19] R. Zare. *Science*, 279:1875, 1998.

[20] T.C. Weinacht, R.A. Bartels, S. Backus, P.H. Bucksbaum, B. Pearson, J.M. Geremia, H. Rabitz, H.C. Kapteyn, and M.M. Murnane. Coherent learning control of vibrational motion in room temperature molecular gases. *Chem. Phys. Lett.*, 344:333–338, 2001.

[21] R. Bartels, T. Weinacht, S. Leone, H. Kapteyn, and M. Murnane. Nonresonant control of multimode vibrational wave packets at room temperature. *Phys. Rev. Lett.*, 88, 2002.

[22] R. A. Bartels, T. C. Weinacht, N. Wagner, M. Baertschy, C. H. Greene, M. M. Murnane, and H. C. Kapteyn. Phase modulation of ultrashort light pulses using molecular rotational wave packets. *Phys. Rev. Lett.*, 88:013903, 2002.

[23] R. A. Bartels and et. al. *Science*, submitted, 2002.

[24] R. A. Bartels, A. Paul, M. M. Murnane, H. C. Kapteyn, and S. Backus. Absolute determination of the wavelength and spectrum of an euv beam using a young's double slit measurement. *Optics Letters*, submitted, 2001.

[25] M. Quack. *Femtosecond Chemistry*. New York: McGraw-Hill, 1990.

[26] P. Planken, I. Brener, M. Nuss, M. Luo, and S. Chuang. Coherent control of terahertz charge oscillations in a coupled quantum well using phase-locked optical pulses. *Phys. Rev. B*, 47:4903–4906, 1993.

[27] E. Dupont, P. B. Corkum, H. Liu, M. Buchanan, and Z. Wasilewski. Phase controlled currents in semiconductors. *Phys. Rev. Lett*, 74:3596, 1995.

[28] A. Hache, Y. Kostoulas, R. Atanasov, J. Hughes, J. Sipe, and H. van Driel. Observation of coherently controlled photocurrent in unbiased, bulk gaas. *Phys. Rev. Lett.*, 78:306, 1997.

[29] H. Petek, A. Heberle, W. Nessler, H. Nagano, S. Kubota, S. Matsunami, N. Moriya, and S. Ogawa. Optical phase control of coherent electron dynamics in metals. *Phys. Rev. Lett.*, 79:4649, 1997.

[30] N. H. Bonadeo, J. Erland, D. Gammon, D. Park, D. S. Katzer, and D. G. Steel. Coherent optical control of the quantum state of a single quantum dot. *Science*, 282:1473, 1998.

[31] D. Yee, K. Yee, S. Hohng, and D. Kim. Coherent control of absorption and polarization decay in a gaas quantum well: time and spectral domain studies. *Phys. Rev. Lett.*, 84:3474, 2000.

[32] P. Planken, I. Brener, M. Nuss, M. Luo, S. Chuang, and L. Pfeiffer. Thz radiation from coherent population changes in quantum wells. *Phys. Rev. B*, 49:4668–4672, 1994.

[33] D. S. Citrin, M. Yamanishi, and Y. Kadoya. Coherent control of terahertz generation in a dc-biased semiconductor microcavity. *J. Selec. Top. Quant. Elec.*, 2:720–723, 1996.

[34] D. Cote, J. Fraser, M. DeCamp, P. Bucksbaum, and H. van Driel. Thz emission from coherently controlled photocurrents in gaas. *Appl. Phys. Lett.*, 75:3959, 1999.

[35] P. Brumer and M. Shapiro. Control of unimolecular reactions using coherent light. *Chem. Phys Lett.*, 126:541, 1986.

[36] C. Chen, Y. Yin, and D. S. Elliot. Interference between optical transitions. *Phys. Rev. Lett.*, 64:507, 1990.

[37] S. Lu, S. M. Park, Y. Xie, and R. J. Gordon. Coherent laser control of bound-to-bound transitions of hcl and co. *J. Chem. Phys.*, 96:6613, 1992.

[38] L. Zhu, V. Kleinman, X. Li, S. Lu, K. Trentelman, and R. J. Gordon. Coherent laser control of the product distribution obtained in the photoexcitation of hi. *Science*, 270:77, 1995.

[39] V. Kleinman, L. Zhu, X. Li, and R. J. Gordon. Coherent phase control of the photoionization of h2s. *J. Chem. Phys.*, 102:5863, 1995.

[40] V. Kleinman, L. Zhu, J. Allen, and R. J. Gordon. Coherent control over the photodissociation of ch3i. *J. Chem. Phys.*, 103:10800, 1995.

[41] A. Shnitman, I. Sofer, I. Golub, A. Yogev, M. Shapiro, Z. Chen, and P. Brumer. Experimental observation of laser control: Electronic branching in the photodissociation of na2. *Phys. Rev. Lett.*, 76:2886, 1996.

[42] D. J. Tannor and S.A. Rice. Control of selectivity of chemical reactions via control of wave packet evolution. *J. Chem. Phys.*, 83:5013, 1985.

[43] D. J. Tannor, T. Kosloff, and S. A. Rice. Coherent pulse sequence induced control of selectivity of reactions: Exact quantum mechanical calculations. *J. Chem. Phys.*, 85:5805, 1986.

[44] S. Shi, A. Woody, and H. Rabitz. Optimal control of selective vibrational excitation in harmonic linear chain molecules. *J. Chem. Phys.*, 88:6870, 1988.

[45] J. Fourkas, W. Jr. Wilson, G. Wackerle, A. Frost, and M. Fayer. Picosecond time-scale phase-related optical pulses: measurement of sodium optical coherence by observation of incoherent fluorescence. *JOSB*, 6:1905, 1989.

[46] N. Scherer, A. Ruggiero, M. Du, and G. Fleming. Time resolved dynamics of isolated molecular systems studied with phase-locked femtosecond pulse pairs. *J. Chem. Phys.*, 93:856, 1990.

[47] T. Baumert, M. Grosser, R. Thalweiser, and title= journal=Phys. Rev. Lett volume=67 pages=3753 year=1991 Gerber, G.

[48] E. Potter, J. Herek, S. Pedersen, Q. Liu, and A. Zewail. Femtosecond laser control of a chemical reaction. *Nature*, 355:22, 1992.

[49] E.D. Potter, J.L. Herek, S. Pedersen, Q. Liu, and A.H. Zewail. *Nature*, 355:66, 1992.

[50] V. Blanchet, C. Nicole, M. Bouchene, Girard, and B. Temporal coherent control in two-photon transitions: from optical interferences to quantum interferences. *Phys. Rev. Lett.*, 78:2716, 1997.

[51] E. Charron, A. Giusti-Suzor, and F. Mies. *Phys. Rev. Lett.*, 75:2815, 1998.

[52] R. Leeuwen, M. Bajema, and R. Jones. Coherent control of the energy and angular distribution of autoionized electrons. *Phys. Rev. Lett.*, 82:2852, 1999.

[53] A. Glass, T. Rozgonyi, T. Feruer, R. Sauerbery, and G. Szabo. Control of the photodissociation of cscl. *Appl. Phys. B*, 71:267, 2000.

[54] B. Kohler, V. Yakovlev, J. Che, J. Krause, M. Messina, K. Wilson, N. Schwenter, R. Whitnell, and Y. Yang. Quantum control of wave packet evolution with tailored femtosecond pulses. *Phys. Rev. Lett.*, 74:3360, 1995.

[55] C. Bardeen, Q. Wang, and C. Shank. Selective excitation of vibrational wave packet motion using chirped pulses. *Phys. Rev. Lett.*, 75:3410, 1995.

[56] I. Pastrik, E. Brown, Q. Zhang, and M. Dantus. Quantum control of the yield of a chemical reaction. *J. Chem. Phys.*, 108:4375, 1998.

[57] D. Meshulach and Y. Silberberg. Coherent quantum control of multiphoton transitions by shaped ultrashort optical pulses. *Phys. Rev. A*, 60:1287, 1999.

[58] Nirit Dudovich, Barak Dayan, Sarah M. Gallagher Faeder, and Yaron Silberberg. Transform-limited pulses are not optimal for resonant multiphoton transitions. *Phys. Rev. Lett.*, 86:47, 2001.

[59] H. Rabitz. *Advances in Chemical Physics 101*, page 315, 1997.

[60] R. M. Friedberg. A learning machine: Part i. *IBM Journal*, 2:2–13, 1958.

[61] H. J. Bremermann. Optimization through evolution and recombination. In et al. M. C. Yovits, editor, *Self-Organizing Systems*, chapter 72. Washington D.C.: Spartan Books, 1962.

[62] L. J. Fogel. *On the Organization of Intellect.* PhD thesis, UCLA, 1964.

[63] T. Back. *Evolutionary Algorithms in Theory and Practice.* New York, NY.: Oxford University Press, Inc., 1996.

[64] H. P. Schwefel. Collective phenomenon in evolutionary systems. In *Prerpints of the* 31^{st} *Annual Meeting of the International Society for General Systems Research*, chapter 2, page 1025. Budapest, 1987.

[65] L. J. Eshelman, R. A. Carvna, and J. D. Schaffer. Biases in crossover landscape. In J.D. Schaffer, editor, *Proceedings of the* 3^{rd} *International Conference on Genetic Algorithms and Their Applications.* San Mateo, CA: Morgan Kaufmann Publishers, 1989, 1989.

[66] J. D. Schaffer and A. Morishima. An adaptive crossover distribution mechanism for genetic algorithms. In J. J. Grefenslette, editor, *Proceedings of the* 2^{nd} *International Conference on Genetic Algorithms and Their Applications.* San Hillside, NJ: Lawrenece Erlbaum Associates, 1987.

[67] C. Bardeen, V. Yakovlev, K. Wilson, S. Carpenter, P. Weber, and W. Warren. Feedback quantum control of molecular electronic population transfer. *Chem. Phys. Lett.*, 280:151–8, 1997.

[68] T. Weinacht, J. White, and P. Bucksbaum. Towards strong field mode-selective chemistry. *J. Chem. Phys.*, 103:10166, 1999.

[69] E. Zeek, R. Bartels, M. M. Murnane, H. C. Kapteyn, S. Backus, and G. Vdovin. *Opt. Lett.*, 25:587, 2000.

[70] M. T. Asaki, C. P. Huang, D. Garvey, J. Zhou, H. C. Kapteyn, and M. M. Murnane. Generation of 11-fs pulses form a self-mode-locked ti:sapphire laser. *Opt. Lett.*, 18:977–9, 1993.

[71] E. Zeek, K. Maginnis, S. Backus, U. Russek, M. Murnane, G. Mourou, H. Kapteyn, and G. Vdovin. *Opt. Lett.*, 24:493, 1999.

[72] K. W. DeLong, R. Trebino, J. Hunter, and W. E. White. *JOSA B*, 11:2206, 1994.

[73] S. Backus, C. Durfee, M. M. Murnane, and H. C. Kapteyn. *Rev. Sci. Instrum.*, 69:1207, 1998.

[74] A. McPherson, G. Gibson, H. Jara, U. Johann, T. S. Luk, I. A. McIntyre, K. Boyer, and C. K. Rhodes. *JOSA B*, 4:595, 1987.

[75] A. L'Huillier, K. J. Schafer, and K. C. Kulander. High-order harmonic generation in xenon at 1064 nm: The role of phase matching. *Phys. Rev. Lett.*, 66:2200, 1991.

[76] J. J. Macklin, J. D. Kmetec, and C. L. III Gordon. *Phys. Rev. Lett.*, 70:766, 1993.

[77] J. M. Schins, P. Breger, and et al. Observation of lawser-assisted auger decay in argon. *Phys. Rev. Lett.*, 73:2180, 1994.

[78] T. E. Glover, R. W. Schoenlein, and et al. Observation of laser assisted photoeclectric effect and femtosecond high order harmonic radiation. *Phys. Rev. Lett.*, 76:2486–2471, 1996.

[79] Paul Corkum. Plasma perspective on strong field miltiphoton ionization. *Phys. Rev. Lett.*, 71:1994–1997, 1993.

[80] K. C. Kulander, K. J. Schafer, and J. L. Krause. Dynamics of short-pulse excitation, ionization and harmonic conversion. In B. Piraux, A. L'Huillier, and K. Rzazewski, editors, *NATO Advanced Science Institutes Series*, chapter 316, pages 95–110. San Hillside, NJ: Lawrenece Erlbaum Associates, 1987.

[81] Z. Chang, A. Rundquist, H. Wang, I. Christov, H. C. Kapteyn, and M. M. Murnane. *Phys. Rev. A*, 58:R30, 1998.

[82] P. Balcou, A. S. Dederichs, and et al. Quantum-path analysis and phase matching of high-order frequency mixing processes in strong laser fields. *Journal of Physics B-Atomic Molecular and Optical Physics*, 32:2973–2989, 1999.

[83] R. Haight. *Surface science reports*, 21:275, 1995.

[84] P. B. Corkum, N. H. Burnett, and M. Y. Ivanov. *Opt. Lett.*, 19:1870, 1994.

[85] M. V. Ammosov, N. B. Delone, and V. P. Krainov. *Soviet Physics JETP*, 64:1191, 1986.

[86] A. M. Weiner, J. P. Heritage, and E. M. Kirschner. *Journal of the Optical Society of America B-Optical Physics*, 5:1563, 1988.

[87] J. Zhou, J. Peatross, M. M. Murnane, H. C. Kapteyn, and I. P. Christov. *Phys. Rev. Lett.*, 76:752, 1996.

[88] Z. H. Chang, A. Rundquist, H. W. Wang, M. M. Murnane, and H. C. Kapteyn. Generation of coherent soft x rays at 2.7 nm using high harmonics. *Phys. Rev. Lett.*, 79:2967, 1997.

[89] C. Spielmann, N. H. Burnett, S. Sartania, R. Koppitsch, M. Schnürer, C. Kan, M. Lenzner, P. Wobrauschek, and F. Krausz. Generation of coherent x-rays in the water window using 5-femtosecond laser pulses. *Science*, 278:661, 1997.

[90] A. Rundquist, C. G. Durfee III, S. Backus, C. Herne, Z. Chang, M. M. Murnane, and H. C. Kapteyn. Phase-matched generation of coherent soft x-rays. *Science*, 280:1412–1415, 1998.

[91] C. G. Durfee, A. Rundquist, Z. Chang, C. Herne, F. Weihe, S. Backus, M. M. Murnane, and H. C. Kapteyn. Phase-matching of high-order harmonic generation in capillary waveguides. *IQEC*, 1998.

[92] D. Yelin, D. Melshulach, and Y. Silberberg. Adaptive femtosecond pulse compression. *Opt. Lett.*, 22:1793, 1997.

[93] T. Brixner, M. Strenle, and G. Gerber. Feedback-controlled optimization of amplified femtosecond laser pulses. *Appl. Phys. B*, 68:281, 1999.

[94] G. Tempea and et al. *Journal of Physics B-Atomic Molecular and Optical Physics*, 16:669, 1999.

[95] I. P. Christov and et al. *Phys. Rev. Lett.*, 77:1743, 1996.

[96] K. J. Schafer and et al. *Phys. Rev. Lett.*, 78:638, 1997.

[97] M. Lewenstein, P. Salieres, and A. Lhuillier. Phase of the atomic polarization in high-order harmonic- generation. *Physical Review A*, 52:4747–4754, 1995.

[98] Xi Chu and Shih-I Chu. Optimization of high-order harmonic generation by genetic algorithm and wavelet time-frequency analysis of quantum dipole emission. *Physical Review A*, 64:021403, 2001.

[99] Paul Corkum. *Private Communication*, July, 2001.

[100] G. Knopp and et al. *J. Raman Spec.*, 31:51, 2000.

[101] F. Crim. *Acc. Chem. Res.*, 32:877, 1999.

[102] JM Geremia, W. J. Zhu, and H. Rabitz. *J. of Chem. Phys.*, 113:10841, 2000.

[103] H. P. Schwefel. *Evolution and Optimum Seeking.* John Wiley & Sons, Inc., 1995.

[104] Y. X. Yan, E. B. Gamble Jr., and K. A. Nelson. *J. Chem. Phys.*, 83:5391, 1985.

[105] L. Dhar, J. Rogers, and K. A. Nelson. *Chem. Rev.*, 94:157, 1994.

[106] H. W. Schrotter and H. W. Klockner. In A. Weber, editor, *Raman Scattering*. Springer Verlag, 1970.

[107] R. L. Carmen, F. Shimizu, C. S. Wang, and N. Bloembergen. *Phys. Rev. Lett.*, 2:5, 1979.

[108] Q. Meng, Y. Zheng, and S. Ding. *Int. J. Quant. Chem.*, 81:154, 2001.

[109] K. D. Rector and et al. *J. Chem Phys.*, 106:10027, 1997.

[110] T. Young. *Philos. Trans. R. Soc. XCII*, 12:387, 1802.

[111] J. Zhou, J. Peatross, M. M. Murnane, and et al. *Phys. Rev. Lett.*, 76:752, 1996.

[112] P. Y. Han, G. C. Cho, and X. C. Zhang. *J. Nonlin. Opt. Phys. & Mat.*, 8:89, 1999.

[113] P. T. Wilson, Y. Jiang, O. A. Aktsipertrov, and et al. *Opt. Lett.*, 24:496, 1999.

[114] R. A. Fisher. *Appl. Phys. Lett.*, 14:140, 1969.

[115] R. L. Fork, C. H Brito Cruz, P. C. Becker, and et al. *Opt. Lett.*, 12:483, 1987.

[116] A. Baltuska, Z. Wei, M. Pshenichnikov, and et al. *Opt. Lett.*, 22:102, 1997.

[117] M. Nisoli, S. de Silvestri, O. Svelto, and et al. *Opt. Lett.*, 22:522, 1997.

[118] E. B. Treacy. *IEEE J. Quant. Elec.*, QE-5:454, 1969.

[119] D. Grischkowsky and A. C. Balant. *Appl. Phys. Lett.*, 41:1, 1982.

[120] S. E. Harris and A. V. Sokolov. *Phys. Rev. Lett.*, 81:2894, 1998.

[121] M. Wittmann, A. Nazarkin, and G. Korn. *Phys. Rev. Lett.*, 84:5508, 2000.

[122] V. P. Kalosha and J. Herrmann. *Opt. Lett.*, 26:456, 2001.

[123] V. P. Kalosha and M. Ivanov. *Phys. Rev. Lett.*, submitted, 2001.

[124] J. P. Heritage, T. K. Gustafson, and C. H. Lin. *Phys. Rev. Lett.*, 34:1299, 1975.

[125] J. Ortigoso, M. Rodriguez, M. Gupta, and et al. *J. Chem. Phys.*, 110:3870, 1999.

[126] B. Friedrich and D. Herschbach. *Phys. Rev. Lett.*, 74:4623, 1995.

[127] Q. L. Jie, S. J. Wang, and L. F. Wei. *Phys. Rev. A*, 57:3262, 1998.

[128] A. E. Siegman. *Lasers.* University Science Books, Mill Valley, 1986.

[129] S. Backus, C. G. Durfee, G. A. Mourou, and et al. *Opt. Lett.*, 22:1256, 1997.

[130] E. Hertz, O. Faucher, B. Lavorel, and et al. *Phys. Rev. A*, 61:033816, 2000.

[131] E. Hertz, O. Faucher, B. Lavorel, and et al. *J. Chem. Phys.*, 113:6132, 2000.

[132] M. Kubasik, A. Cebo, E. Hertz, and et al. *J. Phys. B*, 34:2437, 2001.

[133] G. P. Agrawal. *Nonlinear Fiber Optics.* New York: Academic Press, 2001.

[134] D. N. Nikogosyan. *Properties of Optical and Laser-Related Materials: A Handbook.* John Wiley & Sons: New York, 1997.

[135] W. J. Tropf and et. al. Properties of crystals and glasses. In M. Bass and et al., editors, *Handbook of Optics II: Devices, Measurements, and Properties*, chapter 33. McGraw Hill Inc.: New York, 2000.

[136] J. A. R. Samson. *Techniques of vacuum ultraviolet spectroscopy.* Glasgow: Cruithne, 2000.

[137] D. Attwood. New opportunities at soft-x-ray wavelengths. *Physics Today*, 45:24–31, 1992.

[138] D. L. Matthews, P. L. Hagelstein, and et al. Demonstration of a soft x-ray amplifier. *Physical Review Letters*, 54:110–3, 1985.

[139] J. Andruszkow, B. Aune, V. Ayvazyan, and et al. First observation of self-amplified spontaneous emission in a free-electron laser at 109 nm wavelength. *Physical Review Letters*, 85:3825–3829, 2000.

[140] T. Ditmire, E. Gumbrell, R. Smith, J. Tisch, D. Meyerhofer, and M. Hutchinson. Spatial coherence measurement of soft x-ray radiation produced by high order harmonic generation. *Physical Review Letters*, 77:4756–9, 1996.

[141] P. Salieres, A. L'Huillier, and M. Lewenstein. Coherence control of high-order harmonics. *Physical Review Letters*, 74:3776, 1995.

[142] P. Salieres, T. Ditmire, M. Perry, A. L'Huillier, and M. Lewenstein. Angular distributions of high-order harmonics generated by a femtosecond laser. *Journal of Physics B (Atomic, Molecular and Optical Physics)*, 29:4771–4786, 1996.

[143] K. A. Goldberg, P. Naulleau, S. Lee, C. Bresloff, C. Henderson, D. Attwood, and J. Bokor. High-accuracy interferometry of extreme ultraviolet lithographic optical systems. *Journal of Vacuum Science & Technology B*, 16:3435–3439, 1998.

[144] B. Thompson and E. Wolf. *J. Opt. Soc. Am.*, 46:895, 1957.

[145] C. Chang, P. Naulleau, E. Anderson, and D. Attwood. *Opt. Comm.*, 182:25, 2000.

[146] Y. Lui, M. Seminario, F. Tomasel, C. Chang, J. Rocca, and D. Attwood. *Phys. Rev. A*, 63:033802, 2001.

[147] J. Goodmann. *Statistical Optics*. Wiley, New York, 1985.

[148] E. Wolf and A. J. Devaney. On a relationship between spectral properties and spatial coherence properties of light. *Optics Letters*, 6:168–170, 1981.

[149] A. T. Friberg and E. Wolf. Relationships between the complex degrees of coherence in the space-time and in the space-frequency domains. *Optics Letters*, 20:623–625, 1995.

[150] S. Backus, R. Bartels, S. Thompson, R. Dollinger, H. C. Kapteyn, and M. M. Murnane. High-efficiency, single-stage 7-khz high-average-power ultrafast laser system. *Optics Letters*, 26:465–467, 2001.

[151] E. A. J. Marcatili and R. A. Schmeltzer. Hollow metallic and dielectric waveguides for long distance optical transmission and lasers. *Bell System Technical Journal*, 43:1783, 1964.

[152] M. Bauer, C. Lei, K. Read, R. Tobey, J. Gland, M. M. Murnane, and H. C. Kapteyn. Direct observation of surface chemistry using ultrafast soft-x- ray pulses. *Physical Review Letters*, 8702:5501, 2001.

[153] R. Haight and D. R. Peale. Tunable photoemission with harmonics from subpicosecond lasers. *Review of Scientific Instruments*, 65:1853, 1994.

[154] K. Read, H. S. Karlsson, M. M. Murnane, H. C. Kapteyn, and R. Haight. Excitation dynamics of dye doped tris(8-hydroxy quinoline) aluminum films studied using time-resolved photoelectron spectroscopy. *Journal of Applied Physics*, 90:294–300, 2001.

[155] S. Lindaas, M. Howells, C. Jacobsen, and A. Kalinovsky. x-ray holographic microscopy via photoresist recording and atomic force microscope readout. *JOSA A*, 13:1788, 1996.

[156] D. Gabor. A new microscope principle. *Nature*, 161:777–8, 1948.

[157] G. L. Rogers. Gabor diffraction microscope: the hologram as a generalized zone-plate. *Nature*, 166:237, 1950.

[158] A. G. Michette. *Optical Systems for soft x rays*. Plenum, New York, 1986.

[159] T. Yasuhiro and H. Ohzu. Fast numerical reconstruction technique to high-resolution hybrid holographic microscopy. *Applied Optics*, 38:2204–2211, 1999.

ABSTRACT

Coherent Control of Atoms and Molecules

by

Randy Alan Bartels

Co-Chairs: Henry C. Kapteyn & Margaret M. Murnane

Whenever scientific tools are significantly advanced, new discoveries soon follow. My thesis work relies on advances in ultrafast laser technology that allow precise control over the shape of sub 20-fs laser pulses. This laser system enabled many new experiments that yielded significant advances in attosecond science, atomic physics, extreme nonlinear optics, quantum chemistry, coherent control, molecular physics, ultrafast optical phase modulation, EUV coherent imagines, and EUV radiation sources.

By using an automated learning control algorithm coupled to our deformable mirror pulse shaper, we have demonstrated the control of a process on an attosecond time-scale for the first time. We demonstrate the manipulation of the phase of an electron wave packet, allowing us to tailor the EUV spectrum generated by high-order harmonic generation. These optimal fields were discovered by a learning algorithm that both found an unknown optimal solution, but also discovered an unknown phase-matching mechanism that occurs in the interaction of a single atom and light pulse.

We control molecular vibrational and rotational coherences with the same learning algorithm, demonstrating selective control in room temperature molecules at atmospheric pressures. Moreover, we demonstrate that modifications to the algorithm can help automatically uncover the physics of the control mechanism found by the learning algorithm.

We also demonstrate a new pulse-compression technique using rotational phase modulation, where optical pulses were compressed by an order of magnitude after phase modulation by a molecular rotational coherence and subsequent propagation

through a transparent window. This technique will enable efficient pulse compression in the deep-UV.

Finally, we measure the coherence of EUV light generated by high-harmonic upconversion of a femtosecond laser. In phase-matched hollow-fiber geometry, the EUV light exhibits the highest inherent spatial coherence of any source in this region of the spectrum. We use this source to demonstrate the coherent image with first table-top EUV radiation. Since this source exhibits full spatial coherence at very short wavelength, this light source represents has smallest inherent effective source-size of any light source yet created. We also demonstrate that the spectrum of an optical field can be determined by measuring the interference of a double-slit pattern.